

Direct measurement of anisotropic resistivity in thin films using a 4-probe STM

Tim Flatten

Schlüsseltechnologien / Key Technologies

Band / Volume 213

ISBN 978-3-95806-460-7

Forschungszentrum Jülich GmbH
Peter Grünberg Institut (PGI)
Elektronische Eigenschaften (PGI-6)

Direct measurement of anisotropic resistivity in thin films using a 4-probe STM

Tim Flatten

Schriften des Forschungszentrums Jülich
Reihe Schlüsseltechnologien / Key Technologies

Band / Volume 213

ISSN 1866-1807

ISBN 978-3-95806-460-7

Bibliografische Information der Deutschen Nationalbibliothek.
Die Deutsche Nationalbibliothek verzeichnet diese Publikation in der
Deutschen Nationalbibliografie; detaillierte Bibliografische Daten
sind im Internet über <http://dnb.d-nb.de> abrufbar.

Herausgeber
und Vertrieb: Forschungszentrum Jülich GmbH
 Zentralbibliothek, Verlag
 52425 Jülich
 Tel.: +49 2461 61-5368
 Fax: +49 2461 61-6103
 zb-publikation@fz-juelich.de
 www.fz-juelich.de/zb

Umschlaggestaltung: Grafische Medien, Forschungszentrum Jülich GmbH

Druck: Grafische Medien, Forschungszentrum Jülich GmbH

Copyright: Forschungszentrum Jülich 2020

Schriften des Forschungszentrums Jülich
Reihe Schlüsseltechnologien / Key Technologies, Band / Volume 213

D 38 (Diss. Köln, Univ., 2019)

ISSN 1866-1807
ISBN 978-3-95806-460-7

Vollständig frei verfügbar über das Publikationsportal des Forschungszentrums Jülich (JuSER)
unter www.fz-juelich.de/zb/openaccess.



This is an Open Access publication distributed under the terms of the [Creative Commons Attribution License 4.0](https://creativecommons.org/licenses/by/4.0/),
which permits unrestricted use, distribution, and reproduction in any medium, provided the original work is properly cited.

Kurzzusammenfassung

Die bekanntlich beste Wahl um den Widerstand einer Probe zu messen und damit die Widerstandseigenschaften zu bestimmen, sind 4-Punkt elektronische Transportmessungen, weil die Kontaktwiderstände vernachlässigbar klein sind. Von den vielen bereits entdeckten Varianten der 4-Punkt-Methode, ist das 4-Spitzen Rastertunnelmikroskop das effektivste experimentelle Hilfsmittel zur Messung des Probenwiderstands auf kleinen Längenskalen, einschließlich der Möglichkeit den Spitzenabstand zu variieren.

Im Fokus der Grundlagenforschung stehen geschichtete Materialien aufgrund ihrer faszinierenden Eigenschaften und ihres hohen Potenzials in einer Vielzahl von Anwendungen. Darüber hinaus sind sie auch mögliche Eltern-Materialien für sogenannte 2D-Materialien aufgrund einer typischen, schwächeren chemischen Bindung entlang einer kristallinen Achse. Neben den bekannten Eltern-Materialien wie Graphit, hexagonales Bornitrid und Übergangs-Metall-Dichalkogenide gibt es eine weitere Klasse von geschichteten Materialien, die sogenannten MAX Phasen, welche sowohl metallische als auch keramische Eigenschaften umfassen. Diese einzigartige Kombination ergibt sich aus einem komplexen, anisotropen Bindungsschema, das zu einer anisotropen Leitfähigkeit führt. Werden diese geschichteten Materialien als dünne Filmproben hergestellt, umfassen sie in der Regel eine Bindungsanisotropie senkrecht zur Oberfläche. Somit wird eine Anisotropie zwischen den Leitfähigkeiten in der Ebene und senkrecht zur Probenoberfläche erwartet. Führt man die Widerstandsfähigkeit als Tensor zweiter Ordnung ein, können solche anisotropen elektronischen Transporteigenschaften bestimmt werden. Die Widerstandsfähigkeit wird dann durch eine symmetrisch abhängige Anzahl unabhängiger Komponenten ausgedrückt, die aus Widerstandsmessungen in verschiedenen Richtungen der Probe bestimmt werden können. Die Komponenten, welche in der Ebene liegen, können mit mehreren bekannten Methoden einfach charakterisiert werden. Solange ein Material nur als dünner Film hergestellt werden kann, ist es bislang nicht möglich die Widerstandsfähigkeitskomponente senkrecht zur Ebene ohne zusätzliche Behandlungen oder Modifikationen der Probe zu bestimmen.

Daher wird in dieser Arbeit eine neuartige direkte und parameterfreie Methode entwickelt, welche die senkrecht aus der Probe gerichtete Widerstandsfähigkeit ohne weitere Behandlung der Probe bestimmt. Mit einem Multi-Spitzen-Rastertunnelmikroskop werden 4-Punkt-Transportmessungen mit variablem Spitzenabstand durchgeführt. Die Beobachtung des Übergangs vom 3D-Transportbereich für kleine Abstände zwischen den Spitzen zum 2D-Bereich für große Abstände ermöglicht die Bestimmung der Widerstandsfähigkeiten, sowohl in der Ebene als auch senkrecht zur Ebene. Nach der analytischen Beschreibung der Methode werden die experimentellen Verfahren zur Messung der elektronischen Transporteigenschaften mit einem Multi-Spitzen-Rastertunnelmikros-

kop beschrieben, insbesondere die Einflüsse von Probengröße und -form, Oberflächenmorphologie und Korn-Größe, die Größe des Spitzen-Proben-Kontakts sowie die wichtigsten experimentellen Fehlerquellen.

Mit dieser Methode wird eine erste direkte und parameterfreie Messung der anisotropen elektrischen Widerstandsfähigkeit einer magnetischen $(\text{Cr}_{0.5}\text{Mn}_{0.5})_2\text{GaC}$ MAX Phasen Probe vorgestellt. Mit Messungen auf nur einer dünnen Filmprobe ermöglicht die Beobachtung des Übergangs zwischen dem 3D- und dem 2D-Transportfall die gleichzeitige Bestimmung von in der Ebene und senkrecht zur Ebene gerichteten Widerstandsfähigkeiten und ergibt eine große Anisotropie. Die Widerstandsfähigkeit senkrecht zur Ebene ist um den Faktor 500 größer als die in der Ebene, was auf das komplexe Bindungsschema der MAX Phasen zurückzuführen ist. Das hier bestimmte Verhältnis der Widerstandsfähigkeiten gibt einen besseren und quantitativeren Einblick in das Zusammenspiel von kristalliner Struktur, Bindungsstruktur und elektronischen Transporteigenschaften.

Zusätzlich werden $(\text{Cr}_{2/3}\text{Ho}_{1/3})_2\text{AlC}$ Kristallite, die zu den i-MAX Phasen mit chemischer Ordnung in der Ebene gehören, untersucht. Die Ergebnisse liefern signifikante Hinweise auf eine anisotrope Widerstandsfähigkeit sowohl in als auch senkrecht zu der Ebene. Die Anisotropie in der Ebene ist eine Folge der chemischen Ordnung der Übergangsatome und der seltenen Erd-Atome. Die im Vergleich zu herkömmlichen MAX Phasen schwächere Anisotropie zwischen der senkrecht zur Ebene und in der Ebene liegende Widerstandsfähigkeit wird durch die Vorhersagen über geringere anisotrope Bandstrukturen für i-MAX Phasen bestätigt. Diese Messungen stellen die erste Charakterisierung der anisotropen Widerstandsfähigkeit in einer i-MAX Phase dar. Darüber hinaus sind sie ein *Proof-of-Principle* für die Bestimmung des gesamten Widerstandsfähigkeiten-Tensors eines Materials mit orthorhombischer oder höherer Symmetrie durch die Hilfe der 4-Punkt elektronischen Transportmessungen an einzelnen dünnen oder kristallinen Proben.

Abstract

Four-point electronic transport measurements have proven to be the best choice for determining the resistance of a sample and thus the resistivity properties, because the contact resistances are negligibly small. Various techniques using the 4-point method have been explored, whereby the 4-probe scanning tunneling microscope is a powerful experimental tool to measure the sample resistance on small length scales including the possibility to vary probe spacings.

Nowadays, layered materials are in the focus of interest due to their intriguing fundamental properties and their high potential in a variety of applications. In addition, they are also possible parenting materials for so-called 2D materials due to a typically weaker chemical bonding along one crystalline axis. Beside the famous parent-materials such as graphite, hexagonal boron nitride, and transition metal dichalcogenides, there is a further class of layered materials, namely the so-called MAX phases comprising both metal as well as ceramic properties. This unique combination stems from a complex, anisotropic bonding scheme that leads to an anisotropic conductivity. Growing those layered materials as thin-film samples, they comprise usually a bonding anisotropy perpendicular to the surface. Thus, an anisotropy between the in-plane and out-of-plane conductivities is expected. Such anisotropic electronic transport properties are characterized by introducing the resistivity as a second rank tensor. The resistivity is then expressed by a symmetry-dependent number of independent components that can be determined from resistance measurements along different directions of the sample. The in-plane resistivity components can be easily characterized using several well-known methods, while up to now the out-of-plane resistivity cannot be determined without any additional sample treatment or modification, if a material can only be prepared in thin-film form.

Therefore, a novel direct and parameter-free method is developed in this thesis for the accurate determination of the out-of-plane resistivity without any further treatment of the sample. A multi-probe scanning tunneling microscope is used to carry out 4-probe transport measurements with variable probe spacings. The observation of the crossover from the 3D electronic transport regime for small spacings between the probes to the 2D regime for large spacings enables the determination of both in-plane and perpendicular-to-plane resistivities. After working out the analytical description of the method, the experimental procedures for measuring electronic transport properties with a multi-probe scanning tunneling microscope are described, in particular the influences of sample size and shape, surface morphology and grain size, probe-sample contact size and as well as the main experimental error sources.

Using this method, a first direct and parameter-free measurement of anisotropic elec-

trical resistivity of a magnetic $(\text{Cr}_{0.5}\text{Mn}_{0.5})_2\text{GaC}$ MAX phase film is presented. The observation of the crossover between the 3D and 2D transport case enables the simultaneous determination of in-plane and out-of-plane resistivities from a single sample and yields a large anisotropy. The out-of-plane resistivity exceeds the in-plane resistivity by a factor of about 500, which is a consequence of the complex bonding scheme of MAX phases. The determined resistivity ratio gives a better and quantitative insight into the interplay of crystalline structure, bonding structure, and electronic transport.

Additionally, $(\text{Cr}_{2/3}\text{Ho}_{1/3})_2\text{AlC}$ crystallites, which belong to the i-MAX phases with in-plane chemical ordering, are investigated. The results give clear evidence for both out-of-plane and in-plane anisotropic resistivity. The in-plane anisotropy is a consequence of the chemical ordering of the transition and rare-earth atoms. The weaker out-of-plane anisotropy compared to conventional MAX phases corroborates predictions of less anisotropic band structures for i-MAX phases. These measurements represent the first characterization of anisotropic resistivity in an i-MAX phase and furthermore give proof-of-principle for the determination of the entire resistivity tensor of a material with orthorhombic or higher symmetry through 4-probe electronic transport measurements of a single thin or crystalline sample.

Contents

1. Introduction	1
2. Theory of resistivity measurements	7
2.1. Determination of a resistivity via a 2-probe setup	7
2.2. 4-point transport measurements on isotropic thin-film samples	10
2.3. Crossover between the 2D and 3D transport case	14
2.4. Crossover for arbitrary probe positioning	17
2.5. Summary and conclusions	24
3. Extension to anisotropic resistivity	27
3.1. Anisotropic resistivity	27
3.2. Simultaneous measurement of in-plane and out-of-plane resistivity components	31
3.3. Measurement of in-plane anisotropic transport behaviour	33
3.4. Measurement of out-of-plane as well as in-plane anisotropic transport behavior	37
3.5. Summary and conclusions	38
4. Experimental setup	39
4.1. LT Nanoprobe	40
4.1.1. 4-probe Scanning Tunneling Microscope	41
4.1.2. The piezo control	43
4.1.3. Scanning Tunneling Microscopy	44
4.1.4. Scanning Electron Microscope	48
4.1.5. Software for transport measurements	50
4.2. Probe preparation	51
4.3. Preparation chamber	54
4.4. Summary	57
5. Characterization of electronic transport measurements by using a 4-probe STM	59
5.1. Measurements of ex- and in-situ test resistors	59
5.2. Procedure of in-situ transport measurements	62
5.3. Discussion of errors	63
5.4. In-situ 4-probe measurement of a thin Cu stripe	66
5.4.1. Impact of positioning precision and contact radii	67

5.4.2. Impact of thin-film quality	69
5.5. In-situ 4-probe measurement of a thin Au film – Test of arbitrary probe configurations	71
5.6. Summary and conclusions	74
6. Electronic transport properties of a magnetic MAX phase – $(\text{Mn}_{0.5}\text{Cr}_{0.5})_2\text{GaC}$	77
6.1. Theoretical Background	77
6.2. Experimental procedure	79
6.3. Electronic transport measurements	80
6.3.1. Determining the in-plane resistivity component measured on a 40 nm thin-film sample	80
6.3.2. Determining ρ_c/ρ_{ab} via the crossover function measured on a 155 nm thin-film sample	82
6.4. Summary and conclusions	85
7. Electronic transport properties of an i-MAX phase – $(\text{Cr}_{2/3}\text{Ho}_{1/3})_2\text{AlC}$	87
7.1. Theoretical background	87
7.2. Experimental procedure	89
7.3. Characterization of the in-plane resistivities components	91
7.4. Determination of the out-of-plane resistivity component	95
7.5. Conclusion	98
8. Summary and Outlook	101
A. Additional Data	105
A.1. Calibration of the PCUs	105
A.2. Measurements of ex-situ and in-situ test resistors	108
Bibliography	113
List of Own Publications	123
Acknowledgment	125
Erklärung	127
Curriculum Vitae	129

1. Introduction

A fundamental physical property of any solid is the resistivity ρ which is the inverse conductivity. This physical quantity is often used to classify solids into insulators, semiconductors and metals due to the range of the resistivity values from $10^{-8} \Omega\text{cm}$ to $10^{16} \Omega\text{cm}$ for a metal to an insulator material [1, 2]. Hence, it is important to characterize this quantity for any material since the resistivity has a great influence on several parameters of many devices, like transistors or light emitting diodes [3, 4]. This essential determination of the resistivity can be easily achieved by measuring the resistance R of a material according to the well known proportionality between the resistivity and the measured resistance [2, 4].

Determining the resistance is typically accomplished by measuring the voltage drop between two electrodes while a known current is injected. Thereby, the measured resistance always contains the contact resistance of the electrodes which are in series with the intrinsic resistance to be measured [4]. To avoid this problem, Wenner [5] found in 1915 a suitable way to determine the resistance of a material, which was first used for geophysical transport measurements. To neglect the contact resistance he suggested a 4-point setup with an in-line geometry for directly measuring the intrinsic resistance, whereby two probes apply the current while two other ones measure the voltage drop [4]. From 1915 on this method has been established in the geophysical community, while years later, in 1954, Valdes [6] used an in-line 4-probe transport measurement for the determination of a semiconductor wafer resistance and since 1975 this method has been established in the microelectronic industry [7].

However, since the discovery of the 4-point transport measurement there has been a huge development of different methods leading to several contact configurations like the famous van der Pauw setup where a sample is contacted at the edges [8]. For small spacings between the contact points down to the micrometer range one can use monolithic microscopic 4-point probes fixed in-line on a cantilever which are already commercially available [9]. For variable probe spacings this scheme can be extended to 12-probes [9, 10]. By selecting different probes for a 4-point configuration the probe spacing can be varied. The lithographically fabricated multi-probe technique exhibits the great advantage of a very precise probe spacing, e.g. a probe spacing of $1.5 \mu\text{m}$ comprises an error of less than 1.5 nm [11]. The fine determination of the spacing is related to a novel position correction method [11]. Finally, as known today, the 4-point technique is an easy and precise way for the direct determination of an intrinsic resistance by neglecting the contact resistances for which many methods have been developed ranging from macroscale 4-probes to microscale lithographically produced multi-probe techniques as well as different contact configurations like the van der Pauw method.

Nevertheless, the probe spacings achieved today in the micrometer range must be further developed down to the nanometer range. According to the never ending progress in science, microelectronics evolves into nanoelectronics where it is now essential to provide measuring setups for the nanoscale regime [12]. Especially for future applications of such novel nanoelectronic devices the conductivity should be well characterized, wherefore lithographic methods are the standard approach to contact those small structures for performing electronic transport measurements.

A suitable, alternative approach is the use of a multi-probe Scanning Tunneling Microscope (in the following STM) where each probe is able to contact well defined parts of nanostructures with spacings even in the nanometer range [13]. The advantage of this variable probe positioning goes at the expense of an positioning error and also leads to an error in probe spacings. The lithographically fabricated multi-probe technique comprises better defined probe spacings but not a variable positioning and additionally needs the use of correction methods. Furthermore, the flexibility for different probe spacings of the lithographically fabricated multi-probes is limited whereas a multi-probe STM exhibits more degrees of freedom for probe positioning. Hence, a 4-probe STM is a more suitable approach for transport measurements on nanostructures. The approach of a 4-probe STM exhibits several advantages (compare to [12]):

- in-situ contacting of a sample in Ultra High Vacuum (in the following UHV) conditions allowing transport measurements free from contaminations.
- possibility to freely position the probes in three dimensions.
- probing can be non-invasive (high-ohmic).

For those reasons there is a growing community of multi-probe STM users [12]. While the first multi-probe STM was introduced in 2001 by Shiraki et al. [14], today there are several home-built multi-probe STM designed [15–22] as well as there are commercial multi-probe STM available [23–26]. The ongoing progress in developing the 4-probe STM to the multimeter in the nanoscale regime [12] leads to a constant increase of possible applications of multi-probe STM and opens new possible investigation methods for transport measurements. Just to mention only a few publications, starting with transport measurements of semiconductor materials to disentangle the bulk conductivity from the surface conductivity [27–30] and the characterization of transport properties of topological insulators [31–33], over novel STM imaging like the scanning tunneling potentiometry [34, 35], and ending with the characterization of resistivity of different nanostructures [13, 36].

In recent years layered materials such as graphite, hexagonal boron nitride, and transition metal dichalcogenides (TMD) have attracted great interest due to their intriguing fundamental properties and their high potential in a variety of applications [37, 38]. The nanolaminated structures comprise covalently coordinated two-dimensional atomic layers that are stacked and van der Waals-bonded in the third dimension. This highly

anisotropic crystallographic structure exhibits anisotropic electronic, optical, and mechanical properties of the bulk material, where additionally the van der Waals-bonding type allows the stabilization, synthesis, handling, investigation, and application of single or a few atomic layers, so-called 2D materials, which are mostly prepared as isolated objects or in van der Waals heterostructures [38]. A further class of layered materials was rediscovered in 1990 [39], namely the ternary carbides and nitrides with the general formula $M_{n+1}AX_n$ (in the following just called MAX phase) with $n = 1, 2, 3$ where M is an early transition metal, A is a A-group element mostly of the main groups 13-16, and X is C or N. Firstly discovered in the early 1960 [40] it is nowadays in the point of interest due to numerous applications ranging from electrical contacts, magnetic sensors, spintronics devices to coating materials in aerospace technology [40–42] which arise from the complex crystallographic structure of the MAX phases. The nanolaminated and anisotropic atomic structures consist of predominantly covalent bonds, both within the two-dimensional building blocks formed by M-X-M planes as well as between them. As a consequence, MAX phases combine metallic and ceramic properties in a unique manner [43]. Furthermore, selective etching of the A atoms from the MAX phase results in MXenes, i.e. $M_{n+1}X_nT_x$ 2D materials, where T represents surface terminations [44]. All this has recently triggered the development of an environmentally friendly, sustainable, and cheap MAX phase synthesis scheme that can be scaled up to industrial scale [45].

Nevertheless, a key property for further investigations and applications of such layered materials is the electrical conductivity. According to the anisotropic bonding structure in layered materials an anisotropic electronic transport is expected as will be described in this thesis in particular for the MAX phases. In the past 40 years several methods have been developed for measuring anisotropic transport properties of a sample [4, 46], mostly connected to the investigation of high temperature superconductors [47] and low-dimensional organic and metallic conductors [48, 49].

Anisotropic electronic transport can be characterized by introducing the resistivity as a second rank tensor. Due to the nature of a second ranked tensor the resistivity can be expressed by a symmetry-dependent number of independent components that can be determined from resistance measurements along different directions of the sample. The in-plane resistivity components (in the following ρ_a and ρ_b) can be easily characterized by using several modified versions of the van der Pauw technique [46, 50–53]. A further sensitive investigation of ρ_a and ρ_b can be achieved by a 4-probe STM using a square formation of the probes and rotating this configuration [4, 54].

These straight-forward methods for the determination of an in-plane anisotropic transport behaviour become quite challenging if the out-of-plane resistivity component (in the following ρ_c) has to be taken into account as well. Using van der Pauw techniques for characterizing ρ_c the sample must be cut to get access to another crystalline surface orientation, which is inherently difficult for samples synthesized in thin-film form [46]. In particular, as long as a material is predominantly growing in (0001) orientation (i.e. in c -direction), thus preventing the determination of in-plane and out-of-plane resistivity components by measuring two suitably oriented thin-film samples. Nevertheless, there

are some alternative strategies for measuring ρ_c . A direct measurement of ρ_c [55] requires sufficiently large single crystals that are difficult to grow and patterning efforts to achieve a specific device structure [56], which allows to extract ρ_c using geometric correction factors. Individual grains of a polycrystalline sample can be addressed with transmission electron microscopy measuring the dielectric response in different crystalline orientations by electron energy loss spectroscopy. Subsequent semiclassical Drude–Lorentz modeling then provides an estimate of the resistivity anisotropy [57, 58]. The comparison of in-plane resistivity measurement of a (0001)-oriented thin film (yielding the in-plane resistivity) with the resistivity of a polycrystalline bulk sample (which depends on both in-plane and out-of-plane resistivity) allows deducing the resistivity anisotropy in an effective medium approach [59, 60]. However, the large parameter space of effective medium models as well as different defect and impurity densities result in large uncertainties.

Considering that layered materials synthesized as thin films predominantly grow in (0001) orientation, a measuring procedure for the characterization of ρ_a , ρ_b and ρ_c should be based on only one single epitaxial or at least oriented thin-film sample and neither require a specific device structure, nor a comparison of samples with different microstructure, or modelling of transport or effective medium properties. Therefore, in this thesis a parameter-free experimental procedure to accurately and simultaneously measure the in-plane as well as out-of-plane resistivity components from a single (0001)-oriented thin-film sample is presented.

The here introduced method is based on 4-probe measurements with variable probe spacings realized by a 4-probe STM featuring for all four probes individual lateral positioning and well-defined vertical approach to the contact regime. Due to variable spacing s between the probes, the observation of the crossover from the so called 3D transport regime for small s compared to the film thickness to the 2D transport regime for large s enables the determination of both in-plane and out-of-plane resistivity components. This scheme is applied to the magnetic MAX phase $(\text{Mn}_{0.5}\text{Cr}_{0.5})_2\text{GaC}$ yielding a large ratio for the out-of-plane over the in-plane resistivity components. These results have been published in Flatten et al. [61]. For this publication the MAX phase samples were produced at the Linköping University in Sweden by A. Petruhins, member of the group of J. Rosen. The theory behind this project (the direct determination of the out-of-plane resistivity component) and the measurements were performed entirely by myself in the group of D. E. Bürgler at the Research Center Jülich. The group of M. Farle of the University Duisburg-Essen, especially U. Wiedwald supported this project.

For the description of this novel measuring method for determining the resistivity components the thesis is structured as follows. In **chapter 2** the theoretical background is given for a 4-point transport measurements on a homogeneous thin-film sample with isotropic resistivity. First, the relation between ρ and the resistance measured by a 2-point setup is shown, and the so-called 2D and 3D transport cases are introduced. Then this scheme is extended to a 4-probe transport measurement. The crossover between 2D and 3D case is explained for a 4-probe configuration. In literature this crossover between

the 2D and 3D case has so far only been verified for an in-line configuration of the four contact probes with equidistant spacing. Therefore, in this thesis the crossover is also treated for arbitrary probe configurations.

In **chapter 3** the electronic 4-point transport measurement is extended to an anisotropic resistivity by applying a coordinate transformation suggested by van der Pauw to the transport equations known for an isotropic resistivity. The properties of the transformed crossover function are used for the direct determination of in-plane and out-of-plane resistivity components. The resulting principle is the key for analysing resistivity anisotropy of thin-film materials. Additionally, the well-known characterization of anisotropic in-plane resistivity components is discussed.

Chapter 4 shows the experimental setup, and the 4-probe STM (LT Nanoprobe from Scienta Omicron [23]) is introduced. The top mounted Scanning Electron Microscope (in the following SEM), which is used together with the STM for the probe positioning, is explained as well as the setup for transport measurements. In addition, the self-made probe preparation is presented, which is a key for precise transport measurements on small length scales. The chapter ends with a description of the preparation chamber that is utilized for cleaning samples and probes.

In **chapter 5** first transport measurements are performed, starting with ex-situ and in-situ measurements of several test resistors to verify the functionality of the setup. The procedure of in-situ 4-probe transport measurements and possible errors emerging during a measurement (e.g. probe positioning errors) are discussed. Experimental results for transport measurements on thin copper and gold films demonstrate the impact of the quality of the contacts and verify the derived equations for describing transport measurements with arbitrary probe positioning.

Chapter 6 presents the main result of this thesis, namely the measurement of the anisotropic electronic transport properties of the magnetic MAX phase $(\text{Mn}_{0.5}\text{Cr}_{0.5})_2\text{GaC}$, for which $\rho_a = \rho_b \neq \rho_c$. In-plane and out-of-plane resistivities are measured simultaneously and reveal a large anisotropy ratio $\rho_c/\rho_{ab} = 525 \pm 49$. Additionally, a further thin-film MAX phase sample is investigated to verify again the equations for arbitrary probe configurations.

Chapter 7 introduces the so called i-MAX phases which exhibit both out-of-plane as well as in-plane anisotropic behaviour of the resistivity. For the in-plane anisotropy the measured sample yields a small anisotropy ratio of $\rho_a/\rho_b = 1.46 \pm 0.13$. On this basis, this chapter describes the possible investigation of thin films with $\rho_a \neq \rho_b \neq \rho_c$ and discusses the challenges of the model derived in this work for the measurement of all components of the resistivity tensor.

Finally, the thesis closes with a brief conclusion on the results and an outlook, both given in **chapter 8**.

2. Theory of resistivity measurements

In this chapter the measurement of the resistivity ρ of a material is discussed, where the determination of ρ can be achieved by measuring the resistance R . At first, section 2.1 introduces the dependency between R and ρ for a 2-probe electronic transport measurement. Here, the so-called 2D and 3D transport regimes are introduced and explained. Afterwards, this principle is extended to determine the sample resistivity via the 4-point technique for a thin-film sample (section 2.2). In section 2.3 the crossover between the 2D and 3D transport regimes is described, first only for an in-line configuration of the probes with equidistant spacings. In section 2.4 I derive a general equation for the crossover for arbitrary probe positioning. This extension of the previous work has been published in Flatten et al. [61]. The influences of different probe spacings and configurations on the crossover are discussed.

2.1. Determination of a resistivity via a 2-probe setup

In general, an isotropic resistivity ρ of a conducting material is defined by an applied electric field E and a current density J with the ratio

$$\rho = \frac{E}{J}, \quad (2.1)$$

which is nothing else than Ohm's law. For this case ρ can be expressed as a scalar according to the assumption of an isotropic resistivity. The unit of ρ is $[\Omega \text{ cm}]$, if the electric field is given in $[\text{V cm}^{-1}]$ and the current density in $[\text{A cm}^{-2}]$. From the experimental point of view the resistivity depends on the sample resistance $R = V/I \propto \rho$. Hence, an easy measuring setup is given by a typical 2-probe electronic transport measurement as shown in figure 2.1 (a) where the voltage drop ΔV is measured over two contacting probes injecting an defined current I . Thereby, the total measured resistance always contains the contact resistances R_C connected in series to R . In the following a model is introduced to describe the measured voltage drop V between the two probes supposing a homogeneous material with an isotropic resistivity. The contact area and penetration depth of the probes are considered. The distribution of the current density is discussed leading to the so-called 2D and 3D transport regimes. Considering this, Ohm's law is used to calculate the potential at a certain distance r from the injection point. This principle is extended to the 2-probe setup yielding the dependency between R and ρ .

Now, two STM probes contact the sample. Due to small lateral separations adjustable by a multi-probe STM the contact radius of the probes cannot be neglected. Hence, a spherical contact with a defined radius r_C of each probe is assumed leading to the setup

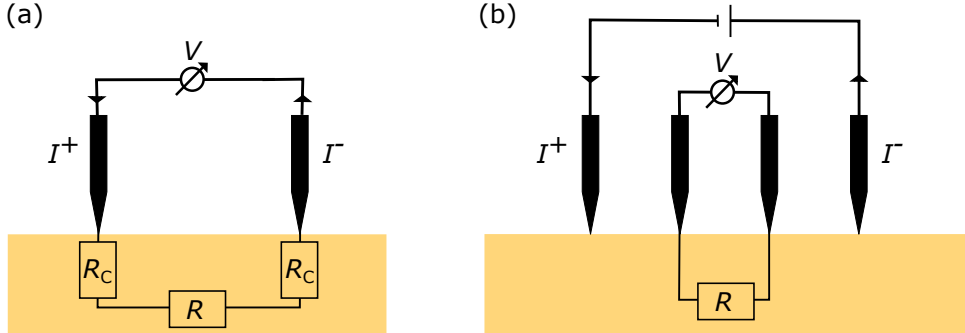


Figure 2.1.: Sketch of a 2-probe configuration measuring R_C and R connected in series (a), while a 4-probe configuration (b) allows to determine R directly.

sketched in figure 2.2 (a) where two STM probes are contacting a sample with a fixed probe spacing s . The measured voltage drop is given by $\Delta V = (\Phi_1 - \Phi_2)$.

Before considering the potentials, the distribution of the current density J at the injection points is discussed which depends strongly on the geometry of the sample. If the sample thickness is much larger than the spacing s , the sample appears as a semi-infinite bulk. A spherical spreading of J at the injecting point of the probe can be assumed yielding the so-called 3D transport case [see fig. 2.2 (b)]. Due to the spherical spreading the current density at a distance r is given by $J = I/(2\pi r^2)$, where I is the injected current. In contrast to the 3D case, the 2D transport regime occurs for a sample thickness much smaller than s . The sample appears as an infinite two-dimensional sheet whereby a cylindrical spreading of the current can be assumed. This spreading results in $J = I/(2\pi r t)$ where t is the sample thickness as shown in figure 2.2 (c). Considering J for the 3D transport case the electric field $E(r)$ can be expressed as follows

$$E(r) = \rho J(r) = \frac{\rho I}{2\pi r^2} = -\frac{d\Phi}{dr}. \quad (2.2)$$

Integrating this term the potential Φ at a point r is given by

$$\begin{aligned} \int_{\Phi_C}^{\Phi(r)} d\Phi &= - \int_{r_C}^r \frac{\rho I}{2\pi r^2} dr \\ \Rightarrow \Phi(r) &= \Phi_C - \frac{\rho I}{2\pi} \cdot \left(\frac{1}{r_C} - \frac{1}{r} \right), \end{aligned} \quad (2.3)$$

where Φ_C is the potential at the spherical edge of the probe.

The potential $\Phi(r)$ is now applied to the 2-probe setup where the sign of the current has to be considered. The measured potential Φ_1 (Φ_2) at probe 1 (2) depends on the

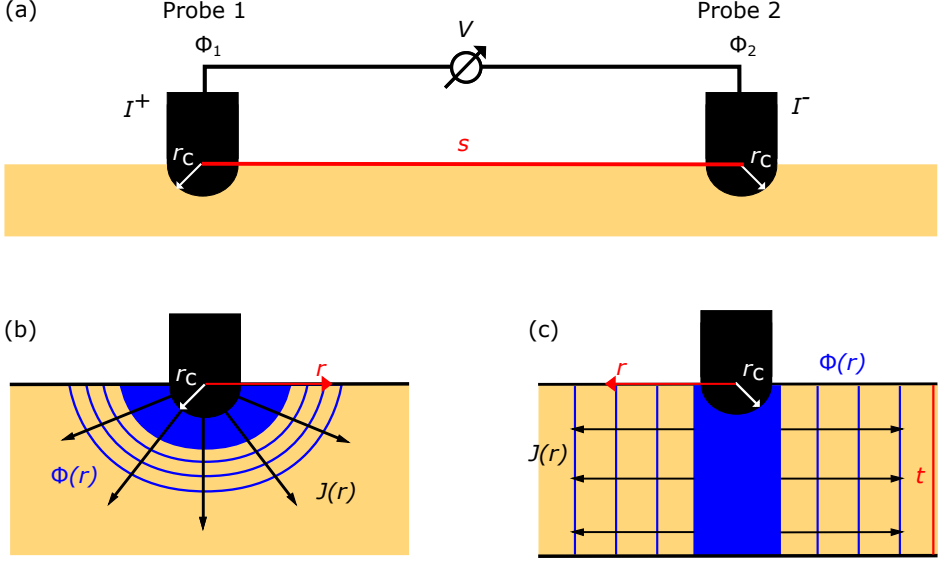


Figure 2.2.: (a) Scheme of an electronic 2-probe transport measurement assuming a spherical contact of the probes with a radius r_C and a spacing s between them. (b) Potential and current density profiles of a 3D bulk and (c) a 2D sheet sample assuming a spherical contact point. Adapted from [4, 62].

current from the opposite probe 2 (1). Referring to figure 2.2 (a) for Φ_1 the injected current I from probe 2 is negative. For Φ_2 the applied current from probe 1 is taken into account which is positive. The potential is determined from the spherical edge of probe 1 to the edge of probe 2 [see fig. 2.2 (a)], meaning that the distance r is given by the spacing s minus twice the contact radius r_C . Taking this into account, Φ_1 becomes

$$\begin{aligned} \int_{\Phi_C}^{\Phi_1} d\Phi &= - \int_{r_C}^{s-r_C} \frac{-I\rho}{2\pi r^2} dr \\ \Rightarrow \Phi_1 &= \Phi_C + \frac{\rho I}{2\pi} \cdot \left(\frac{1}{r_C} - \frac{1}{s-r_C} \right), \end{aligned} \quad (2.4)$$

and similarly Φ_2 but with the opposite sign of I

$$\Phi_2 = \Phi_C - \frac{\rho I}{2\pi} \cdot \left(\frac{1}{r_C} - \frac{1}{s-r_C} \right). \quad (2.5)$$

Using equations (2.4) and (2.5) the measured voltage drop ΔV can be determined leading

to the resistance $R_{3D}^{2P} = \frac{\Delta V}{I}$ for the 3D transport case measured by a 2-probe setup

$$\begin{aligned}\Delta V &= \Phi_1 - \Phi_2 = \frac{\rho I}{\pi} \cdot \left(\frac{1}{r_C} - \frac{1}{s - r_C} \right) \\ \Rightarrow R_{3D}^{2P} &= \frac{\Delta V}{I} = \frac{\rho}{\pi} \cdot \left(\frac{1}{r_C} - \frac{1}{s - r_C} \right).\end{aligned}\quad (2.6)$$

Obviously, R_{3D}^{2P} depends on $1/s$ as well as the contact radius. Now, the same steps are performed for the 2D transport regime. The sample appears as an infinite sheet, thus the potential at the surface and the bottom of the sample are the same at each distance r . This is a consequence of the confinement of the potential lines in the direction of the sample thickness. Considering J for the 2D case the electric field $E(r)$ and the potential Φ can be expressed by

$$E(r) = \rho J(r) = \frac{\rho I}{2\pi r t} = -\frac{d\Phi}{dr}.\quad (2.7)$$

By integration, a logarithmic dependence of the potential on the distance r is obtained for the 2D transport case:

$$\begin{aligned}\int_{\Phi_C}^{\Phi} d\Phi &= -\int_{r_C}^r \frac{\rho I}{2\pi t r} dr \\ \Rightarrow \Phi &= \Phi_C - \frac{\rho I}{2\pi t} \cdot \ln\left(\frac{r_C}{r}\right).\end{aligned}\quad (2.8)$$

Performing the same steps as done in equations (2.4) to (2.6) for the 3D case to calculate the potentials Φ_1 and Φ_2 for the 2D transport case leads to the resistance R_{2D}^{2P} measured by a 2-probe setup

$$\begin{aligned}\Delta V &= \Phi_1 - \Phi_2 = \frac{\rho I}{\pi t} \cdot \ln\left(\frac{s - r_C}{r_C}\right) \\ \Rightarrow R_{2D}^{2P} &= \frac{\rho}{\pi t} \cdot \ln\left(\frac{s - r_C}{r_C}\right).\end{aligned}\quad (2.9)$$

R_{2D}^{2P} exhibits a logarithmic dependency on s . However, this model obviously diverges for both transport regimes when the contact radius is neglected ($r_C = 0$). Hence, always some assumptions are required for the size and shape of the contact areas for the 2-probe electronic transport measurement [2]. A further disadvantage of the 2-probe measurement setup is the influence of the contact resistance which can be neglected by using a 4-probe configuration.

2.2. 4-point transport measurements on isotropic thin-film samples

The introduced 2-probe electronic transport measurement will now be extended to a 4-probe configuration assuming again a homogeneous material with an isotropic resistivity.

The sample is contacted by four probes with the co-called Valdes configuration [6] which is a typical 4-point configuration used in numerous experiments. The probes are adjusted in an in-line arrangement with equidistant probe spacing, where typically the current is injected by the two outer probes while the voltage drop is measured by the inner ones [refer to fig. 2.1 (b)]. Assuming a high impedance for both voltage probes, i.e. no current flow between them, yields directly the determination of the sample resistance without detrimental influence of the contact resistances, which is a great advantage in comparison to the 2-probe setup.

In the following the 3D transport case is derived for a 4-probe setup wherefore at first the potential at probes 2 and 3 is discussed. Determining the voltage drop between the probes $\Delta V = \Phi_2 - \Phi_3$ delivers an equation for the measured resistance in the 3D transport case. This can be further simplified by neglecting the contact resistance and choosing equidistant probe spacings. Afterwards, the same is performed for the 2D transport case. Finally, both transport cases are compared to each other.

At first, again the 3D transport case is considered supposing a thick sample for the spherical spreading of the current density. The voltage drop is defined by the potential difference $\Delta V = \Phi_2 - \Phi_3$. As shown in figure 2.3, Φ_2 at probe 2 (respectively Φ_3 at probe 3) is given by the injected current density from probe 1 with the spacing s_1 (s_3) as well as from probe 4 with the spacing s_2 (s_4):

$$\begin{aligned} \int_{\Phi_C}^{\Phi_2} d\Phi &= - \left(\int_{r_C}^{s_1-r} \frac{\rho I}{2\pi r^2} dr - \int_{r_C}^{s_2-r} \frac{\rho I}{2\pi r^2} dr \right) \\ \Rightarrow \Phi_2 - \Phi_C &= \frac{\rho I}{2\pi} \left(\frac{1}{s_1 - r_C} - \frac{1}{s_2 - r_C} \right) \end{aligned} \quad (2.10)$$

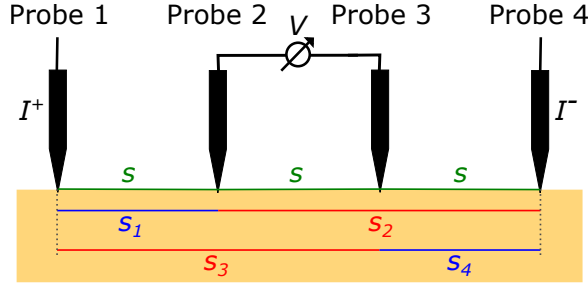


Figure 2.3.: Scheme of an in-line 4-probe measurement with equidistant probe spacing s (green marked). The assignment of the probe spacings s_i is indicated for the case that the current is injected through the outer probes 1 and 4 and the voltage drop is measured between the inner probes 2 and 3. Adapted from [4].

Note, that probe 1 applies a positive current and probe 4 a negative one for the here shown case and thus Φ_3 has the following form

$$\Phi_3 - \Phi_C = \frac{\rho I}{2\pi} \left(\frac{1}{s_3 - r_C} - \frac{1}{s_4 - r_C} \right). \quad (2.11)$$

In analogy to the 2-probe setup the resistance for an in-line 4-probe transport measurement $R_{3D}^{4P} = \frac{\Delta V}{I} = \frac{\Phi_2 - \Phi_3}{I}$ is given by

$$R_{3D}^{4P} = \frac{\rho}{2\pi} \left[\left(\frac{1}{s_1 - r_C} - \frac{1}{s_2 - r_C} \right) - \left(\frac{1}{s_3 - r_C} - \frac{1}{s_4 - r_C} \right) \right]. \quad (2.12)$$

If the probe spacings are much larger than the contact radius, for the 4-probe transport measurement a point contact ($r_C = 0$) can be assumed and

$$R_{3D, r_C = 0}^{4P} = \frac{\rho}{2\pi} \left[\left(\frac{1}{s_1} - \frac{1}{s_2} \right) - \left(\frac{1}{s_3} - \frac{1}{s_4} \right) \right]. \quad (2.13)$$

For the case of equidistant probe spacings s ($s = s_1 = s_4$ and $2s = s_2 = s_3$; see fig. 2.3) equations (2.12) and (2.13) simplify to

$$R_{3D}^{4P, s} = \frac{\rho}{\pi} \left(\frac{1}{s - r_C} - \frac{1}{2s - r_C} \right), \quad (2.14)$$

$$R_{3D, r_C = 0}^{4P, s} = \frac{\rho}{2\pi s} \equiv R_{3D}. \quad (2.15)$$

As can be seen for the simplified measured resistance considering the 3D transport case R_{3D} just depends on the spacing s . Next, the 2D transport case is considered when the sample thickness t is much smaller than the probe spacing $t \ll s$. Following the same steps as in the 3D case delivers an expression for the potentials $\Phi_{2,3}$:

$$\Phi_2 - \Phi_C = \frac{\rho I}{2\pi t} \cdot \ln \left(\frac{s_2 - r_C}{s_1 - r_C} \right), \quad (2.16)$$

$$\Phi_3 - \Phi_C = \frac{\rho I}{2\pi t} \cdot \ln \left(\frac{s_4 - r_C}{s_3 - r_C} \right). \quad (2.17)$$

For the 2D case the resistance for an in-line 4-probe transport measurement $R_{2D}^{4P} = \frac{\Delta V}{I} = \frac{\Phi_2 - \Phi_3}{I}$ with contact radius r_C and without contact radius $r_C = 0$ is given by

$$R_{2D}^{4P} = \frac{\rho}{2\pi t} \cdot \ln \left(\frac{(s_2 - r_C) \cdot (s_3 - r_C)}{(s_1 - r_C) \cdot (s_4 - r_C)} \right), \quad (2.18)$$

$$R_{2D, r_C = 0}^{4P} = \frac{\rho}{2\pi t} \cdot \ln \left(\frac{s_2 s_3}{s_1 s_4} \right). \quad (2.19)$$

For an equidistant probe spacing $s = s_1 = s_4$ and $2s = s_2 = s_3$ equations (2.18) and (2.19) can be again simplified to

$$R_{2D}^{4P, s} = \frac{\rho}{\pi t} \cdot \ln \left(\frac{2s - r_C}{s - r_C} \right), \quad (2.20)$$

$$R_{2D, r_C=0}^{4P, s} = \frac{\rho \ln(2)}{\pi t} = \text{const} \equiv R_{2D}. \quad (2.21)$$

Interestingly, the simplified resistance R_{2D} is independent of s , but depends on the sample thickness t .

These dependencies of the 2D as well as 3D case can be explained pictorially as shown in figure 2.4. Here, four probes are placed along an in-line configuration with equidistant probe spacing, and the black lines indicate the current distributions. For the 2D transport regime the sample appears as an infinite sheet, as it is bounded by the finite thickness. On the other hand the sample for the 3D transport regime appears as an semi-infinite bulk. The cylindrical current spreading of the 2D case arises from the compression of the current distribution at the sample bottom due to the finite film thickness, and R is independent of s , but inversely proportional to t [see fig. 2.4 (a)]. The $1/s$ dependency for the 3D case originates from the spherical current spreading into the sample as shown in figure 2.4 (b). At first glance, this dependency on s is against common experience, which is based mostly on measurements of long wires with $R \propto s$. In the 2D case, the increase of resistance along each current path for increasing s is compensated by the increasing number of current paths [4]. For the 3D case, the

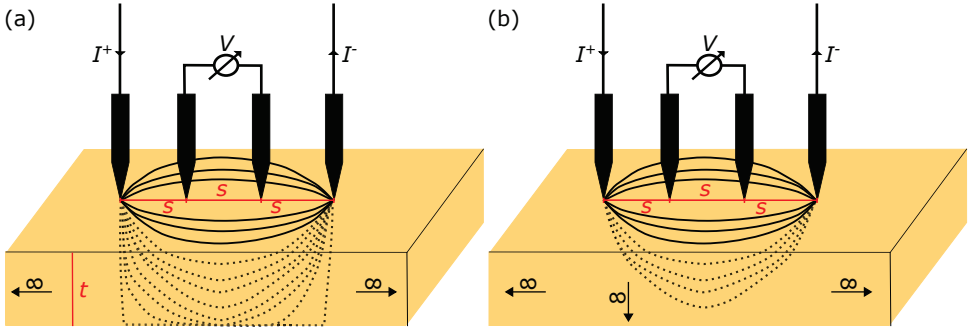


Figure 2.4.: Scheme of the current distributions for a 4-probe electronic transport measurement. The black lines indicate the current distributions on the surface (solid lines) and into the sample (dashed lines). The latter are compressed due to the finite thickness t for the 2D transport case (a), but exhibit an unperturbed spherical spreading for the 3D transport case (b). Adapted from [4].

increase of resistance per current path is overcompensated by the increasingly larger number of current paths due to the spreading of the current deep into the sample.

The 2D and 3D transport regimes are limiting cases that occur depending on the relative magnitude of probe spacing and sample thickness. For $t \ll s$ the sample appears as a sheet and exhibits the 2D transport case while the 3D case occurs for $t \gg s$. However, the sample thickness in an experiment is fixed unless multiple samples are considered. The special feature of a 4-probe STM to be able to vary the probe spacing allows measuring the 2D case for large s and the 3D case for smaller s on one single sample. For intermediate values of s the crossover between the two transport regimes can be addressed as explained in the next section.

2.3. Crossover between the 2D and 3D transport case

The crossover function to be derived in this section is a correction factor for intermediate film thicknesses $t \approx s$. As derived later in this thesis (chapter 3) the crossover function is key for measuring the components of an anisotropic resistivity tensor. But for now, a homogeneous sample with isotropic ρ is considered.

For simplicity reasons an in-line 4-probe transport measurement with equidistant probe spacing s , fixed sample thickness t and negligible radius $r_C = 0$ is assumed. The crossover from the 3D to the 2D case is accomplished by varying s instead of t from $s \ll t$ to $s \gg t$ as sketched in figure 2.5 (a) and (b). The crossover point from the 3D behavior [equation (2.15)] with $R_{3D} \propto s^{-1}$ to the 2D case [equation (2.21)], for which R_{2D} is independent on s , occurs at

$$\zeta = \frac{s}{t} = \frac{1}{2 \ln(2)}, \quad (2.22)$$

where $R_{3D} = R_{2D}$ [refer to equations (2.15) and (2.21)]. For s/t ratios exceeding this value, the finite thickness of the sample affects and compresses the spatial current distribution as sketched in figure 2.5 (a) and (b).

For a given geometry of current injection, the potential is given by the Laplace equation. Albers and Berkowitz presented an approximate solution for the crossover from the 3D to the 2D regime for the measured resistance [63]:

$$R = \frac{\rho}{\pi t} \cdot \ln \left(\frac{\sinh(t/s)}{\sinh(t/2s)} \right). \quad (2.23)$$

For an isotropic resistivity ρ and the resistance R measured by a 4-probe setup using the Valdes configuration, this equation is in literature often rewritten to the form

$$\rho = \left(\frac{\pi R t}{\ln(2)} \right) \cdot F. \quad (2.24)$$

Here, F is considered as a correction factor for samples with finite thickness [4] and is defined as

$$F = \frac{\ln(2)}{\ln\left(\frac{\sinh\left(\frac{t}{s}\right)}{\sinh\left(\frac{t}{2s}\right)}\right)}. \quad (2.25)$$

The accuracy of the Albers-Berkowitz approximation [equation (2.23)] or the correction factor F [equation (2.25)], respectively, has been investigated experimentally [64] and theoretically [65, 66]. It was found that the approximate resistance values deviate by less than 10% near the crossover point ζ and much less elsewhere.

The correction factor F is plotted in figure 2.5 (c) together with the limiting 3D and 2D cases versus the ratio t/s . The crossover point ζ^{-1} is also indicated. The correction factor F shows for $t/s \ll 1$ a constant course due to the asymptotic behavior $\sinh(x) \approx x$ for $x \rightarrow 0$ and thus $F = 1$ expresses the 2D transport case [see left part of F in fig. 2.5 (c)]. This approximation holds with an error of around 1% for $t/s < 1/5$. For $t/s \gg 1$, the asymptotic behavior $\sinh(x) \approx e^x/2$ for $x \rightarrow \infty$ yields $F \approx 2 \ln(2) s/t$,

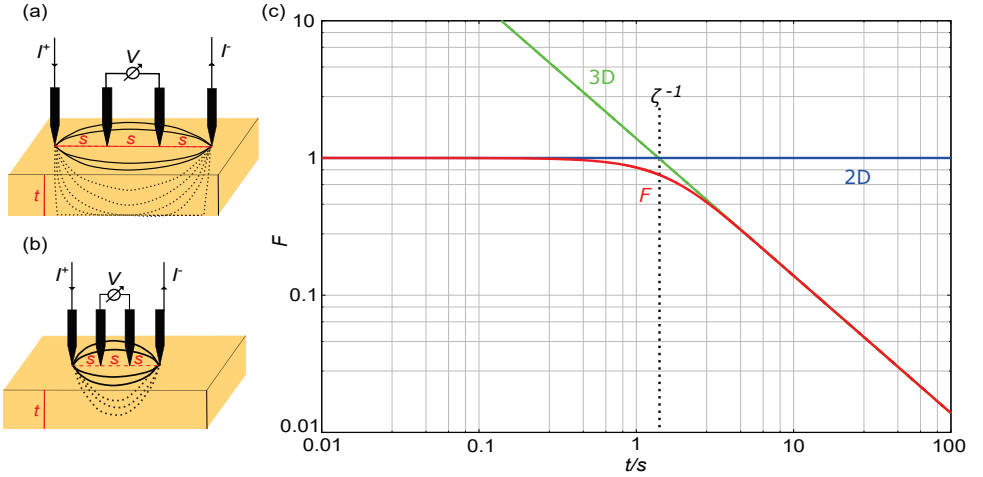


Figure 2.5.: Crossover between 3D and 2D electron transport regimes. Sketches of 4-probe transport measurements in a film with thickness t and equidistant probe spacing s for the 2D regime (a) and 3D regime (b) according to [61]. Dashed lines indicate the current distribution, which is unperturbed spherical in the 3D case, but compressed at the sample bottom in the 2D case. In (c) the crossover function F (red line) between the 3D (green line) and the 2D (blue line) transport case is plotted versus the ratio t/s . Additionally, the crossover point ζ^{-1} is indicated.

which reduces the expression to the 3D transport case [see right part of F in fig. 2.5 (c)]. This approximation holds with an error of about 1% for $t/s > 4$.

Finally a homogeneous sample with isotropic resistivity $\rho = 1 \mu\Omega\text{m}$ and a film thickness $t = 100 \text{ nm}$ is considered as a practical example for a typical measurement of ρ . The crossover function (2.23) as well as the equations for the 2D (2.21) and 3D (2.15) transport case are plotted in figure 2.6 where a perfect 4-probe transport measurement is considered by neglecting any contact radius. The resistance values R are of the order of 1 to 10Ω . The 3D (green line) and the 2D (blue line) transport cases show the expected behaviour $R \propto 1/s$ (3D) and $R = \text{const.}$, independent of s (2D). The crossover function (red curve) follows the 3D curve for probe spacings in the nanometer range and the 2D curve for large spacings (micrometer range). Additionally, the crossover functions for an isotropic sample with a thickness of $t = 50 \text{ nm}$ (dotted line) and $t = 500 \text{ nm}$ (dashed line)

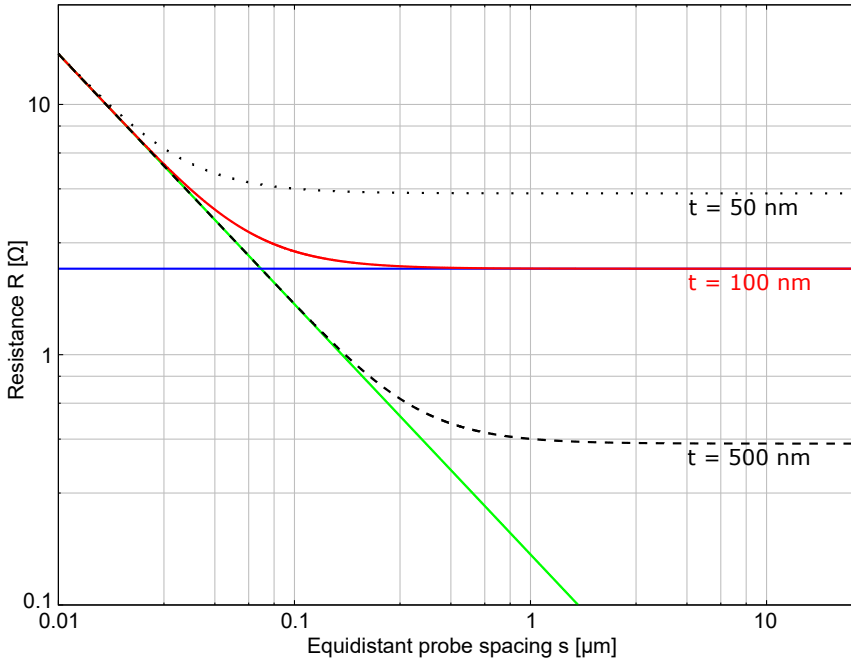


Figure 2.6.: Resistance R versus equidistant probe spacing s for a 4-probe measurement of a $t = 100 \text{ nm}$ thin-film sample with isotropic resistivity $\rho = 1 \mu\Omega\text{m}$ reveals the crossover between the 3D (green line) and the 2D (blue line) transport case. Crossover curves for a sample thickness of $t = 50 \text{ nm}$ (dotted line) and $t = 500 \text{ nm}$ (dashed line) are plotted, too.

line) are plotted, too. Both curves follow the 3D curve which just depends on the probe spacing but not on the thickness. However, the crossover functions level out at different resistance values for different sample thicknesses, because the 2D transport case depends on t but is independent of s . For constant ρ , the crossover point shifts for increasing sample thickness to larger s , whereby the values of R in the 2D limit decrease. From the experimental point of view, larger probe spacings are much easier to achieve. Therefore, thicker samples (several 100 nm-range) are more likely desired for the observation of the crossover point, which will be shown in chapters 3 and 6 to be an elegant means for the measurement of an out-of-plane resistivity component in the case of an anisotropic resistivity tensor.

2.4. Crossover for arbitrary probe positioning

In the last sections only the Valdes configuration is considered, but not how the crossover behaves for an arbitrary probe positioning. The advantage of a 4-probe STM comprises an individual probe positioning wherefore the previous derived equations must be generalized for arbitrary probe positioning. A more general expression will be given below for the 2D and 3D transport cases where the contact radius is neglected.

An arbitrary probe positioning is shown in figure 2.7 (a). The current is still injected and drained through probes 1 and 4, respectively, and the voltage drop is measured between probes 2 and 3. The spacings are now defined by the vectors \vec{r}_i according to the general formalism used in literature [12]. The vectorial notation leads to the following expressions for R_{3D} and R_{2D} :

$$R_{3D} = \frac{\rho}{2\pi} \left[\frac{1}{|\vec{r}_2 - \vec{r}_1|} - \frac{1}{|\vec{r}_4 - \vec{r}_2|} - \frac{1}{|\vec{r}_3 - \vec{r}_1|} + \frac{1}{|\vec{r}_4 - \vec{r}_3|} \right], \quad (2.26)$$

$$R_{2D} = \frac{\rho}{2\pi t} \ln \left[\frac{|\vec{r}_3 - \vec{r}_1| \cdot |\vec{r}_4 - \vec{r}_2|}{|\vec{r}_2 - \vec{r}_1| \cdot |\vec{r}_4 - \vec{r}_3|} \right]. \quad (2.27)$$

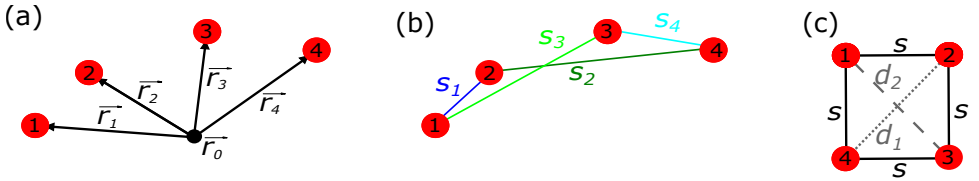


Figure 2.7.: Different probe configurations for a 4-probe transport measurement: (a) general non-linear configuration using vector notation for the spacings (\vec{r}_i), (b) arbitrary positioning with a scalar notation of the spacings (s_i), and (c) square configuration. Adapted from [12].

2. Theory of resistivity measurements

The vectors \vec{r}_i have a common reference point \vec{r}_0 . Note, that these equations also hold for any arbitrary probe assignment to current source and voltmeter; the voltage probes do not have to be between the current probes [12]. The previously introduced equations for R_{3D}^{4P} (2.12), $R_{3D,r_C=0}^{4P}$ (2.13), R_{2D}^{4P} (2.18), and $R_{2D,r_C=0}^{4P}$ (2.19) are already valid for an arbitrary probe configuration. As shown in figure 2.7 (a) and (b) the scalar spacings s_i indicate the same distances as those described by the vectorial notations. They can also be used for the derivation of the above mentioned equations in section 2.2.

In figure 2.7 (c) a further frequently used probe configuration is shown, namely a square configuration with an edge length of s . Assuming that probes 1 and probe 4 are the current probes and probes 2 and 4 measure the voltage drop, the probes spacing are then defined by $s = s_1 = s_4$ and $d_1 = d_2 = s_2 = s_3 = \sqrt{2}s$. This leads to following equations for R in the 2D and 3D case, again assuming $r_C = 0$ (see also [4])

$$R_{3D}^{\text{square}} = \rho \frac{(2 - \sqrt{2})}{2\pi s}, \quad (2.28)$$

$$R_{2D}^{\text{square}} = \rho \frac{\ln(2)}{2\pi t}. \quad (2.29)$$

While the measured resistance can be easily be expressed for an arbitrary probe configuration, the (approximate) crossover function in equation (2.23) is only valid for an in-line configuration with equidistant probe spacing s [63]. In a 4-probe STM setup, however, each probe can be positioned individually, which allows arbitrary probe configurations, e.g. by varying the position of at least one probe starting from an equidistant in-line configuration or by performing measurements in a square configuration. In the following a generalized crossover function is derived for arbitrary probe positioning and discussed for three specific configurations. This derivation and discussion has been published in the supplemental material of my own publication [61].

Tehrani et al. [66] derived an expression for a 4-probe transport measurement of a thin-film sample on a non-conducting substrate with arbitrary probe positioning, where the voltage drop is measured between probes 2 and 3 [see fig. 2.7 (b)]:

$$\begin{aligned} \Delta V_{23} &= [V(s_1) + V(s_2)] - [V(s_3) + V(s_4)] \\ &= \frac{I\rho}{2\pi} \left[\int_0^\infty [J_0(ks_1) - J_0(ks_2) - J_0(ks_3) + J_0(ks_4)] \coth(kt) dk \right]. \end{aligned} \quad (2.30)$$

Here, J_0 is the zeroth-order Bessel function of the first kind. The $\coth(kt)$ -term originates from the boundary conditions due to the finite film thickness, i.e. the boundaries towards vacuum and the non-conducting substrate. Equation (2.30) can now be rewritten as

$$\begin{aligned} \Delta V_{23} &= \frac{I\rho}{2\pi} \left[\int_0^\infty [J_0(ks_1) - J_0(ks_2)] \coth(kt) dk + \right. \\ &\quad \left. \int_0^\infty [J_0(ks_4) - J_0(ks_3)] \coth(kt) dk \right], \end{aligned} \quad (2.31)$$

where the first (second) term represents the potential at probe 2 (3) due to the currents injected at probes 1 and 4. Similar to Albers and Berkowitz [63], the integrals can be simplified by removing the Bessel functions, but limiting the integration limits with a for the time being unknown function $f(1/s_i)$, such that the values of the definite integrals are approximately preserved,

$$\Delta V_{23} = \frac{I\rho}{2\pi} \left[\int_{f(1/s_2)}^{f(1/s_1)} \coth(kt) dk + \int_{f(1/s_3)}^{f(1/s_4)} \coth(kt) dk \right]. \quad (2.32)$$

The function f can be obtained by considering the limiting case of an infinitely thick sample ($t \rightarrow \infty$), for which the boundary condition $\coth(kt) \rightarrow 1$. The integrals in equation (2.31) can then be solved analytically

$$\Delta V_{23}^\infty = \frac{I\rho}{2\pi} \left[\int_0^\infty [J_0(ks_1) - J_0(ks_2)] dk + \int_0^\infty [J_0(ks_4) - J_0(ks_3)] dk \right] \quad (2.33)$$

$$= \frac{I\rho}{2\pi} \cdot \left(\frac{1}{s_1} - \frac{1}{s_2} - \frac{1}{s_3} + \frac{1}{s_4} \right). \quad (2.34)$$

As expected for an semi-infinite sample, this is the expression for the 3D transport regime with non-equidistant probe spacings as previously derived in equation (2.13). Accordingly, we define $f(1/s_i) = 1/s_i$ and solve the integrals in equation (2.32) to obtain a general expression for resistance R in a 4-probe transport measurement with arbitrary probe positioning that solely depends on the spacings s_i defined in figure 2.7 (b) and the film thickness t ,

$$R = \frac{\Delta V_{23}}{I} = \frac{\rho}{2\pi t} \cdot \ln \left(\frac{\sinh(t/s_1) \sinh(t/s_4)}{\sinh(t/s_2) \sinh(t/s_3)} \right). \quad (2.35)$$

Obviously, for equidistant probe spacing $s_1 = s_4 = s$ and $s_2 = s_3 = 2s$, equation (2.35) reduces to the crossover equation (2.23) deduced by Albers and Berkowitz [63]. The following presents and discusses the crossover function in equation (2.35) for three specific probe configurations and compares them to the general 3D and 2D expressions given in equations (2.13) and (2.19), respectively.

First, the previously mentioned square arrangement of the probes is considered as shown in the inset of figure 2.8. Equations (2.28) and (2.29) express the measured resistance for the limiting 3D and 2D cases. The crossover function in equation (2.35) becomes

$$R^{\text{square}}(s) = \frac{\rho}{\pi t} \cdot \ln \left(\frac{\sinh(t/s)}{\sinh(t/\sqrt{2}s)} \right). \quad (2.36)$$

In figure 2.8, these three expressions [equations (2.28), (2.29), and (2.36)] are plotted for typical values of the isotropic resistivity $\rho = 1 \mu\Omega\text{m}$ and the sample thickness $t = 200 \text{ nm}$.

2. Theory of resistivity measurements

Obviously, the expressions for the 2D (blue line) and 3D (green line) regimes fit well to the respective parts of the crossover function (red line). The black curve shows the crossover function for the in-line configuration with equidistant probe spacing, which, in comparison to the square configuration, reveals about twice as large resistance values. Furthermore, the crossover point ζ^{square} of the square configuration is determined by setting $R_{3\text{D}}^{\text{square}} = R_{2\text{D}}^{\text{square}}$,

$$\zeta^{\text{square}} = \frac{s}{t} = \frac{2 - \sqrt{2}}{\ln(2)} = 0.845. \quad (2.37)$$

This is slightly larger than the crossover point of the in-line configuration [see equa-

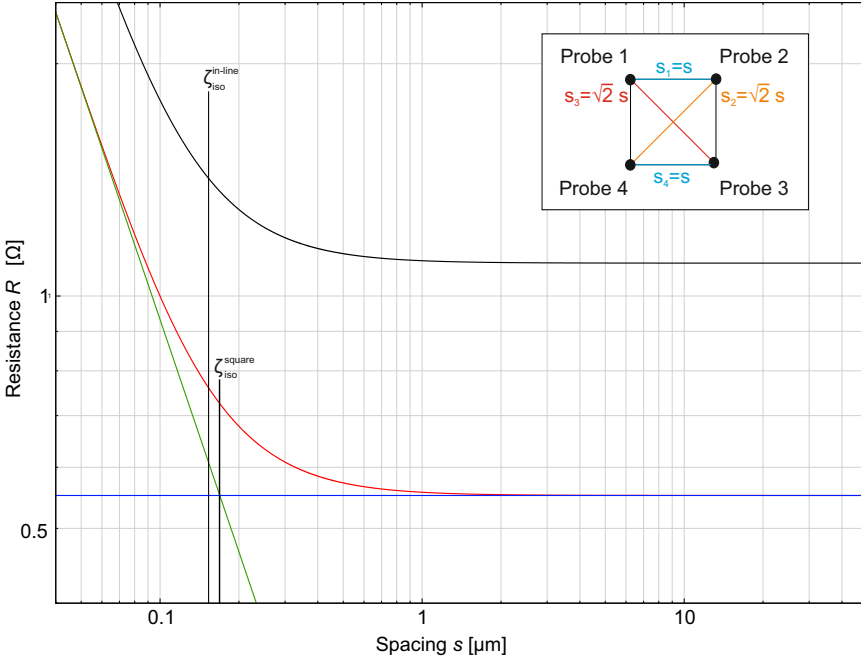


Figure 2.8.: Crossover function (red line) for the square configuration as sketched in the inset. The green and blue lines represent the corresponding 3D ($R_{3\text{D}}^{\text{square}}$) and 2D ($R_{2\text{D}}^{\text{square}}$) transport regimes, respectively. The black line shows for comparison the crossover function for the in-line configuration with equidistant probe spacing s according to equation (2.23). The crossover point ζ for both curves is also indicated. All curves are plotted for resistivity $\rho = 1 \mu\Omega\text{m}$ and sample thickness $t = 200 \text{ nm}$.

tion (2.22)]

$$\zeta^{\text{in-line}} = \frac{s}{t} = \frac{1}{2 \ln(2)} = 0.721. \quad (2.38)$$

From the experimental point of view (and also limited by the setup used in this thesis, where the injected current is limited to a maximum of 30 mA) the current is often chosen in the 1 mA range or below to obtain a gentler, thermally less influenced measurement. Since larger resistance values are easier to measure due to the correspondingly larger voltage drop, the in-line configuration is preferred, although the square configuration shifts the crossover point to slightly larger probe spacings.

Next, an in-line configuration is considered, where the current probes 1 and 4 are the two outer ones and the voltage probes 2 and 3 the two inner ones. The measurement is performed by simultaneously moving the two inner probes in opposite directions, see inset of figure 2.9. Starting from a fixed, equidistant probe spacing s between all probes, the probe spacings s_i change according to

$$s_1 = s_1 + x \quad (2.39)$$

$$s_2 = s_2 - x \quad (2.40)$$

$$s_3 = s_3 - x \quad (2.41)$$

$$s_4 = s_4 + x. \quad (2.42)$$

This leads to the expressions for the crossover function $R^{\text{inner probes}}$ as well as for the 2D and 3D transport regimes

$$R^{\text{inner probes}}(x) = \frac{\rho}{2\pi t} \cdot \ln \left(\frac{\sinh(t/[s_1 + x]) \sinh(t/[s_4 + x])}{\sinh(t/[s_2 - x]) \sinh(t/[s_3 - x])} \right) \quad (2.43)$$

$$R^{\text{3D, inner probes}}(x) = \frac{\rho}{2\pi} \cdot \left(\frac{1}{s_1 + x} - \frac{1}{s_2 - x} - \frac{1}{s_3 - x} + \frac{1}{s_4 + x} \right) \quad (2.44)$$

$$R^{\text{2D, inner probes}}(x) = \frac{\rho}{2\pi t} \cdot \ln \left(\frac{(s_2 - x)(s_3 - x)}{(s_1 + x)(s_4 + x)} \right). \quad (2.45)$$

All three expressions are plotted in figure 2.9 starting at equidistant probe spacings $s_1 = s_4 = s = 50 \mu\text{m}$ and $s_2 = s_3 = 2s = 100 \mu\text{m}$, $\rho = 1 \mu\Omega\text{m}$, and $t = 200 \text{ nm}$. Obviously, $R^{\text{inner probes}}$ (red line) becomes zero at $x = 25 \mu\text{m}$, where probes 2 and 3 meet in the center of the in-line configuration. For negative values of x probes 2 and 3 are moving apart from each other towards the outer probes 1 and 4, respectively. For $x = -50 \mu\text{m}$, the inner probes reach the outer ones. Obviously, the 2D transport curve (blue line) describes the crossover function very well in the entire physically meaningful x -range. Only, for $x < -47 \mu\text{m}$ there is a small, hardly visible deviation, where the 3D transport curve (green line) contributes weakly. This behavior is due to the large distance between the current probes 1 and 4 ($3s \gg t$) that leads to a cylindrical current spreading

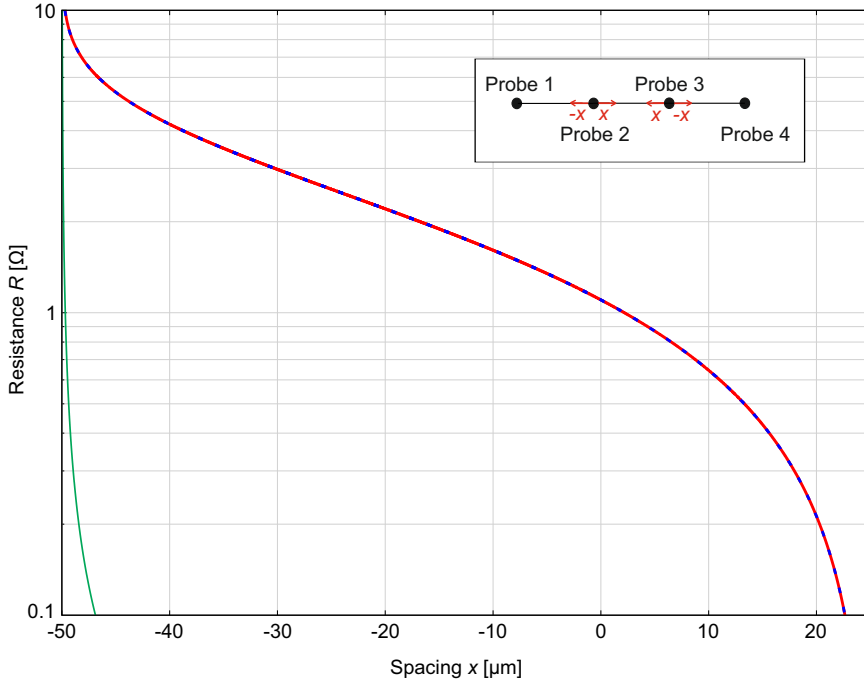


Figure 2.9.: Crossover function (red line) for the in-line configuration with variable positions of the voltage probes and an initial equidistant probe spacing $s = 50 \mu\text{m}$ as sketched in the inset. The green and blue lines represent the corresponding 3D ($R^{3\text{D}}, \text{inner probes}$) and 2D ($R^{2\text{D}}, \text{inner probes}$) transport regimes, respectively. All curves are plotted for resistivity $\rho = 1 \mu\Omega\text{m}$ and sample thickness $t = 200 \text{ nm}$.

in the thin film independent of the positions of the voltage probes 2 and 3. Only in the very vicinity of the current injection points (radius $\approx t$) is the current spreading spherically distorted, which gives rise to a weak 3D-type contribution. Therefore, this measurement procedure is not useful for the observation of the 2D/3D crossover for experimentally feasible probe spacings.

Finally, again an in-line configuration is considered, but now the outer current probes 1 and 4 are moved, while keeping the positions of the voltage probes 2 and 3 constant, see inset of figure 2.10. Taking the results in figure 2.9 into account, the starting equidistant probe spacing is chosen rather small ($s = 50 \text{ nm}$) such that the distance between the current probes $d_{1,4}$ can be varied in the range from $d_{1,4} < t$ to $d_{1,4} \gg t$. For increasing x , the probe spacings s_i change according to

$$s_1 = s_1 + x \quad (2.46)$$

$$s_2 = s_2 + x \quad (2.47)$$

$$s_3 = s_3 + x \quad (2.48)$$

$$s_4 = s_4 + x. \quad (2.49)$$

This leads to the expressions for the crossover function $R^{\text{outer probes}}$ as well as for the 2D and 3D transport regimes

$$R^{\text{outer probes}}(x) = \frac{\rho}{2\pi t} \cdot \ln \left(\frac{\sinh(t/(s_1 + x)) \sinh(t/(s_4 + x))}{\sinh(t/(s_2 + x)) \sinh(t/(s_3 + x))} \right) \quad (2.50)$$

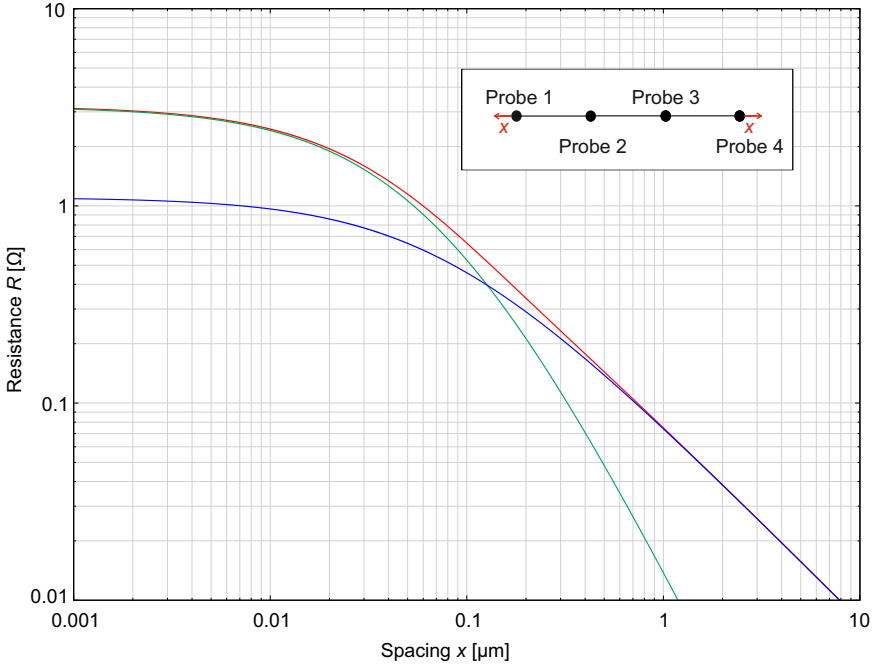


Figure 2.10.: Crossover function (red line) for the in-line configuration with variable positions of the current probes and an initial equidistant probe spacing $s = 50$ nm as sketched in the inset. The green and blue lines represent the corresponding 3D ($R^{\text{3D, outer probes}}$) and 2D ($R^{\text{2D, outer probes}}$) transport regimes, respectively. All curves are plotted for resistivity $\rho = 1 \mu\Omega\text{m}$ and sample thickness $t = 200$ nm.

$$R^{\text{3D, outer probes}}(x) = \frac{\rho}{2\pi} \cdot \left(\frac{1}{s_1 + x} - \frac{1}{s_2 + x} - \frac{1}{s_3 + x} + \frac{1}{s_4 + x} \right) \quad (2.51)$$

$$R^{\text{2D, outer probes}}(x) = \frac{\rho}{2\pi t} \cdot \ln \left(\frac{(s_2 + x)(s_3 + x)}{(s_1 + x)(s_4 + x)} \right). \quad (2.52)$$

All three expressions are plotted in figure 2.10 for starting equidistant probe spacings $s_1 = s_4 = s = 50$ nm and $s_2 = s_3 = 2s = 100$ nm, and $\rho = 1 \mu\Omega\text{m}$ and $t = 200$ nm. As expected, for small displacements of the current probes ($x < 20$ nm) the crossover curve $R^{\text{outer probes}}(x)$ follows the 3D behavior (green line), whereas for large displacements ($x > 1 \mu\text{m}$) the 2D regime (blue line) fits well the crossover curve. Hence, the crossover in this configuration is observable at similar minimum probe distances $d_{ij} \approx 50$ nm as in the in-line configuration with equidistant probe spacing (see black line in fig. 2.8).

Concluding this section, there are several probe configurations to characterize the crossover between the 2D and 3D transport regimes. The in-line configuration with equidistant probe spacing derived by Albers and Berkowitz [63] is experimentally and theoretically well established [64–66] and therefore used in this work. The square configuration as well as the in-line configuration with moving outer current probes are also well working solutions and require the control of similarly small probe distances. However, the in-line configuration with equidistant probe spacing yields the largest resistance values near the crossover point, making it the experimentally preferred probe configuration for this thesis.

2.5. Summary and conclusions

In this chapter I have discussed the 4-probe electronic transport measurement method as a powerful means for the measurement of the resistivity of a given material. The main advantage over 2-probe measurements is that the contact resistances do not matter, if the impedance of the voltage measurement is much larger than the intrinsic resistance of the sample. This condition is usually easy to meet. The elimination of the contact resistances from the measurement is of particular importance for investigations on the micrometer scale and below, where the control and characterization of the probe and contact properties becomes increasingly difficult. The relationship between measured resistance R and resistivity ρ depends on the probe spacing s and the sample shape, which is particularly relevant for the technologically important thin-film geometry. Thick films with $t \gg s$ behave like a semi-infinite bulk. The current distribution penetrates undisturbed spherically inside the film. This corresponds to the 3D transport regime with $R \propto \rho/s$. In thin films with $t \ll s$, however, the current distribution is compressed at the bottom boundary of the film and hence is cylindrically deformed. This limit is called the 2D transport regime with $R \propto \rho/t$. In this thesis, the crossover between these two regimes ($t \approx s$) is of particular interest. It can be described with the previously derived approximate analytical crossover function that only depends on the ratio t/s . However, so far the crossover function was only derived for the in-line alignment of the

probes with equidistant probe spacings. Hence, it does not meet the flexibility of the 4-probe STM, which, based on the individual positioning of each probe, allows a variety of tip configurations and measurement protocols based on the movement of one or more probes. Therefore, I have extended the crossover function in section 2.4 for arbitrary probe positioning. This made it possible to compare different measurement protocols (quadratic positioning, in-line positioning with moving current or voltage probes, respectively). It turned out that the in-line configuration with equidistant probe spacing is the best protocol for measuring the crossover function because it provides higher resistance values near the transition point. Therefore, this protocol will be used in the experimental part of this thesis.

In the next chapter the extension to anisotropic resistivity is carried out. It will be shown that the crossover function is the key to the direct, simultaneous and parameter-free measurement of both in-plane and out-of-plane resistivity components of a thin film with anisotropic resistivity.

3. Extension to anisotropic resistivity

This chapter introduces the determination of anisotropic resistivity, which is expressed as a second ranked tensor. By introducing the transformation of van der Pauw, relations between the components of the resistivity tensor and the measured resistance are derived in section 3.1. These equations imply quite challenging measurements to determine the anisotropic resistivity properties of a sample. Thus, different methods are introduced in the following sections. In section 3.2 the properties of the crossover function are used to determine the ratio of the out-of-plane to the in-plane resistivity component. This represents a novel method for the direct, simultaneous and parameter-free determination of both the in-plane and out-of-plane resistivity components of a thin-film sample, which I have developed and published in [61]. Section 3.3 addresses the well-known measurement of an in-plane resistivity anisotropy by 4-probe measurements. Finally, the measurement of three independent components of the resistivity tensor is briefly discussed in section 3.4.

3.1. Anisotropic resistivity

For anisotropic resistivity Ohm's law [equation (2.1)] is rewritten in vectorial form with the second rank tensor $\boldsymbol{\rho}$ whose components ρ_{ij} represent resistivities along certain directions of the solid [4]. E_i and J_i are the electric field and the density current along the i th direction of the solid, respectively [4, 67].

$$\begin{pmatrix} E_1 \\ E_2 \\ E_3 \end{pmatrix} = \begin{pmatrix} \rho_{11} & \rho_{12} & \rho_{13} \\ \rho_{21} & \rho_{22} & \rho_{23} \\ \rho_{31} & \rho_{32} & \rho_{33} \end{pmatrix} \begin{pmatrix} J_1 \\ J_2 \\ J_3 \end{pmatrix}. \quad (3.1)$$

According to crystallographic symmetries the number of independent resistivity components is nine or less. A cubic crystal is described by only one resistivity component which represents nothing else than an isotropic resistivity case [67]

$$\text{Cubic} \Rightarrow \begin{pmatrix} \rho_1 & 0 & 0 \\ 0 & \rho_1 & 0 \\ 0 & 0 & \rho_1 \end{pmatrix}. \quad (3.2)$$

Tetragonal, hexagonal as well as trigonal crystals require two independent resistivity components and orthorhombic crystals three. For the sake of completeness, it is mentioned that monoclinic symmetry requires four independent components and triclinic structures even nine [67].

$$\begin{aligned}
 \begin{array}{l} \text{Tetragonal} \\ \text{Hexagonal} \\ \text{Trigonal} \end{array} &\Rightarrow \begin{pmatrix} \rho_1 & 0 & 0 \\ 0 & \rho_1 & 0 \\ 0 & 0 & \rho_3 \end{pmatrix} & \text{Orthorhombic} &\Rightarrow \begin{pmatrix} \rho_1 & 0 & 0 \\ 0 & \rho_2 & 0 \\ 0 & 0 & \rho_3 \end{pmatrix} \\
 \text{Monoclinic} &\Rightarrow \begin{pmatrix} \rho_1 & 0 & \rho_{13} \\ 0 & \rho_2 & 0 \\ \rho_{13} & 0 & \rho_3 \end{pmatrix} & \text{Triclinic} &\Rightarrow \begin{pmatrix} \rho_{11} & \rho_{12} & \rho_{13} \\ \rho_{21} & \rho_{22} & \rho_{23} \\ \rho_{31} & \rho_{32} & \rho_{33} \end{pmatrix}
 \end{aligned} \tag{3.3}$$

As a consequence the proportionality between the measured 4-probe resistance and the resistivity described in chapter 2 for isotropic materials needs to be reformulated, since the measured 4-probe resistance along one axis in general may also depend on the other resistivity components. The situation is simplified, if the resistivity tensor is diagonal allowing for a decoupling the components of the resistivity tensor. This is the case for a maximum of three independent components [4, 51], i.e. for cubic, tetragonal, hexagonal, trigonal, and orthorhombic symmetries. For the following considerations we restrict ourselves to these symmetries. For simplicity reasons the resistivity components are named ρ_x , ρ_y and ρ_z and refer to the resistivities along the orthogonal space coordinates x , y and z . Thus, the determination of the single resistivity components is based on resistance measurements along each space coordinate.

For the treatment of an anisotropic sample van der Pauw [68] suggested a transformation of the coordinates of an anisotropic cube with edge length l onto an isotropic parallelepiped of resistivity ρ and dimensions l'_i (also refer to fig. 3.1)

$$l'_i = \sqrt{\frac{\rho_i}{\rho}} l_i \quad \text{with} \quad i = x, y, z, \tag{3.4}$$

where $\rho = \sqrt[3]{\rho_x \cdot \rho_y \cdot \rho_z}$. This transformation does not affect the resistance R as it preserves voltage and current [4, 50]. In the following the transformation of van der Pauw is applied to 4-probe measurements of a homogeneous material with resistivity tensor components ρ_x , ρ_y , ρ_z and with the probes in in-line or square configuration.

Starting with the 3D transport case the transformation $s'_x = \sqrt{\rho_x/\rho} s_x$ is obtained by assuming an in-line alignment of the probes along the x -axis of the sample. In addition, equidistant probe spacing and negligible contact radii are assumed. Applied to the R_{3D} -equation (2.15) delivers for the measured resistance $R_{3D, \text{ aniso}}^{x\text{-axis}}$

$$\begin{aligned}
 R_{3D, \text{ aniso}}^{x\text{-axis}} &= \frac{\rho}{2\pi s'_x} = \frac{\rho}{2\pi \sqrt{\rho_x/\rho} s_x} \\
 &= \frac{\sqrt{\rho_y \rho_z}}{2\pi s_x}.
 \end{aligned} \tag{3.5}$$

Here, $R_{3D, \text{ aniso}}^{x\text{-axis}}$ is just the geometric mean of the resistivity components of the other two axis [4]. Taking the sample thickness $t'_z = \sqrt{\rho_z/\rho} t_z$ into account the R_{2D} -equation

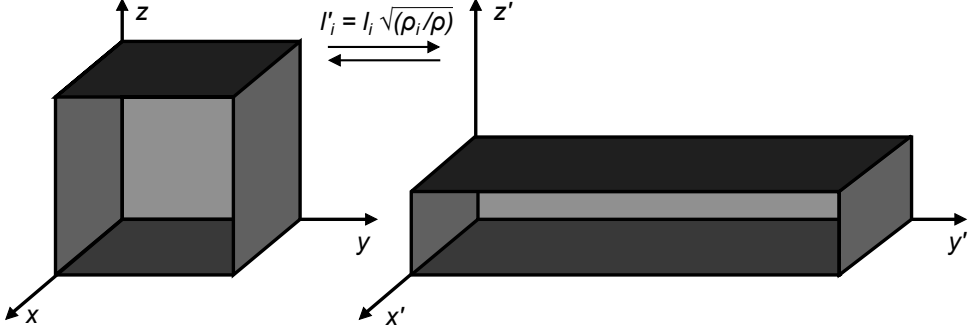


Figure 3.1.: Mapping of an anisotropic cubic sample into an equivalent isotropic parallelepiped using the van der Pauw transformation. Adapted from [4, 68].

(2.21), which only depends on the in-plane resistivity components ρ_x and ρ_y , transforms into

$$\begin{aligned} R_{2D, \text{ aniso}}^{x\text{-axis}} &= \frac{\ln(2)}{\pi t'_z} \rho = \frac{\ln(2)}{\pi \sqrt{\rho_z/\rho} t_z} \rho \\ &= \frac{\ln(2)}{\pi t_z} \sqrt{\rho_x \rho_y}. \end{aligned} \quad (3.6)$$

In comparison to the in-line configuration a square arrangement of the probes leads to a more complicated transformation. As shown in figure 3.2, the 4-probe arrangement for the anisotropic case is aligned along the x - as well as the y -axis. The equivalent configuration for the transformed geometry still depends on the x - and y -axis and thus the spacings s_i are defined as follows

$$\begin{aligned} s'_1 = s'_4 &= s \sqrt{\rho_y/\rho} \\ s'_2 = s'_3 &= s \sqrt{(\rho_x/\rho) + (\rho_y/\rho)} \\ t'_z &= t_z \sqrt{\rho_z/\rho}, \end{aligned} \quad (3.7)$$

where the original square has $s = s_1 = s_4$ and $\sqrt{2} s = s_2 = s_3$. Using equation (2.13) for an arbitrary probe positioning delivers

$$\begin{aligned} R_{3D, \text{ aniso}}^{x\text{-axis}, \square} &= \frac{\rho}{2\pi} \left[\left(\frac{1}{s'_1} - \frac{1}{s'_2} \right) - \left(\frac{1}{s'_3} - \frac{1}{s'_4} \right) \right] = \frac{\rho}{2\pi} \left[\frac{2}{s} \left(\frac{1}{\sqrt{\rho_y/\rho}} - \frac{1}{\sqrt{(\rho_x/\rho) + (\rho_y/\rho)}} \right) \right] \\ &= \frac{\sqrt{\rho_x \rho_z}}{\pi s} \left(1 - \frac{1}{\sqrt{1 + \rho_x/\rho_y}} \right). \end{aligned} \quad (3.8)$$

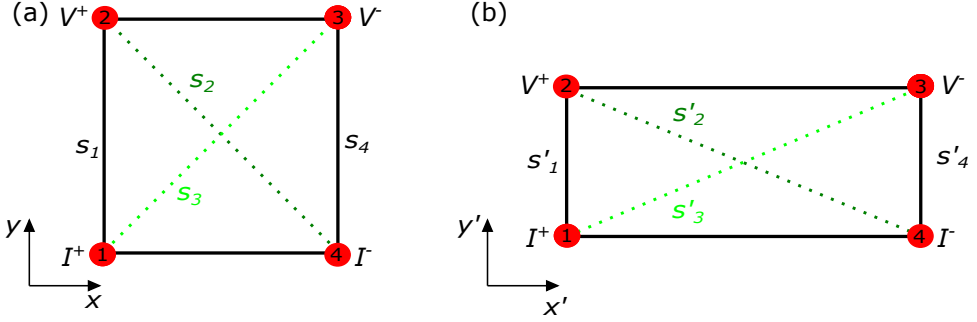


Figure 3.2.: Mapping of a 4-probe square configuration placed on an anisotropic sample (a) onto a rectangular configuration of an equivalent isotropic sample (b). Redrawn from [4].

The same steps can be done for the 2D case using equation (2.19)

$$\begin{aligned}
 R_{2D, \text{ aniso}}^{x\text{-axis, square}} &= \frac{\rho}{2\pi t'_z} \ln \left(\frac{s'_2 s'_3}{s'_1 s'_4} \right) = \frac{\rho}{2\pi \sqrt{\rho_z/\rho} t_z} \ln \left(\frac{(\rho_x/\rho) + (\rho_y/\rho)}{\rho_y/\rho} \right) \\
 &= \frac{\sqrt{\rho_x \rho_y}}{2\pi t_z} \ln \left(1 + \frac{\rho_x}{\rho_y} \right). \quad (3.9)
 \end{aligned}$$

It is obvious that for the square configuration rotated by 90° in the plane (i.e. current along y - instead of x -axis), one has to exchange ρ_x and ρ_y . Here, the same counterintuitive dependencies of the resistance appear, namely the decreasing resistance value for increasing probe spacing s in the 3D case as well as the s -independent resistance for the 2D case. The reasons are again the different current distributions [4] as discussed in section 2.2.

In the following the in-line and the square configuration are compared to each other. The resistances for in-line configuration in the 3D and 2D transport cases depend only on two different resistivity components, namely ρ_x, ρ_z or ρ_y, ρ_z for the 3D regime depending on the measurement axis, while for the 2D case ρ_x and ρ_y have to be taken into account. For the square configuration the resistance for the 3D case depends on all three resistivity components, while again for the two 2D case only ρ_x and ρ_y are relevant.

From the experimental point of view, in order to reveal information about all three tensor components ρ_x, ρ_y, ρ_z at least three measurements have to be performed. The following discussion assumes a setup with four probes in an in-line configuration with equidistant probe spacing s . The sample surface is assumed to be in the xy -plane and perpendicular to the z -axis. First, a measurement in the 3D regime along the x -axis is needed to determine the geometric mean $\sqrt{\rho_y \rho_z}$. Afterwards, the measurement axis is rotated by 90° into the y -direction to determine $\sqrt{\rho_x \rho_z}$ from an additional measurement.

The last combination $\sqrt{\rho_x \rho_y}$ can be obtained by thinning the sample or cutting a thin horizontal (xy -plane) lamella out of the sample to perform a measurement in the 2D transport limit [4], which is quite challenging if one has to measure thin-film samples.

All in all, this is not a straight-forward determination of the resistivity tensor components, since it requires sufficiently thick samples to measure first in the 3D regime and a means to thin the sample for the final measurement in the 2D regime. A novel method is introduced in the following sections, where one has to perform only two measurements on one single film of a given thickness in order to determine ρ_x , ρ_y , ρ_z without any further treatment of the sample like cutting or thinning. First, the protocol for the direct and simultaneous determination of both the out-of-plane and one in-plane resistivity components (ρ_z and e.g. ρ_x) is explained, followed by the well-known determination of the in-plane anisotropy between ρ_x and ρ_y , and ends with a description of the procedure for the measurement of ρ_x , ρ_y and ρ_z by combining the two methods.

3.2. Simultaneous measurement of in-plane and out-of-plane resistivity components

This section presents a novel method for the simultaneous determination of the in-plane and out-of-plane resistivity components from one single measurement. For the time being, an isotropic in-plane resistivity is assumed for simplicity while the out-of-plane resistivity component is different, which means $\rho_x = \rho_y \neq \rho_z$. This anisotropy is typically expected for layered materials like the MAX phases as will be discussed in chapters 6 and 7. This method is also a powerful tool to characterize an out-of-plane resistivity component in thin-film samples. The direct determination of ρ_z uses the properties of the crossover between the 2D and 3D transport case. The restriction to anisotropic in-plane resistivity will be dropped in section 3.3, which finally leads in section 3.4 to a measurement protocol for the determination of all resistivity components for the general case $\rho_x \neq \rho_y \neq \rho_z$ from a thin-film sample without any intermediate sample treatment like cutting or thinning. Parts of this chapter have been published in Flatten et al. [61].

Without loss of generality the coordinate system is defined that the sample surface lies in the xy -plane and the probes are aligned along the x -axis. If now an anisotropic resistivity ρ_z with enhanced (reduced) resistivity normal to the sample surface is considered, then the current distribution is modified in a such way that the current flow is closer to (farther from) the sample surface. Accordingly, the onset of the perturbation due to the finite thickness of the sample and the 3D-2D crossover will be shifted to smaller (larger) sample thickness. Applying the transformation of van der Pauw to the crossover function [equation (2.23)] as well as to the definition of the crossover point [equation (2.22)] yields generalized expressions for the 3D-2D transient behavior for anisotropic samples:

$$R = \frac{\rho}{\pi t'_z} \cdot \ln \left(\frac{\sinh \left(\frac{t'_z}{s'_x} \right)}{\sinh \left(\frac{t'_z}{2s'_x} \right)} \right) = \frac{\rho}{\pi \sqrt{\rho_z/\rho} t_z} \cdot \ln \left(\frac{\sinh \left(\frac{\sqrt{\rho_z/\rho} t_z}{\sqrt{\rho_x/\rho} s_x} \right)}{\sinh \left(\frac{\sqrt{\rho_z/\rho} t_z}{2\sqrt{\rho_x/\rho} s_x} \right)} \right)$$

$$\Rightarrow R = \frac{\sqrt{\rho_x \rho_y}}{\pi t} \cdot \ln \left(\frac{\sinh \left(\sqrt{\frac{\rho_z}{\rho_x}} \cdot t/s \right)}{\sinh \left(\sqrt{\frac{\rho_z}{\rho_x}} \cdot t/2s \right)} \right) \quad (3.10)$$

$$\zeta = \frac{s'_x}{t'_z} = \frac{\sqrt{\rho_x/\rho} s_x}{\sqrt{\rho_z/\rho} t_z} = \frac{1}{2 \ln(2)}$$

$$\Rightarrow \zeta = \frac{s_x}{t_z} = \frac{\sqrt{\rho_z/\rho_x}}{2 \ln(2)}. \quad (3.11)$$

The normalized and dimension-less form of equation (3.10) is plotted in figure 3.3

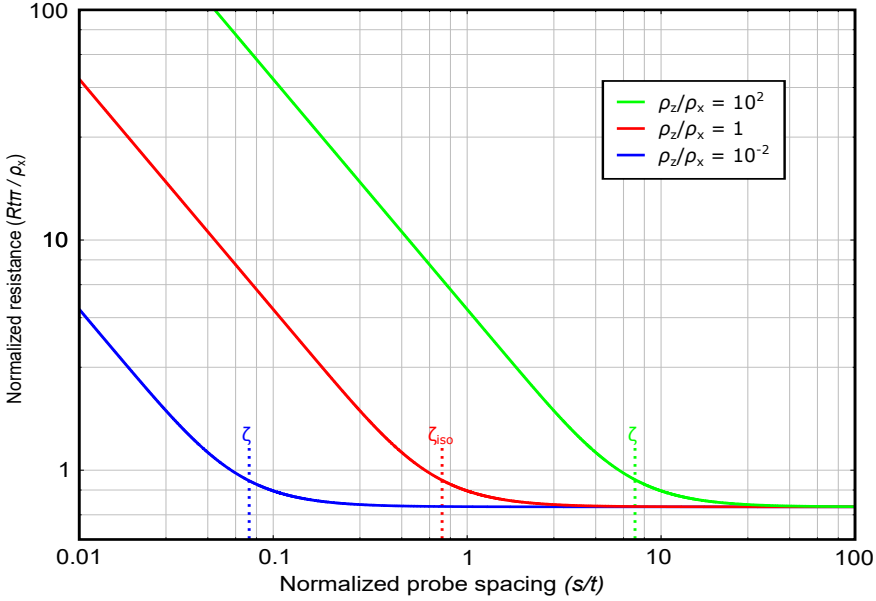


Figure 3.3.: Transient behavior of the normalized resistance as a function of the normalized probe spacing s/t according to equation (3.10) for in-line configuration and for isotropic ($\rho_z/\rho_x = 1$, red line) and different anisotropic resistivity ($\rho_z/\rho_x = 10^{-2}$, blue line; $\rho_z/\rho_x = 10^2$, green line) as indicated.

for different anisotropy ratios of the perpendicular-to-plane and in-plane resistivities $\rho_z/\rho_x = 10^2$ (green curve), 1 (red curve), and 10^{-2} (blue curve), for clarity under the assumption $\rho_x = \rho_y$. Obviously, the crossover between the 2D and 3D case depends on the anisotropy ratio, as explained above phenomenologically by the modification of the current distribution depending on ρ_z . For fixed sample thickness t , the crossover occurs for $\rho_x < (>) \rho_z$ at larger (smaller) probe spacing s . Equation (3.11) quantifies the anisotropy-dependent shift of the 3D-2D crossover point ζ depending on the anisotropic ratio of the out-of-plane and in-plane resistivity component. This modified crossover function reveals a novel and parameter-free method for a direct determination of the ratio ρ_z/ρ_x and with this ρ_z from the measurement of the 3D-2D crossover. Simultaneously, the in-plane resistivity $\rho_x = \rho_y$ can be obtained from the constant resistance value in 2D limit ($s/t \gg \zeta$), where equation (3.10) yields $R \approx \ln(2)\sqrt{\rho_x\rho_y}/(\pi t)$. The key feature of the method is that the crossover function is mapped by varying the probe spacing s rather than the film thickness t . Therefore, it enables the direct measurement of ρ_x and ρ_z of a single in-plane isotropic thin-film sample of a given thickness t .

The above procedure can be also used for arbitrary probe configurations, if the generalized crossover function [equation (2.35)] introduced in section 2.4 is taken into account. This yields for a square configuration of the probes with the edges of the square aligned along the x and y -axes

$$R_{\text{square}} = \frac{\sqrt{\rho_x\rho_y}}{\pi t} \cdot \ln \left(\frac{\sinh \left(\sqrt{\frac{\rho_z}{\rho_x}} \frac{t}{s} \right)}{\sinh \left(\sqrt{\frac{\rho_z}{\rho_x + \rho_y}} \frac{t}{s} \right)} \right), \quad (3.12)$$

if the current flows along the x -axis. For current flow along the y -axis, the indices x and y must be exchanged in equation (3.12). Equation (3.12) is plotted in figure 3.4 for different anisotropy ratios of the perpendicular-to-plane and in-plane resistivities $\rho_z/\rho_x = 10^2$ (solid green curve), 1 (solid red curve), and 10^{-2} (solid blue curve) while $\rho_x = \rho_y$. Comparing to the in-line configuration the resistance values are clearly smaller, and the crossover between the 2D and 3D cases depends strongly on the out-of-plane anisotropy ratio. As mentioned in section 2.4, larger resistance values are easier to measure, so the in-line configuration remains preferred in the experimental chapters.

3.3. Measurement of in-plane anisotropic transport behaviour

Next, the restriction to in-plane isotropy is dropped and the general case with in-plane as well as out-of-plane anisotropy, $\rho_x \neq \rho_y \neq \rho_z$, is addressed. In figure 3.4, equation (3.12) is additionally plotted for the same ρ_z/ρ_x ratios 1 and 10^2 , but now for an in-plane anisotropy $\frac{\rho_x}{\rho_y} = 10^2$ (all dashed lines). These curves deviate clearly from the in-plane isotropic ones. They are shifted to larger resistances and also show a shift of the crossover point ζ to slightly smaller normalized probe spacings s/t . Therefore, a

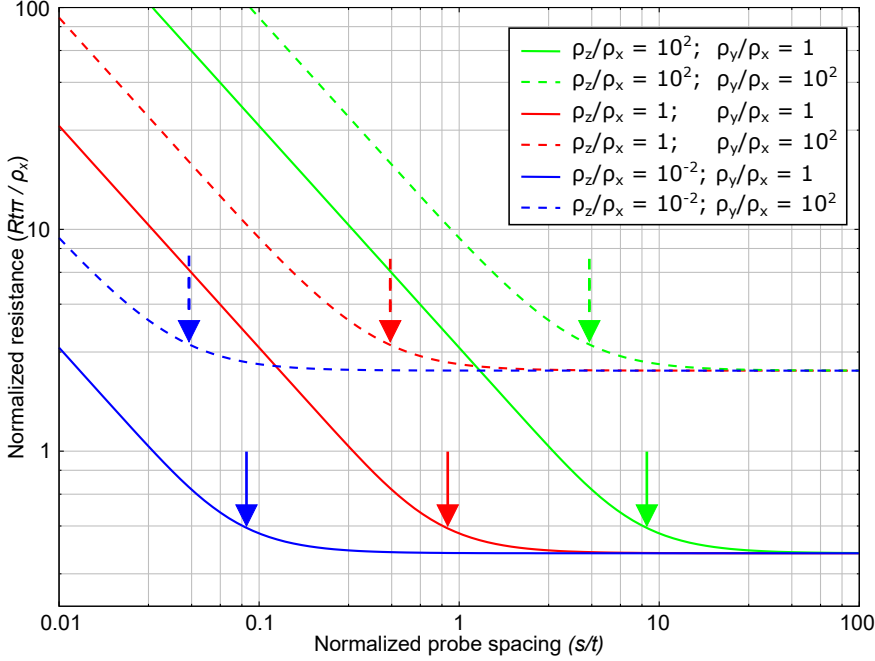


Figure 3.4.: Transient behavior of the normalized resistance as a function of the normalized probe spacing s/t according to equation (3.12) for square configuration and for isotropic ($\rho_z/\rho_x = 1$, solid red line) and different anisotropic resistivity ($\rho_z/\rho_x = 10^{-2}$, solid blue line; $\rho_z/\rho_x = 10^2$, solid green line), whereas $\rho_y/\rho_x = 1$. The dashed lines are plotted for the same ratios, but an in-plane anisotropy $\rho_y/\rho_x = 10^2$. The colored arrows indicate the different crossover points ζ .

direct determination of ρ_z is only possible, if the in-plane anisotropy ratio is known. For this reason, the characterization of the in-plane anisotropy $\rho_x \neq \rho_y$ is discussed in this section. In the 3D transport regime, the measured resistance in general depends on all three resistivity components, whereas for the 2D regime the resistance measurement is independent of ρ_z for both in-line and square configurations [see equations (3.6) and (3.9)]. However, the resistance measured in the in-line configuration does not depend on the in-plane orientation of the line connecting the probes even for strong in-plane anisotropy. This counterintuitive behavior can be seen in equation (3.6), where R only depends on the geometric mean $\sqrt{\rho_x \rho_y}$. In contrast, the measured resistance in the square configuration depends on the alignment of the the square edges with respect to

the x and y -axes. For instance, a rotation by 90° corresponds in equation (3.9) to an exchange of x and y indices, which alters for $\rho_x \neq \rho_y$ the argument of the logarithm. Hence, the square configuration in the 2D transport regime allows determining the in-plane anisotropy without knowledge of ρ_z . To this end, a square 4-probe configuration with the edges of the square aligned with the x and y axis, respectively, is considered. Two transport measurements have to be performed by rotating the probe array by 90° or by exchanging voltage and current probes to determine ρ_x and ρ_y . If the probe array is not aligned accurately, equation (3.9) cannot be applied [4] and a more general equation found by Kanagawa et al. [54] in 2003 must be used. Here, we assume for simplicity a perfect square array.

The formal description of a resistance measurement in the 2D regime with a square probe configuration on a 2D sheet with in-plane anisotropic resistivity follows the procedure described in Ref. [4]. The square probe array with edge length s is first rotated by an arbitrary angle θ with respect to one of the orthogonal resistivity components ρ_x and ρ_y . As sketched in figure 3.5 (a), the corner points A , B , C and D of the initial square are transformed onto the positions A' , B' , C' and D' with the coordinates

$$\begin{aligned} A[0, 0] &\rightarrow A'[0, 0] \\ B[s, 0] &\rightarrow B'[s \cos(\theta), s \sin(\theta)] \\ C[s, s] &\rightarrow C'[s \cos(\theta) - s \sin(\theta), s \sin(\theta) + s \cos(\theta)] \\ D[0, s] &\rightarrow D'[-s \sin(\theta), s \cos(\theta)]. \end{aligned} \quad (3.13)$$

Next the transformation of van der Pauw is applied to map the square formed by the contact points for in-plane anisotropic resistivity onto an in-plane isotropic rhomboid

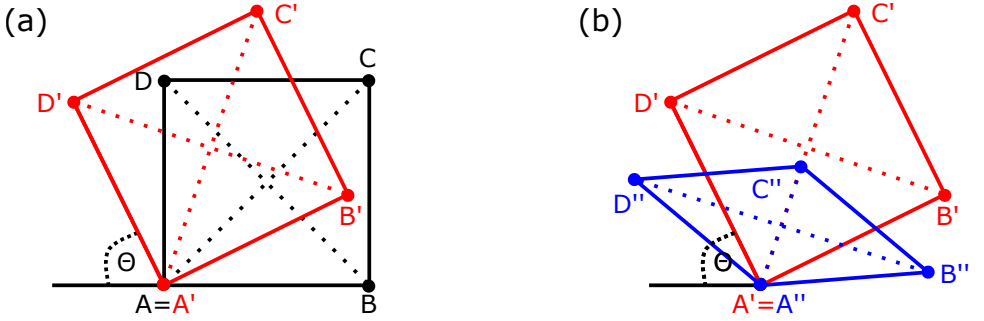


Figure 3.5.: Sketch of the rotation of a 4-probe square configuration (black) by the angle θ with respect to the x and y axes (a) and mapping of the rotated square (red) for anisotropic in-plane resistivity onto a rhomboid for isotropic in-plane resistivity (blue) (b). Adapted from [4].

(see fig 3.5 b)

$$\begin{aligned}
 A' &\rightarrow A''[0, 0] \\
 B' &\rightarrow B''[s \sqrt{\rho_x/\rho} \cos(\theta), s \sqrt{\rho_y/\rho} \sin(\theta)] \\
 C' &\rightarrow C''[s \sqrt{\rho_x/\rho} (\cos(\theta) - \sin(\theta)), (s \sqrt{\rho_y/\rho} (\sin(\theta) + \cos(\theta)))] \\
 D' &\rightarrow D''[-s \sqrt{\rho_x/\rho} \sin(\theta), s \sqrt{\rho_y/\rho} \cos(\theta)].
 \end{aligned} \tag{3.14}$$

Assuming that the current is injected by probes D (I^+) and C (I^-) and thus the voltage is measured by probes A (V^+) and B (V^-) yields the probe spacings $s_1'' = A''D''$, $s_2'' = A''C''$, $s_3'' = B''D''$, $s_4'' = B''C''$ for the rotated and transformed array,

$$\begin{aligned}
 s_1'' &= s \sqrt{\frac{\rho_x \sin^2(\theta) + \rho_y \cos^2(\theta)}{\rho}} \\
 s_2'' &= s \sqrt{\frac{\frac{\rho_x}{\rho} (\cos(\theta) - \sin(\theta))^2 + \frac{\rho_y}{\rho} (\cos(\theta) + \sin(\theta))^2}{\rho}} \\
 s_3'' &= s \sqrt{\frac{\frac{\rho_x}{\rho} (\cos(\theta) + \sin(\theta))^2 + \frac{\rho_y}{\rho} (\cos(\theta) - \sin(\theta))^2}{\rho}} \\
 s_4'' &= s \sqrt{\frac{\rho_x \sin^2(\theta) + \rho_y \cos^2(\theta)}{\rho}}.
 \end{aligned} \tag{3.15}$$

Inserting these spacings into equation (2.19) for the isotropic 2D transport case with arbitrary probe positioning, which is valid after the mapping of the anisotropic square array onto the isotropic rhombic array, yields

$$\begin{aligned}
 R(\theta, \rho_x \rho_y) &= \frac{\rho}{2\pi t \sqrt{\rho_z/\rho}} \cdot \ln \left(\left[\left(\frac{\rho_x}{\rho} \right)^2 (\cos^2(\theta) - \sin^2(\theta))^2 + \right. \right. \\
 &\quad \left(\frac{\rho_x \rho_y}{\rho^2} \right) (\cos(\theta) - \sin(\theta))^4 + \left(\frac{\rho_x \rho_y}{\rho^2} \right) (\cos(\theta) + \sin(\theta))^4 + \\
 &\quad \left. \left(\frac{\rho_x}{\rho} \right)^2 (\cos^2(\theta) - \sin^2(\theta))^2 \right] \left[\frac{\rho_x \sin^2(\theta)}{\rho} + \frac{\rho_y \cos^2(\theta)}{\rho} \right]^{-1} \right).
 \end{aligned} \tag{3.16}$$

After a few rearrangements (see Refs. [4, 54]) one obtains

$$\Rightarrow R(\theta, \rho_x \rho_y) = \frac{\sqrt{\rho_x \rho_y}}{2\pi t} \cdot \ln \left(\frac{\left(1 + \frac{\rho_y}{\rho_x} \right)^2 - 4 \cos^2(\theta) \sin^2(\theta) \left(1 - \frac{\rho_y}{\rho_x} \right)^2}{\left(\sin^2(\theta) + \frac{\rho_y}{\rho_x} \cos^2(\theta) \right)^2} \right). \tag{3.17}$$

The normalized and dimension-less form of this equation is plotted in figure 3.6 for several in-plane anisotropic ratios ranging from $\rho_y/\rho_x = 5$ to 60. For small anisotropy ratios $\rho_y/\rho_x < 20$, the largest difference between the normalized resistance values occurs for two orthogonal contact configurations, $\theta = 0^\circ$ and 90° . For large anisotropy ratios $\rho_y/\rho_x > 20$ negative values for the normalized resistance occur and the minima of the curve shift from $\theta = 0$ to 45° and 135° . The artifact of negative resistance originates from deformation of the electrostatic potential contours due to the large anisotropy, as was experimentally first verified by Kanagawa et al. in 2003 [54].

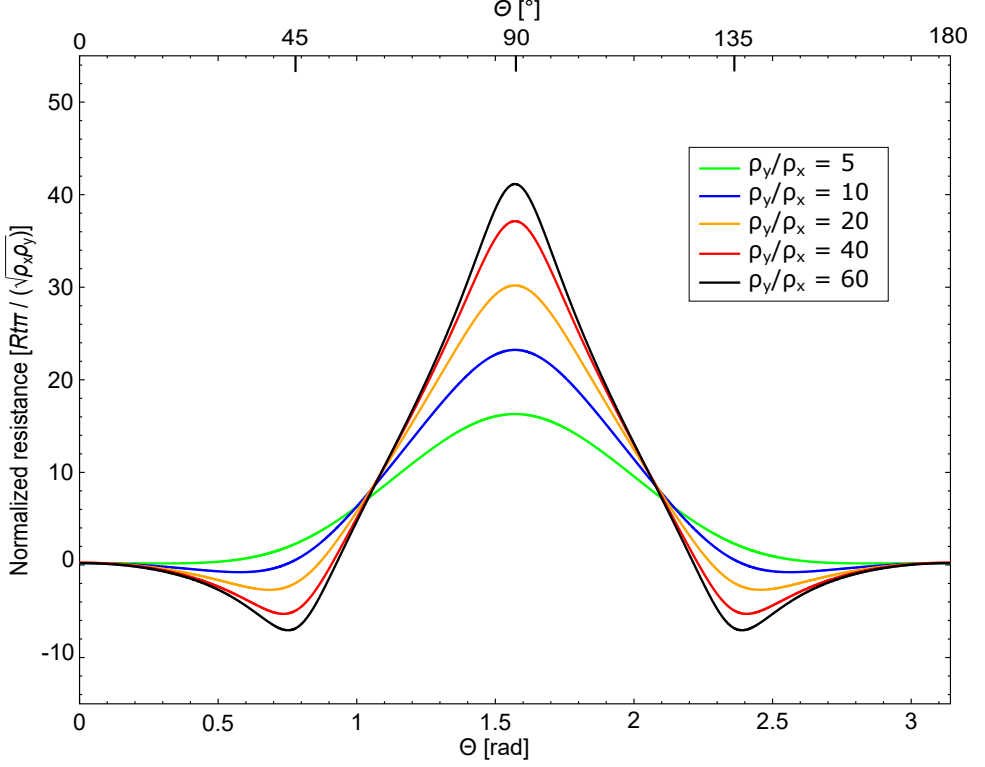


Figure 3.6.: Dependence of the normalized resistance on the angle of the probe array with respect to the main axes x and y of the resistivity tensor for different in-plane resistivity anisotropy ratios as indicated.

3.4. Measurement of out-of-plane as well as in-plane anisotropic transport behavior

In section 3.2 an easy way to measure the out-of-plane component of a sample was introduced, which however required the knowledge of the in-plane resistivity anisotropy, while in section 3.3 the well established theoretical basics for the measurement of both in-plane resistivity components were summarized. The combination of the two procedures enables the measurement of all three resistivity components $\rho_x \neq \rho_y \neq \rho_z$ of a single electrically homogeneous and oriented thin-film sample with thickness t . Starting with 4-probe transport measurements in square formation with $s \gg t$ (2D transport case) yields ρ_x and ρ_y . Then, the probe separation s is varied to observe the crossover point

between the 2D and 3D transport case, which yields the ratio ρ_z/ρ_x and hence the value ρ_z . The entire procedure can be performed in-situ without any treatment, thinning, cutting, rotation, or re-alignment of the sample.

3.5. Summary and conclusions

In this chapter the formalism describing the measurement of the independent components (ρ_x , ρ_y , and ρ_z) of anisotropic, but diagonal resistivity tensors was addressed. Diagonal resistivity tensors describe materials with cubic, tetragonal, hexagonal, trigonal, and orthorhombic symmetry. The van der Pauw transformation was used to map the anisotropic real situation onto a spatially distorted, but isotropic model. This procedure makes it possible to formulate the relations between the resistance measured in a 4-probe configuration and the components of the resistivity tensor for the 2D and 3D limiting cases as well as for the crossover regime. The latter is of particular importance, since I found that the observation of the 2D-3D crossover point allows for a direct determination of the in-plane to out-of-plane resistivity anisotropy ratio. I therefore propose to measure the crossover function of an oriented thin-film sample of a given thickness t with a 4-probe STM by varying the probe spacing s to determine the in-plane to out-of-plane resistivity anisotropy. For in-plane isotropic system ($\rho_x = \rho_y$), this method even allows the simultaneous and parameter-free measurement of ρ_x and ρ_z , since in this case the measured resistance in the 2D limit only depends on ρ_x . In order to treat the most general case $\rho_x \neq \rho_y \neq \rho_z$, I introduced the well established method for the measurement of ρ_x and ρ_y in the in-plane anisotropic case. This is achieved in the 2D regime, where the resistance is independent of ρ_z , by rotating the probe array with respect to the x and y -axes. This procedure is possible with both the square and in-line probe configurations (here I restricted myself for the sake of brevity to the square configuration) and can of course easily be carried out in a 4-probe STM at large probe separations ($s \gg t$). Finally, I described how the two methods, (i) variation of the probe spacings to address the out-of-plane anisotropy and (ii) in-plane rotation of the probe array to address the in-plane anisotropy, can be combined to measure with a 4-probe STM all three independent resistivity components ρ_x , ρ_y and ρ_z of a single oriented thin-film sample in a parameter-free manner. In contrast to previous methods, the proposed measurement protocol, which is based on the flexible probe positioning of the 4-probe STM, does neither require a specific device structure, nor a comparison of samples with different microstructure, or modelling of transport or effective medium properties. In particular, the protocol can be applied to materials that are not available as micrometer-thick crystals or are unstable unless stabilized in thin-film form.

The theoretical basics outlined in this chapter will be used in chapters 6 and 7 to design and interpret 4-probe electronic transport measurements of epitaxial films of the hexagonal $(\text{Cr}_{0.5}\text{Mn}_{0.5})_2\text{GaC}$ MAX phase and the orthorhombic $(\text{Cr}_{2/3}\text{Ho}_{1/3})_2\text{AlC}$ i-MAX phase.

4. Experimental setup

This chapter presents the used experimental setups, the 4-probe STM LT Nanoprobe from Scienta Omicron [23] as well as additional parts of the measurement system (the preparation chamber) and the probe preparation. The chapter begins with the introduction to the LT Nanoprobe followed by an explanation of scanning tunneling microscopy, a description of the top-mounted SEM that is used to monitor the probe positioning. Then the setup for transport measurements is introduced, and finally the preparation chamber and the probe preparation are described.

The never ending progress in modern science requires reliable tools for the characterization of physical and chemical properties of a wide range of materials. Furthermore, the process of miniaturization demands for additional progress of the investigation techniques. The STM is an experimental tool down to atomic resolution, where a probe scans over a surface, allowing surface mapping, spectroscopy as well as even manipulation of single atoms. Thus, it is a powerful tool for the microscopic and nanoscopic world. The ongoing progress to nanostructures as well as new material classes represented for example by the 2D materials or by investigations of single molecules leads to advanced instruments. The multi-probe STMs exhibit novel possibilities for investigations in the microscopic and nanoscopic world comprising in addition to the possibili-

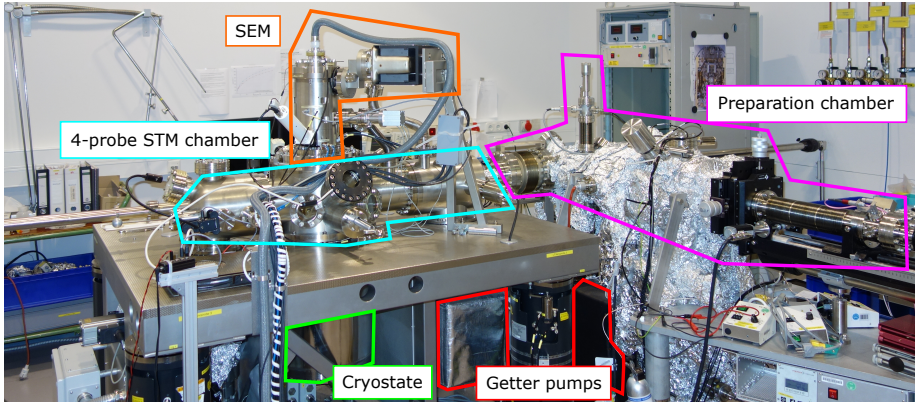


Figure 4.1.: Photograph of the entire measurement setup. The two chambers as well as the cryostat and the ion-getter pumps for the main and preparation chamber are marked.

4. Experimental setup

ties of single-probe STMs novel applications like scanning tunneling potentiometry or the characterization of electronic transport properties at the nanoscale via the 4-point method.

The 4-probe STM from Scienta Omicron called LT Nanoprobe was developed for these purposes and is used in this work. The experimental setup of the microscope is shown in figure 4.1. The 4-probe STM is inside the main chamber on the left side, and the SEM is mounted from the top. A cryostat is fixed from below allowing cooling the microscope with LN and LHe down to temperatures of about 77 K and 5 K, respectively. A preparation chamber is attached to the main chamber and is used for cleaning the STM probes as well as the samples. The whole setup is operated under UHV conditions preventing the investigated sample from air contamination. Therefore, the system is pumped by ion-getter pumps (one for the main and one for the preparation chamber) as well as titanium sublimation pumps (again one for the main and one for the preparation chamber). These pumps provide a pressure of (mostly less than) $5 \cdot 10^{-10}$ mbar. The main chamber is mounted on a table with air damping system to reduce external vibrations, while the preparation chamber stands directly on the floor.

4.1. LT Nanoprobe

A closer look at the main chamber is presented in figure 4.2 (a) and (b). (a) shows the main chamber, which houses in the center the 4-probe STM to be discussed later in

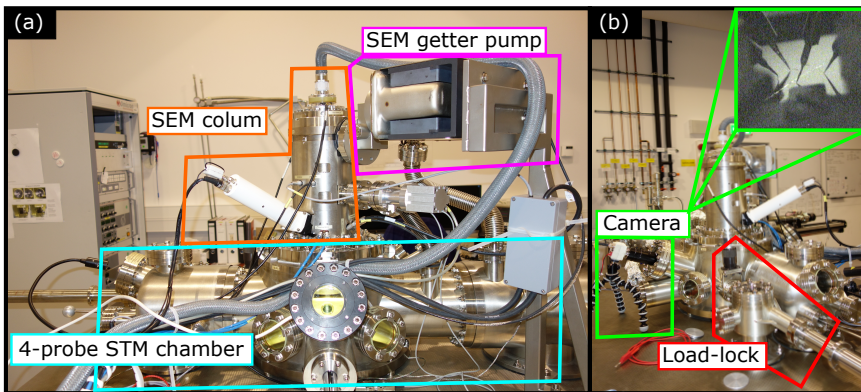


Figure 4.2.: The 4-probe STM setup. (a) shows the main chamber with the SEM column with attached photo-multiplier (white) and the SEM ion-getter pump. (b) is a view on the load-lock system and the camera for observing the coarse positioning of the probes as shown in the insert (the insert photograph is taken by F. Matthes).

more detail. The top-mounted SEM is a UHV Gemini column developed in collaboration between Scienta Omicron and Carl Zeiss AG. The top part, which houses the source filament, is separately pumped by the SEM ion-getter pump. Figure 4.2 (b) shows the load-lock system used for transferring ex-situ prepared samples and probes into the UHV system. It can be independently pumped via a turbo-molecular pump in combination with a rotary-vane prepump. The load-lock system can be sealed from the main chamber by a manually operated valve. During measurements all pumps of the load-lock system are switched off to reduce vibrations. The also shown camera is used for the observation and control of the coarse positioning of the STM probes. An example screenshot showing four probes is displayed in the insert of figure 4.2 (b).

4.1.1. 4-probe Scanning Tunneling Microscope

After the outer parts are briefly described, the 4-probe STM stage placed in the center of the main chamber is presented in the following. Around the 4-probe STM there is a carousel with 28 slots for storing probes and samples. As can be seen in figure 4.3 (a), the

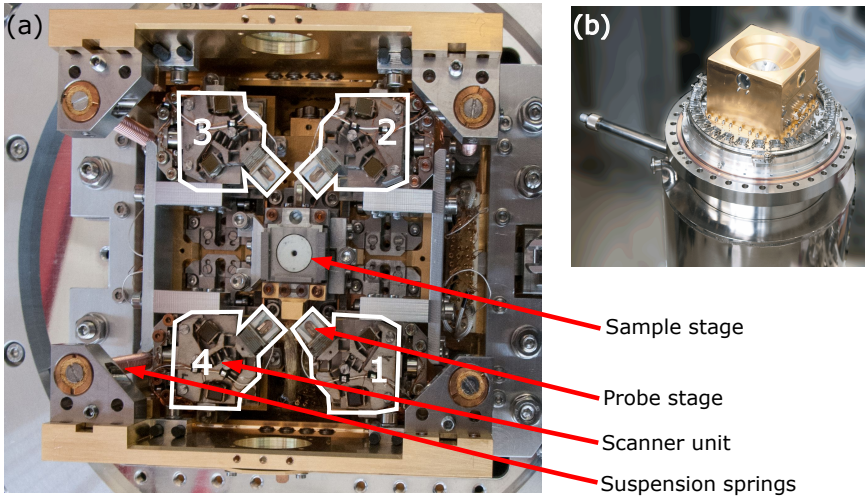


Figure 4.3.: Photograph of the 4-probe STM stage. (a) The four scanner units are arranged around the sample stage in the center. For reducing vibrations the stage hangs on four suspension springs located at the outer perimeter. (b) The stage is capsuled in the cooling shields ensuring measurements at 5 K (LHe) and 77 K (LN). The mounting flange has an outer diameter of 32 cm and the square golden structure an edge length of 15 cm. Photographs are taken by F. Matthes.

4. Experimental setup

central sample stage is surrounded by four scanner units (marked with the white lines), that accommodate the STM probes. Each of these units can be controlled separately. All scanners can be moved via piezo-motors within a coarse range of laterally $(5 \times 5) \text{ mm}^2$ and 3 mm in the z -direction. If a probe is in the tunneling regime (STM contact), the scan range is about $(20 \times 20) \mu\text{m}^2$ in xy -direction and $1.6 \mu\text{m}$ in z -direction. The sample stage can be moved laterally over a range of $(4 \times 4) \text{ mm}^2$. Normally, the whole stage is locked, i.e. it is not hanging on the suspension springs, but is pressed against the flange. For sensitive STM measurements the stage can be unlocked to the so-called hanging stage. In this position, the STM is suspended from springs in the recipient, so that the springs together with an eddy-current damping mechanically decouple the STM stage from the recipient and the environment, which obviously reduces external vibrations. Beneath the stage is a superconducting coil which is able to generate a magnetic field perpendicular to the sample of about 25 mT. For measurements at low temperature, the entire microscope stage is capsuled in two thermal shields, the outer with LN cooling and the inner with LHe cooling [see fig. 4.3 (b)]. A silicon diode reads out the current temperature.

The electronics for transport measurements is sketched in figure 4.4. The SEM has its own control unit and computer for SEM image display and acquisition. The sample stage is connected to ground with a switch. All four probes and all four scanner units

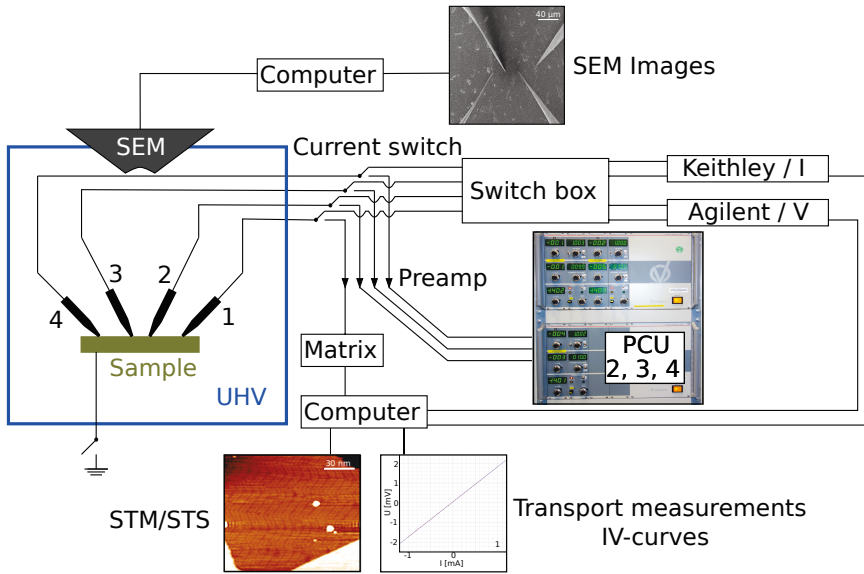


Figure 4.4.: Scheme of the electronics for transport measurements.

have their own control unit. Hence, it is possible to bring all four probes separately in STM contact with the sample. The scanner unit 1 is connected to the so-called Matrix, the standard microscopy hard- and software from Scienta Omicron to perform STM/STS measurements with a single scanner/probe unit. The other three scanners are controlled by Piezo Control Units (in the following PCU) which can be operated manually via the front panel or remotely via the Matrix. However, if one of the PCUs is connected to remote control, scanner 1 is disconnected from the Matrix and cannot be controlled anymore. For all four scanner/probe units the current signal passes a preamplifier before entering the PCU or Matrix.

A current switch is located immediately after the UHV feedthrough. It feeds the current signals either via the preamplifiers to the control units when operating in the tunneling regime or directly, i.e. without preamplification, to the so-called switch box for 2- or 4-probe transport measurements. This is to protect the preamplifiers, which operate in the tunneling regime down to the 0.1 pA range, whereas the transport measurements involve currents up to 30 mA. The switch box consists of a matrix of computer-controlled switches that allow to connect any probe (1...4) to any of the leads ($I^{+,-}$ and $V^{+,-}$) connected to the current supply (Keithley 2636A) and the voltmeter (Agilent 3458A). With this setup two probes can be chosen to inject a current and two other probes to measure the voltage drop. Sweeping the current from $+I$ to $-I$ and measuring the voltage drop a I - V curve is taken, where the resistance is the slope of the curve. The in-situ leads from the feedthrough to the probes each have a resistance of about $180\,\Omega$ [69]. This is a consequence of keeping the thermal conductivity of the wires and therefore the base temperature of the STM stage as low as possible. These relatively high parasitic lead resistances that add to the contact resistances R_C (see fig. 2.1) emphasize the importance of performing 4-probe measurements as discussed in section 2.1.

4.1.2. The piezo control

The control over the positions of the STM probes is separated in two devices. Stick-slip piezo-motors are used for the coarse movement. Coaxially arranged piezos move the scanner unit through a slow movement in the desired direction and then quickly retract. The scanner unit cannot follow this fast contraction due to its inertia and remains in its position. This cycle is repeated to move the driving axis step-by-step to the desired position, i.e. to bring a probe to a certain position of the sample. Fine movements of the probe along the x , y , and z -axes are performed by the piezo scanner which uses an applied voltage between $\pm 135\,\text{V}$ to extend or shorten the piezo crystal. This mode is used for approaching the probe to the tunneling regime and for STM imaging. The scan range is about $(20 \times 20)\,\mu\text{m}^2$ in xy -direction and about $1.6\,\mu\text{m}$ in z -direction. The absolute values in [nm] of this fine positioning is given by the calibrated hard- and software of the Matrix which is connected only to scanner 1.

For scanner 2, 3 and 4 the PCUs display just uncalibrated numbers as a control of a fine probe movement along the x , y and z -directions. Here, the fine movement is

controlled via potentiometers. In this thesis just the potentiometer of the z -axis is used for moving the probes several nanometers forward to bring them from the tunneling regime to direct contact. For a precise knowledge of the "contact depth" for transport measurements the z -elongation of the piezo has to be known in terms of [nm] instead of uncalibrated numbers. Therefore, the PCUs had to be calibrated as shown in appendix A.1. After this calibration, each probe can be first brought to tunneling contact using the STM approach procedure (see next section) and then be moved forward by few manometers in a controlled manner to establish direct (ohmic) contact for 2- and 4-probe transport measurements.

4.1.3. Scanning Tunneling Microscopy

The principle of a STM is to move a sharp probe close to a surface in order to measure the tunneling current between probe and sample [70]. As shown in figure 4.5 (a) a voltage is applied between probe and sample. Then the probe is approached until a current flow is detected (tunneling current) that typically occurs at distances of about $0.5 - 1$ nm. This approach procedure process uses the coarse as well as fine movement of the scanner in z -direction as can be seen in figure 4.5 (b). The probe is driven by the fine positioning to the sample (bright blue arrows). If the piezo is maximum elongated without measuring a tunneling current, it is quickly retracted and the coarse positioning is used to move the probe one step closer to the sample surface (blue arrows). These steps are repeated until a tunneling current is measured. Of course, the coarse step must be smaller than the total range of the fine motion.

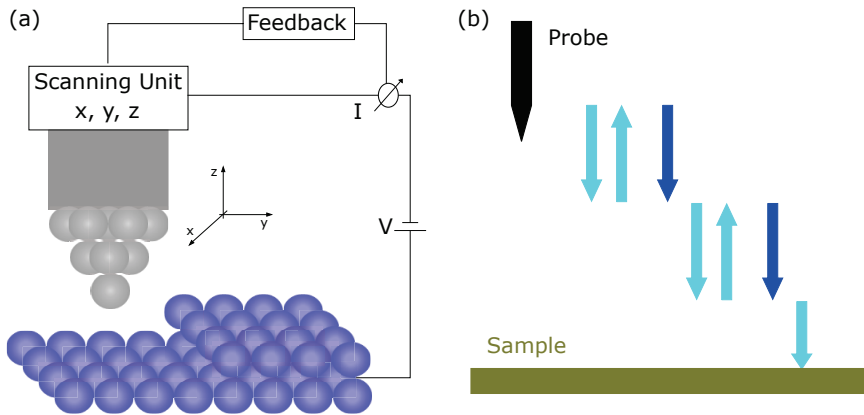


Figure 4.5.: (a) Scheme of a STM (adapted from [70]) and (b) sketch of the procedure to approach the STM probe into the tunneling regime at a probe-sample distance of $0.5 - 1$ nm (adapted from [69]).

After the probe is approached to the surface and scans along the y or x axes to map the surface topography, a feedback mechanism constantly adjusts the probe height by approaching or retracting the probe with the fine piezo to keep the tunneling current constant, which results in a constant probe-sample distance [70]. If the probe scans across an atomic step, the tunneling current will rise due to a smaller distance between probe and sample. The feedback circuit retracts the probe in order to keep a constant tunneling current. Recording the feedback signal as a function of the lateral probe position results in a map the probe height profile, which corresponds to the sample topography [70]. It has to be noted, that electronic effects can change this simplistic interpretation.

From the theoretical point of view the tunneling junction, meaning the sample-gap-probe system, can be treated in different approximations. Here, just a simple solution is presented for a one-dimensional approximation for one electron. This leads to the exponential dependency of the tunneling current on the probe-sample distance (the following explanation is largely based on Ref. [70]). An electron of energy E in a solid is described as a wave function $\psi(\mathbf{r})$ which is a periodic function for a free-electron approximation. The one-dimensional Schrödinger equation is solved by a non-normalized wave function

$$\psi(z) \propto e^{\pm ikz}, \text{ with } k = \sqrt{\frac{2m_e E}{\hbar^2}}. \quad (4.1)$$

The electrons in a solid with highest energy (E at the Fermi level E_F), which is called here $E = E_{\text{Particle}}$, have a lower energy than free electrons at the vacuum level. Approximately, this energy is the bonding energy of the electrons inside the solid. Thus, there is a barrier at the surface preventing electrons to leave the solid. To remove an electron from the solid a minimum energy is needed, which is the work function Φ . This is schematically sketched in figure 4.6 (a).

Classically, electrons cannot penetrate in the region, where $E = E_{\text{Particle}}$ is lower than the potential. However, in quantum mechanics electrons are able to penetrate into the classically forbidden region. Solving the Schrödinger equation yields an exponentially decaying wave function inside the region, $\psi(z) = \psi(0) e^{-\kappa z}$. A wave function that is decaying into the vacuum region is drawn in figure 4.6 (a). Note, that only the real part of the function is plotted. The probability of a particle being in the forbidden region is given by

$$|\psi(z)|^2 = |\psi(0)|^2 e^{-2\kappa z}, \text{ with } \kappa = \sqrt{\frac{2m_e \Phi}{\hbar^2}}. \quad (4.2)$$

A tunneling contact can be approximated by two conductive solids (probe and sample) separated by a vacuum barrier (or an insulating solid) of thickness d as shown in figure 4.6 (b). Also in the second solid the Schrödinger equation is solved by an oscillating wave function. Hence, in quantum mechanic there is a probability that the electron can be in both solids. Assuming a rectangular barrier with height $\Phi = E_{\text{vac}} - E_F$ and thickness

4. Experimental setup

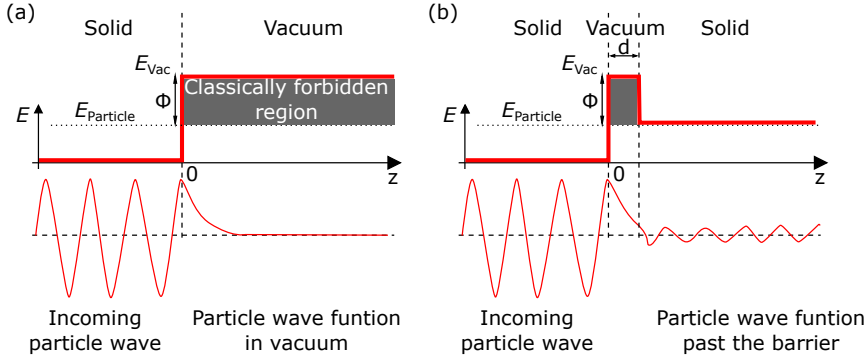


Figure 4.6.: (a) Potential diagram with a barrier of height Φ and the energy of an electron $E_{\text{particle}} = E_F$. The graph below shows the real part of the electron wave function with an exponential decay in the vacuum region. (b) Potential diagram for a solid-vacuum-solid configuration. The electron wave function oscillates in front of the barrier, exponentially decays inside the barrier, and again oscillates after the barrier, but with a significantly reduced amplitude. Redrawn from [70].

d , the transmission coefficient for the electron behind the barrier can be calculated and is given by

$$T = \frac{|\psi(d)|^2}{|\psi(0)|^2} \approx e^{-2\kappa z}. \quad (4.3)$$

The main characteristic of the transmission coefficient is an exponential decay with the barrier thickness d . The decay length is given by the square root of the work function. This means that the right solid probes the probability density of the electron states at distance d from the surface. It can also be derived that the tunneling current is proportional to the transmission coefficient, thus it depends exponentially on the distance between sample and probe. Assuming a typical work function $\Phi = 4 \text{ eV}$, equations (4.2) and (4.3) reveal that increasing (decreasing) the probe-sample distance by 1 \AA results in a 10-fold lower (larger) tunneling current. This strong dependency is the key to the high spatial resolution of the STM.

Two exemplary STM images are shown in figure 4.7 (a) and (b). Both images show a Au(111) surface for which atomic steps with a height 2.4 \AA as well as the so-called herringbone reconstruction are expected. However, the image in (a) is quite blurry which is related to the detrimental influence of external vibrations. The STM measurement is sensitive to mechanical vibrations due to the small distance between sample and probe. Therefore, in this thesis numerous vibration measurements were performed to identify

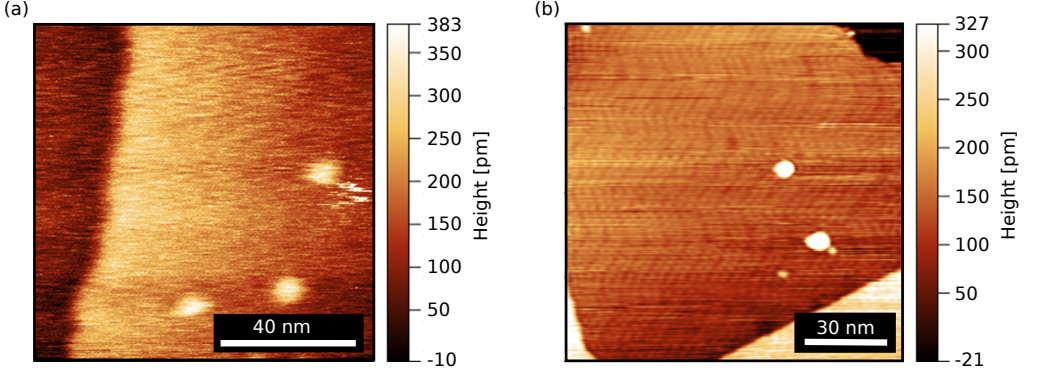


Figure 4.7.: STM images of a Au(111) surface (a) before reducing external vibrations showing a blurry step (tunneling current 1 nA, bias voltage 0.5 V, pressure $8.0 \cdot 10^{-11}$ mbar, temperature 300 K) and (b) after reducing external vibrations whereby the herringbone reconstruction and steps become visible (4.7 nA, -0.05 V, $2.0 \cdot 10^{-10}$ mbar, 300 K).

and suppress parasitic, external sources of vibrations. To this end, a vibration transducer was placed at different locations of LT Nanoprobe to measure vibration spectra [see fig. 4.8 (a)]. On the basis of these data various countermeasures were taken to reduce external vibrations. Just to mention a few: the air damping system of the LT Nanoprobe was newly adjusted, the wires connecting the UHV system to the control electronics

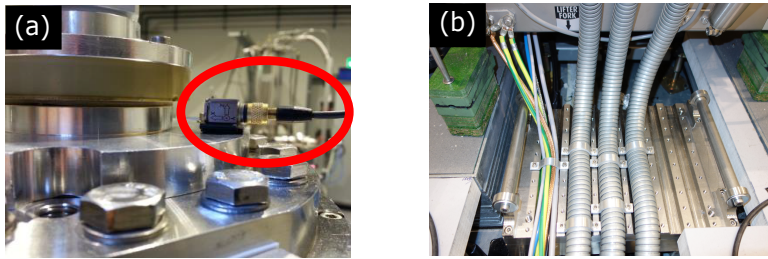


Figure 4.8.: Measurement of external vibrations. (a) The vibration transducer (marked by the red circle) is placed on top of the SEM column. (b) Heavy metal blocks are installed to mechanically stabilize the wires connecting the UHV system to the control electronics.

were fixed and mechanically stabilized on heavy metal blocks [see fig. 4.8 (b)], and the preparation chamber was placed on vulcanized rubber feet. The achieved improvement in the STM imaging stability is 4.7 (b), where clear atomic steps and even the herringbone reconstruction of the Au(111) surface with a much lower corrugation are visible.

4.1.4. Scanning Electron Microscope

For the observation and control of probe positioning as well as for imaging of the sample surface a SEM is mounted on top of the 4-probe STM stage. A SEM uses the interaction between an accelerated electron beam with the sample surface to image several properties like the sample surface. The principle setup of a SEM is shown in figure 4.9. The electron beam is generated in the upper part. A filament, for the Gemini column made of tungsten, acts as a cathode. The cathode is coated with zirconium oxide to lower the work function of the electrons from 4.5 to 2.7 eV [72]. The cathode is heated up to 1800K. Electrons are emitted due to the Schottky effect, where the work function of the electrons is reduced by applying a sufficiently strong electric field up to 7 kV

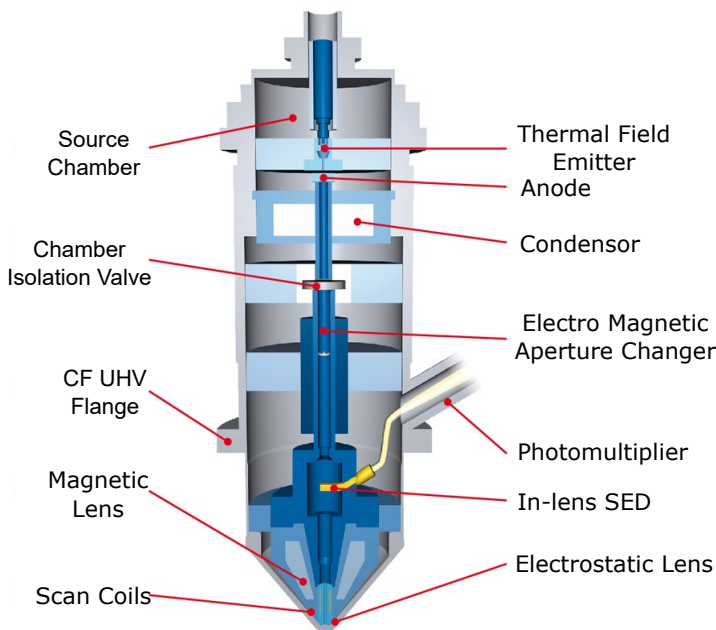


Figure 4.9.: Sketch of the SEM column. Taken from [71].

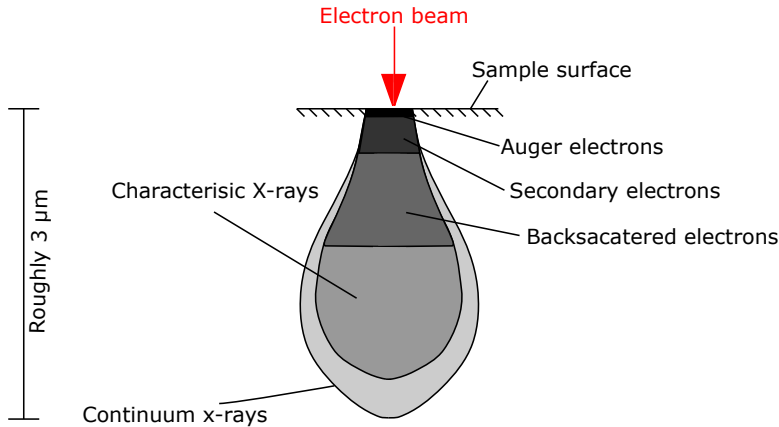


Figure 4.10.: Scheme of the interactions between the sample and the incoming electron beam. Adapted from [73].

yielding a large emission current. The emitted electrons form a beam which is then accelerated by acceleration voltages ranging from 1 to 30 kV. A lens system built up with electromagnetic coils provides the focus, zoom and scanning process (middle to lower part of the SEM column in fig. 4.9). The detector system (see below) is located in the lower part of the SEM column.

When the electron beam hits the sample surface several interactions are possible depending on the energy of the electron beam and the sample material. Typically an interaction volume as shown in figure 4.10 is created. Simply expressed, a higher energy of the electron beam leads to deeper penetration depth. Secondary and backscattered electrons are mostly used for the formation of SEM images. Backscattered electrons are the result of elastic scattering of the incoming electrons at energies in the [keV] range. The number of the backscattered electrons depends on the atomic number of the collision partner and thus contains information about the sample's composition. In contrast, secondary electrons scatter inelastically and consequently have lower energy typically in the [eV] range. Due to the low energies the secondary electrons are quite surface sensitive and exhibit an information depth of just few nanometers, since secondary electrons created in deeper regions of the sample do not reach the surface and thus are not detected.

The used Gemini column is equipped with an in-lens secondary electron detector (SED), i.e. a detector directly integrated in the interior of the SEM column. Due to the small information depth of the secondary electrons, this method allows a good imaging of the sample surface [73]. Thereby, the contrast of the image depends on the material. In general, high atomic number elements appear typically brighter than lighter elements.

4. Experimental setup

Insulating materials or metallic structures on insulating surfaces exposed to the electron beam are positively charged due the emission of secondary electrons and the lack of a connection to ground and thus a compensating current. The charging prevents further emission of secondary electrons. Therefore, insulating parts of the sample appear typically darker than conducting ones. Non-grounded samples show charging effects mostly appear as bright and dark spots in the image [73]. Since only the secondary electrons are detected in this work, further image formation mechanisms of the SEM are not discussed here.

4.1.5. Software for transport measurements

Using all possibilities of the LT Nanoprobe, probes are exactly positioned under SEM control and then brought into tunneling contact with the sample with the fine piezo drives and the tip approach procedure of the Matrix controller. For this procedure, the current switch shown in figure 4.4 feeds the current signal from the probes via the preamplifier to the Matrix and PCU controllers. In the next step of setting up a transport measurement, the current switch connects the probes with the switch box.

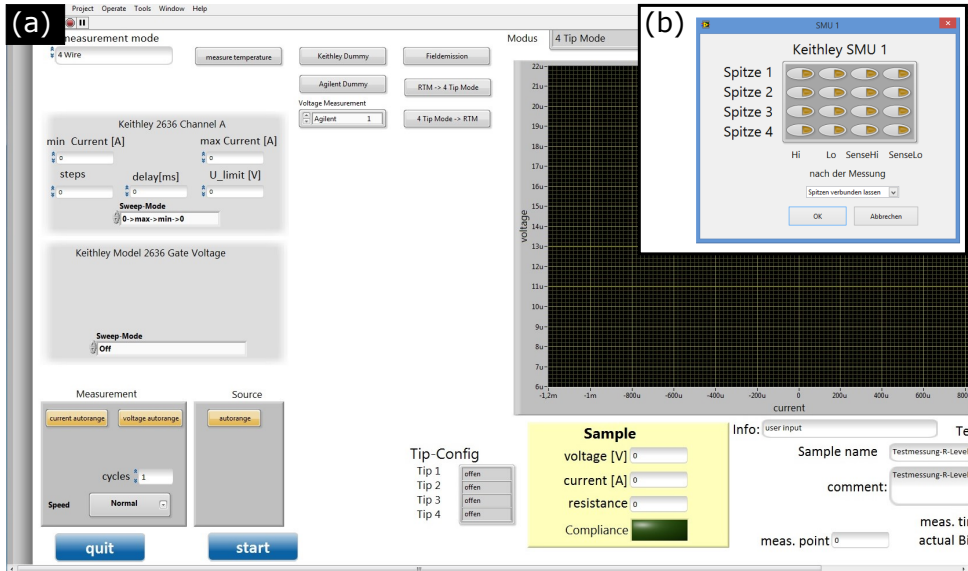


Figure 4.11.: (a) User interface of the software for the control and acquisition of transport measurements. (b) Connection matrix for the assignment of probes 1 to 4 to current ($I^{+,-}$) and voltage ($V^{+,-}$) leads.

This box is controlled via a software shown in figure 4.11 (a). Both hard- and software have been developed and realized by N. Schnitzler at the PGI-6 of the research center Jülich. With this software one can choose between 4-point, 2-point, and 2-point versus time transport measurements. For the 2-point measurements just the Keithley performs the measurements, meaning that it applies the current and measures the voltage at the same time. For the 4-point method the Keithley (current source) as well as the Agilent (voltmeter) are used. Additionally, the current and the measured ranges can be set by the user.

A further advantage of the switch box is the free assignment of probes 1 to 4 to the current ($I^{+,-}$) and voltage ($V^{+,-}$) leads. Before starting the measurement the software asks for a probe assignment that can be set using the matrix shown in figure 4.11 (b). Here, the channel Hi and Lo are the current channels I^+ and I^- as well as for the voltage HiS and LoS for V^+ and V^- . For the 2-point measurement only the channels Hi and Lo have to be selected. The chosen configuration is accomplished by an electronic circuit in the switch box. Note that due to isolation reasons, currents larger than ± 30 mA cannot be selected for the wires in the UHV system.

4.2. Probe preparation

For STM one needs well-defined and clean STM probes that are typically prepared via wet-etching. However, for the LT Nanoprobe the probes have to fulfill additional requirements. They should have a small contact radius in the lower nanometer range.

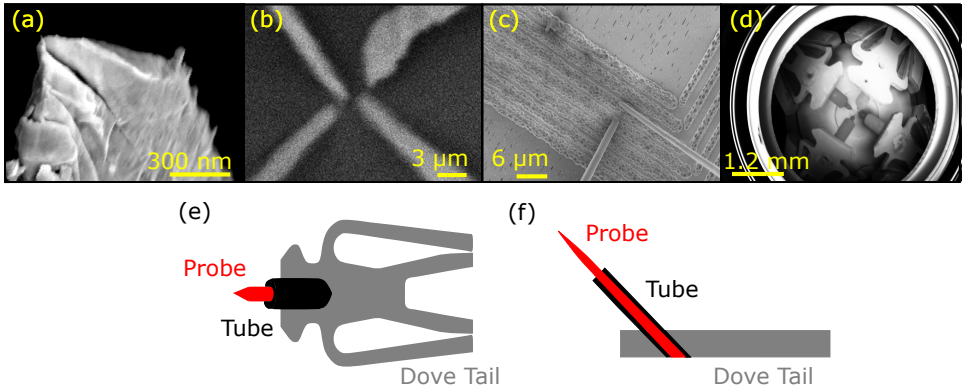
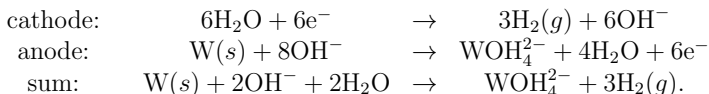


Figure 4.12.: Requirements for the used probes. (a) to (d) SEM images illustrate the special requirements concerning the microscopic and macroscopic geometry of the probes. In (e) and (f) the probe holder, the so-called dove tail, is shown in top and side view.

4. Experimental setup

In figure 4.12 (a) a wet etched probe is shown with a diameter of about 150 nm in the front part. The contact point on the probe has to be well defined so that the probes can be positioned close to each other as can be seen in figure 4.12 (b). On the other hand, the probes have also to be long enough to contact small structures without interfering with each other [see fig. 4.12 (c)]. A zoomed-out image [fish-eye mode of the SEM in fig. 4.12 (d)] shows a further reason to prepare long probes: The probe holders should also not interfere with each other. The probe holders are designed such that the probe axes are inclined with respect to the sample surface by an angle of about 45° [see fig. 4.12 (e) and (f)]. This angle is defined by a small tube that is fixed at the front end of the probe holders, which due to their specific shape are called "dove tails". After the etching process the probes are inserted into these tubes. All in all one needs long probes with small tip diameters. This is somewhat in contrast to normal STM probes that should be as short as possible to be less prone to vibrations.

The here used probes are self-made by wet-chemical etching of tungsten wires. The setup for the etching process is shown in figure 4.13 (a). A 0.38 mm thick tungsten wire is dipped into a 20 ml of 5 mol NaOH solution. Two ceramic tubes protect most of the wire and only expose a certain part of the wire to the etching solution. The etching process produces two tips, the upper one at the end of the wire and the lower one that drops down. In this thesis, the dropped piece of the wire is used as probe. The base plate of the bottom ceramic tube ensures that the dropped wire does not come in contact with any parts of the setup and thus protects the etched probe for any detrimental deformations. The counter-electrode for the etching process is a ring-shaped Pt wire. By applying a current between the tungsten wire (anode) and the counter-electrode (cathode) the following chemical reaction occur [74]



At the anode this reaction involves the oxidative dissolution of tungsten to soluble tungstate anions [75]. More exactly, firstly the tungsten oxidates to intermediate tungsten oxide and then by the non-electrochemical dissolution of the oxide a soluble tungstate anion is formed. At the cathode bubbles of gaseous hydrogen and OH^- ions are produced [75, 76]. These bubbles mostly appears around the etched area of the tungsten wire. To remove these bubbles from the wire and to maintain a homogeneous solution during the etching, a magnetic stirrer is used [see fig. 4.13 (a)]. This etching process typically yields apex diameters between 50 to 200 nm.

The etching setup also offers possibilities to change the shape of the probes. Firstly, the possibility to choose the width of the etched area by varying the distance between the two ceramic tubes allows to control the length of the probes. Figure 4.13 (b) shows two probes etched with a distance of about 2 mm between the ceramic tubes, while the third probe at the bottom is etched with a distance of about 5 mm. As expected, the third probe is clearly longer. The magnetic stirrer influences the shape of the probes as

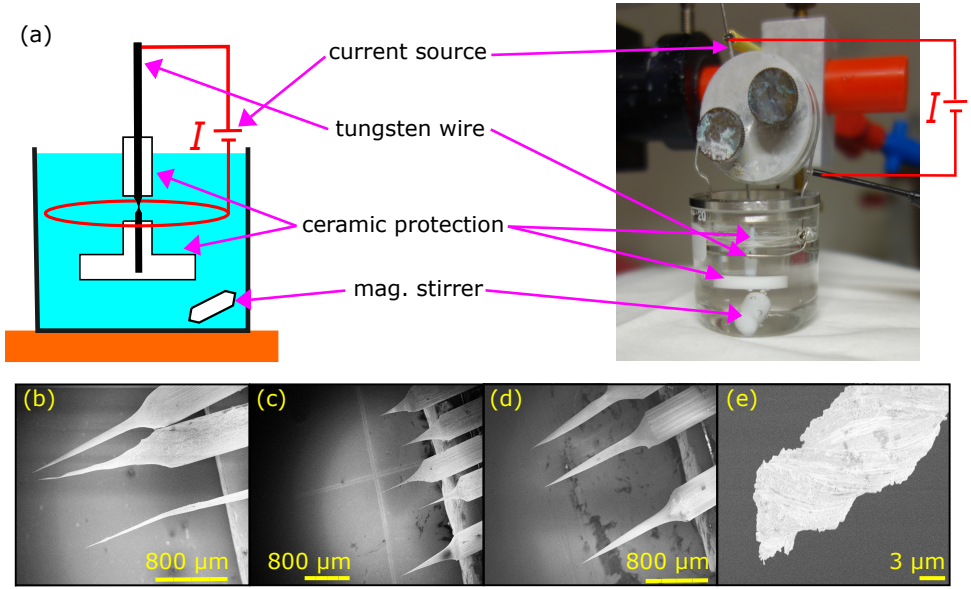


Figure 4.13.: (a) Sketch and picture of the setup for the wet-chemical etching of probes. (b) to (e) SEM images of examples of etched probes.

can be seen in figure 4.13 (c) and (d). In (c) the stirrer is switched on for all probes. Here, long cone-shape probes are produced, while etching without stirrer (see d) results in more elongated and less regularly shaped probes. It is reasonable to assume that the cone-shaped probes are less prone to vibrations than the elongated ones. Therefore, in this thesis the magnetic stirrer is always used during the etching process. However, the stirrer has to be switched off before the lower part of the tungsten wire falls down, otherwise one gets a twisted probe as shown in figure 4.13 (e). Finally, the last adjustable parameter is the etch current. Obviously, a high current leads to a fast etching and thus to shorter probes, while a lower current leads to a slow etching producing long thin probes. Both are not desired for the 4-probe STM setup, because short probes could interfere with each other and too long probes tend to be excited to mechanical vibrations. During this thesis it was found that reducing of the current from high to smaller values yields nicely cone-shaped probes. Typically, the etching current of 30 mA at the beginning is reduced after 2 min etching time to 22 mA, after further 4 min to 15 mA, and finally to 8 mA. After about 4 to 6 min at 8 mA the probe drops down. The immediate removal from the etch solution and cleaning in 80°C warm distilled water prevents post-etching processes that may degrade the apex diameter and the cone shape [77]. Nevertheless, before using

the probes they have to be further cleaned in the UHV system. This happens in the preparation chamber to be described in the next section.

4.3. Preparation chamber

The UHV preparation chamber is connected to the main chamber and is used for cleaning ex-situ prepared samples and STM probes. Figure 4.14 (a) shows the transfer system between the preparation chamber (left) and the main chamber (right). In contrast to the main chamber, the preparation chamber has no air damping system. To reduce external vibrations which can be transferred to the main chamber, there is a Vibration Decoupling Modul (VDM) between the main and preparation chamber. It consists of two concentric soft bellows. The inner bellow maintains UHV in the interior, whereas pressurized air between the two bellows compensates the vacuum force. This construction largely mechanically decouples the two chambers and also allows the main chamber to float on the air damping elements. Figure 4.14 (b) shows a different view to the preparation chamber featuring the tip-flash tool, a sputter gun, and manipulator, which includes a heating stage for samples. These three devices are explained in the following starting with the tip-flash tool.

- **Tip-flash tool**

The ex-situ prepared probes are still covered with oxides, including tungsten oxide, and other contaminations. A so-called tip-flash tool [see fig. 4.15 (a) and (b)], which is a rebuild version of Omicron's e-beam heater, is used to in-situ clean the probes. To do so, the dove tail [see fig. 4.12 (e) and (f)] with the mounted probe is inserted into a specialized sample holder in such a way that the probe points perpendicular to

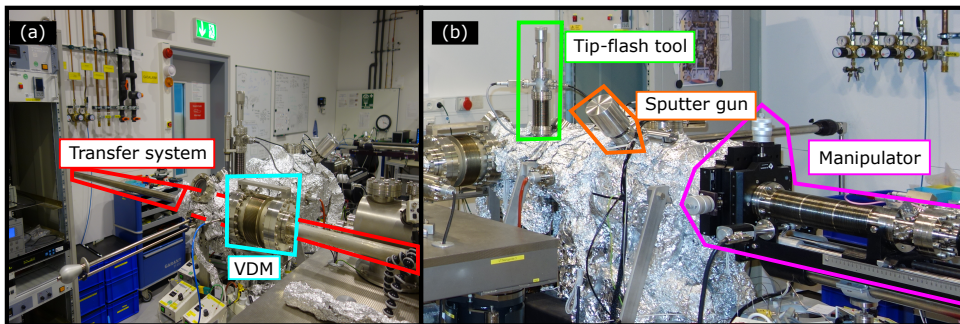
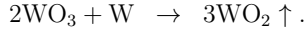


Figure 4.14.: Photographs of (a) transfer system between preparation and main chamber with the Vibration Decoupling Module (VDM) and (b) the preparation chamber.

the plate. This holder is introduced into the UHV and placed in the tip-flash tool. There, the probe can be driven with a z -shift manipulator downwards into a Wehnelt cylinder as can be seen in the picture of figure 4.15 (b). Inside this cylinder a thoriated tungsten filament acts as a electron emitter to heat the probe surface. The emitted electrons are typically accelerated onto the probe apex by a voltage of about 1.2 kV, while the filament current can be set between 0 A and 3 A, but is mostly set at 2.4 A. The measured emission current depends on the filament current, the acceleration voltage and the distance between probe and filament. Usually, the filament current as well as the acceleration voltage are fixed at the above mentioned values. Only the probe-to-filament distance is varied until an emission current of up to 15 mA is measured. The high-energy electron beam heats the probe and activates the following reaction [74]



WO_2 sublimates at 800°C , while pure tungsten melts at 3410°C . This suggests that there

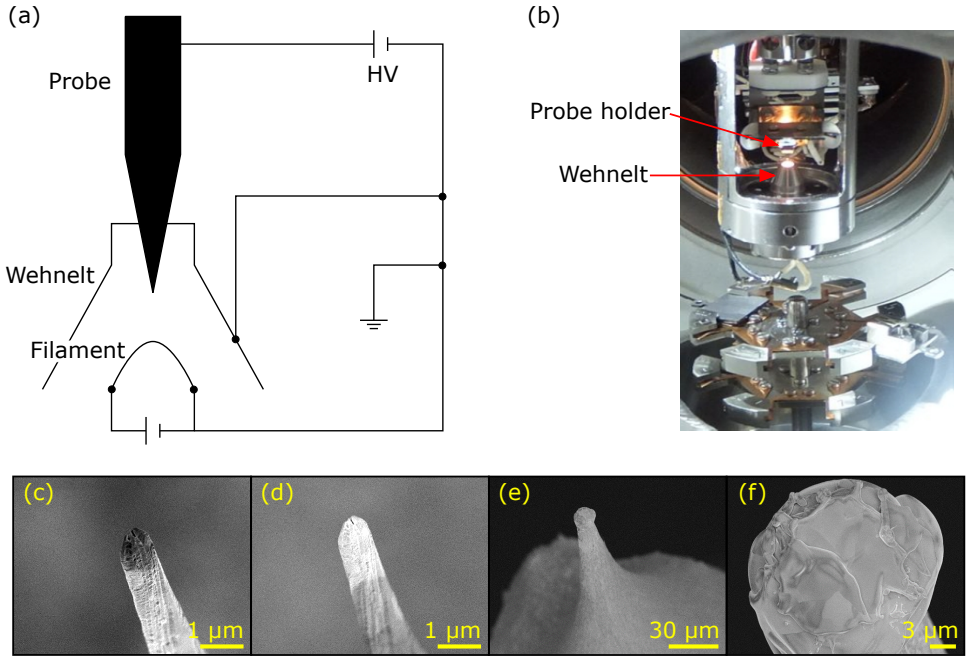


Figure 4.15.: (a) Sketch (adapted from [78]) and (b) photograph (taken from [79]) of the probe-flash tool. (c) to (f) SEM images of probes before and after applying the in-situ cleaning process with different parameters.

will be no blunting of the tip as the WO_2 sublimates [80]. However, elevated temperature also enhances the diffusion of surface atoms, which can lead to a blunting of the probe even below the melting point of tungsten [81]. Hence, the temperature should not raise much higher than 800°C and only for as short a period as possible. In the used setup, there is no possibility to measure the temperature at the probe. Therefore, the color of the probe is used as a rough indication of the temperature. It has been reported that for a heating temperature of about 600°C the probe starts to glow exhibiting a dark red color [82]. In a temperature range of about 900°C to 1100°C the probe shows an orange glow [83, 84] and for temperatures higher than 1100°C [83] the probe glows yellow. In the used setup an emission current of 15 mA leads to a bright yellow glowing. For the cleaning process the probe is typically first annealed for few seconds at an orange glowing occurring at an emission current of about 10 mA. Afterwards the probe-to-filament distance is increased to reach a lower heating temperature (emission current typically about 5 mA). At the lower temperature the probe is heated for several minutes. This heating process is based on Ref. [85].

Figure 4.15 (c) shows a probe after the wet-chemical etching process. The dark color of the probe originates from tungsten oxide which is non-conducting and thus has a dark contrast in SEM images. After flashing the probe in-situ, it appears bright as seen in figure 4.15 (d), indicating there are no oxides anymore. For longer heating times or higher emission currents, molten probes were observed as displayed in figure 4.15 (e) and (f). Therefore, one has to carefully chose the probe-to-filament distance to adjust the emission current. Nevertheless, it is advisable to check the probes by SEM imaging before using them as STM probes. Most importantly, all three steps – flash heating, SEM inspection, and mounting into the 4-probe STM stage – can be performed in the UHV system without breaking the vacuum.

• Sputter gun

Ex-situ prepared samples are contaminated and have to be cleaned in-situ, too. Surface adsorbed contaminations can be sputtered off by using accelerated noble gas ions. In principle, the ions hit the surface and take off the adsorbates. Therefore, a noble gas (in this thesis argon) is let into the UHV system via a fine leak valve which allows an exact flux control. The noble gas is ionized (in this thesis Ar^+) which enables the acceleration of the ions via an electric field to energies between 500 eV to 5 keV. The accelerated ion beam is directed to the sample.

There, three different mechanism lead to the sample cleaning as sketched in figure 4.16. In (a) the ion hits the adsorbate and knocks it directly from the surface. In (b) the ion is able to penetrate the surface before it is reflected. By the reflection process the ion can take off an adsorbate. Finally, in (c) the ion knocks off a substrate atom that can also remove a contamination [87]. All this leads to a stochastic process for the sputtering.

A sputter gun from Omicron, the ISE5 [23] is used, which operates at acceleration voltages between 500 V to 5 kV and achieves sample currents up to $80\text{ }\mu\text{A}$. However for

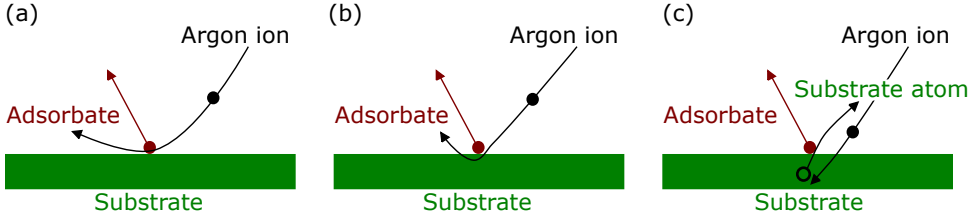


Figure 4.16.: Sketch of the three possible processes occurring during the sputtering process. Redrawn from [86].

the purposes in this thesis, sample currents of 5 to 10 μA are chosen, mostly at small acceleration voltages between 500 V to 1 kV. For these conditions, an argon partial pressure of about $1 \cdot 10^{-6}$ mbar is required. Since the sputtering process structurally impairs the sample and roughens the surface, thermal annealing is usually required after the sputtering.

- **Manipulator/Heating stage**

The sample manipulator has four degrees of freedom: x , y , z , and rotation about its axis. It is used to transfer samples to the sputtering position and to align it with respect to the ion beam. A heater is integrated in the manipulator head, which also allows simultaneous sputtering at elevated temperatures. The heating stage comprises a PBN/PG/PBN button heater. PBN stands for pyrolytic boron nitride and PG for pyrolytic graphite. The central PG layer is resistively heated by applying an electrical current and the outer PBN layers serve as electrical insulation. The heater used in this thesis can achieve sample temperatures up to 1000°C.

Heating a sample, which is typically called annealing, supports the recrystallization of the sample surface. Furthermore, it can triggered the segregation of impurities to the sample surface which leads to a re-contamination of the sample. In this case, annealing and sputtering should be repeated several times, especially for highly reactive materials.

4.4. Summary

In this chapter, I have introduced the employed instrumentation and experimental procedures. The principles of scanning tunneling microscopy were briefly introduced, mainly focusing on the procedure to approach the STM probes to the surface, which is of importance for establishing gentle and reproducible contacts for 2- and 4-probe transport measurements. The switching from the tunneling regime for the controlled approach of the probes to the (ohmic) contact regime for the transport measurements is achieved with the currents switches and the home-built software-controlled switch box. The latter was in this thesis for the first time tested and employed under real experimental

conditions. Therefore, I gave a detailed description of both the hard- and software. Further strong emphasis was finally put on the ex-situ and in-situ preparation as well as SEM characterization of the probes, since I identified during my work the probe shape, cleanness, and reproducibility to be the most critical aspects for successful transport measurements with a 4-probe STM setup.

5. Characterization of electronic transport measurements by using a 4-probe STM

In this chapter the experimental part of electronic transport measurements with a 4-probe STM is introduced. First, ex-situ and in-situ measurements of several test resistors are shown to verify the transport measurement setup and procedure (section 5.1). Then, the procedure for performing in-situ electronic transport measurements is introduced (section 5.2) and possible errors emerging during experiments are discussed (section 5.3). Finally, measurements performed on copper (section 5.4) and gold (section 5.5) thin-film samples are presented, which demonstrate the impact of probe contact quality and verify the equations derived in section 2.4 for arbitrary probe configurations.

5.1. Measurements of ex- and in-situ test resistors

Before using the LT Nanoprobe for in-situ transport measurements the ex-situ setup has to be verified, in particular the wiring and electronics connected to the feed-through into the UHV system from the air side (see to fig. 4.4). To this end, the in-situ part (blue box fig. 4.4) is mimicked by several test resistors ranging from $1\text{ m}\Omega$ to $10\text{ k}\Omega$. The current switch connects the lead from the test resistor to the switch box using the software described in section 4.1.5. Sweeping the current from $-I$ to $+I$ and back to $-I$ delivers the I - V -curve. Thereby, each measured I - V -point is the average of 10 repeated measurements. For a test resistor of $10\text{ k}\Omega$ the curve in figure 5.1 is measured. Note, that the errors of the measured values are too small to be visible in the plot. Additionally as shown in the insert of figure 5.1, the test resistor is switched in series with two $100\text{ }\Omega$ resistors demonstrating that contact resistances (here the $100\text{ }\Omega$ resistors) do not have an influence on a 4-point transport measurement.

A linear fit function $V(I) = R \cdot I + V_0$ is used to determine the resistance (slope of the curve) as well as the offset V_0 , which should be close to zero. For the $10\text{ k}\Omega$ test resistor the fit yields $R = (10003.93 \pm 0.02)\text{ }\Omega$ and a small offset of about $V_0 = (29 \pm 8)\text{ }\mu\text{V}$. If the current range is step-wise reduced from $\pm 1\text{ mA}$ to $\pm 10\text{ nA}$ (measurements are shown in figure A.4 of appendix A.2), the result is basically unchanged as shown in table 5.1. The offset is typically in the low μV range and thus much smaller than the voltage drop and is most likely related to an instrumental offset of the voltmeter. The resistance is always determined to be $10.003\text{ k}\Omega$ with an error bar that depends on the current range. During the course of the thesis this measurement has been repeated several times, always showing the same results. Therefore, it provides a clear indication for a functioning and precise measurement system. The same set of measurements are performed with a test

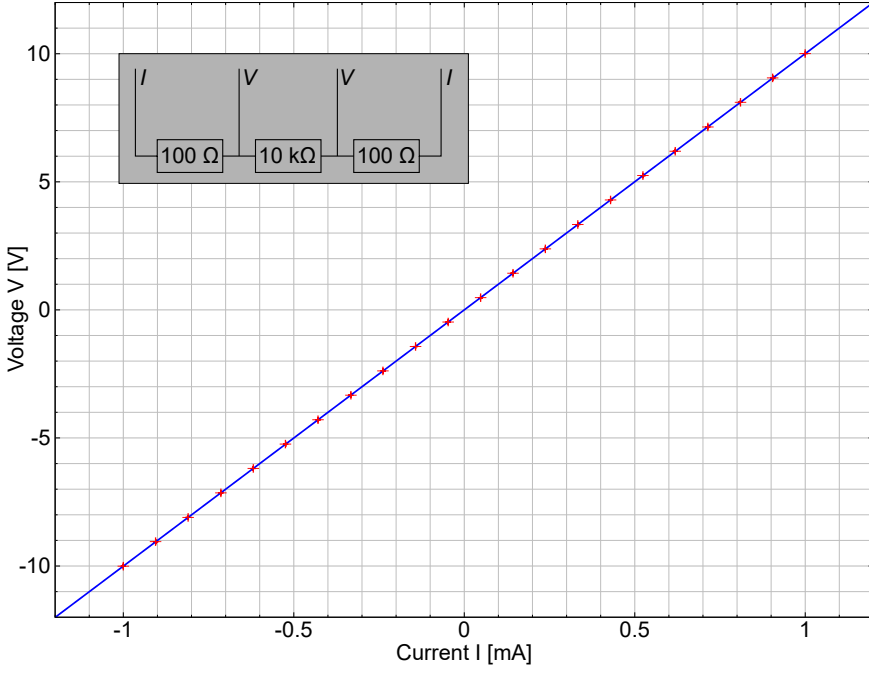


Figure 5.1.: I - V -curve for an ex-situ connected $10\text{ k}\Omega$ test resistor. Two $100\text{ }\Omega$ resistances connected in series as shown in the insert demonstrate that the contact resistances have no influence on the 4-point transport measurement. The linear fit function in blue yields
 $V(I) = (10003.93 \pm 0.02) \cdot I + (29 \pm 8)\text{ }\mu\text{V}$.

Current range	R	V_0
$-1\text{ mA to }+1\text{ mA}$	$(10003.93 \pm 0.02)\text{ }\Omega$	$(29 \pm 8)\text{ }\mu\text{V}$
$-100\text{ }\mu\text{A to }+100\text{ }\mu\text{A}$	$(10003.41 \pm 0.10)\text{ }\Omega$	$(25 \pm 3)\text{ }\mu\text{V}$
$-10\text{ }\mu\text{A to }+10\text{ }\mu\text{A}$	$(10003.65 \pm 0.04)\text{ }\Omega$	$(12.9 \pm 0.2)\text{ }\mu\text{V}$
$-1\text{ }\mu\text{A to }+1\text{ }\mu\text{A}$	$(10003.0 \pm 0.4)\text{ }\Omega$	$(13.9 \pm 0.2)\text{ }\mu\text{V}$
$-100\text{ nA to }+100\text{ nA}$	$(10003 \pm 2)\text{ }\Omega$	$(17.28 \pm 0.16)\text{ }\mu\text{V}$
$-10\text{ nA to }+10\text{ nA}$	$(10003 \pm 7)\text{ }\Omega$	$(18.496 \pm 0.04)\text{ }\mu\text{V}$

Table 5.1.: Fit results for the $10\text{ k}\Omega$ test resistor measured in different current ranges.

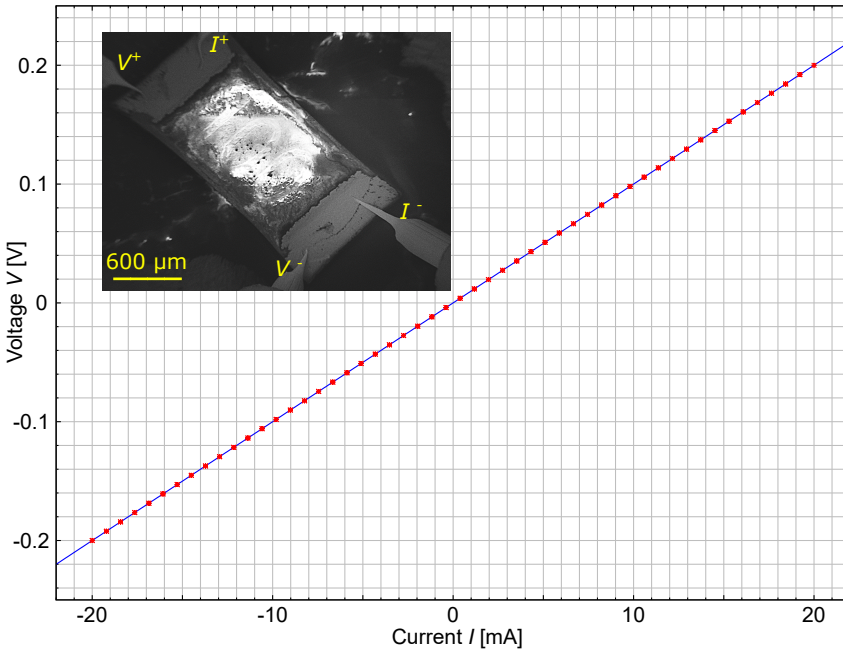
resistor of $1\text{ }\Omega$. The V - I curves are shown in figure A.5 of appendix A.2, and the results of the linear fits are compiled in table 5.2. The results are comparable to those of the $10\text{ k}\Omega$ test resistor. For the current range $-1\text{ }\mu\text{A to }+1\text{ }\mu\text{A}$ there are some deviations from

Current range	R	V_0
$-10 \text{ mA to } +10 \text{ mA}$	$(1.00005 \pm 0.00004) \Omega$	$(51.7 \pm 0.38) \mu\text{V}$
$-1 \text{ mA to } +1 \text{ mA}$	$(1.00023 \pm 0.00008) \Omega$	$(54.41 \pm 0.08) \mu\text{V}$
$-100 \mu\text{A to } +100 \mu\text{A}$	$(1.0002 \pm 0.0009) \Omega$	$(54.50 \pm 0.05) \mu\text{V}$
$-10 \mu\text{A to } +10 \mu\text{A}$	$(1.025 \pm 0.012) \Omega$	$(56.11 \pm 0.07) \mu\text{V}$
$-1 \mu\text{A to } +1 \mu\text{A}$	$(1.00 \pm 0.09) \Omega$	$(28.84 \pm 0.05) \mu\text{V}$

 Table 5.2.: Fit results for the 1Ω test resistor measured in different current ranges.

a the I - V -curve indicating the resolution limits of the setup. The voltage measurements are trustable in μV range but not below, while the current can be chosen down to 10 nA , but not below.

Two calibrated test resistors, $10.0015 \text{ m}\Omega$ and $1.0008 \text{ m}\Omega$, are used to verify the setup for small resistance values. Each resistor is ex-situ connected and measured four times. The corresponding plots are shown in figures A.6 and A.7 of appendix A.2. The mean resistance values are $(9.98 \pm 0.06) \text{ m}\Omega$ and $(1.006 \pm 0.015) \text{ m}\Omega$, respectively. In both


 Figure 5.2.: V - I curve for a 10Ω test resistor that is in-situ contacted with the four probes of the 4-probe STM (see SEM image in the insert).

cases the nominal value is within the error bars of $\pm 0.6\%$ and $\pm 1.2\%$, respectively. The voltage offset V_0 is in the μV range and is now in the range of the measured voltage drop. However, as can be seen from the results the offset does not interfere with the measurement, which solely relies on the slope of the V - I curves.

Finally, a $10\,\Omega$ test resistor is brought in the UHV system and in-situ contacted by four probes as one can see in the insert of figure 5.2. The measured I - V -curve delivers $R = (10.00060 \pm 0.00005)\,\Omega$ and $V_0 = (18.0 \pm 0.5)\,\mu\text{V}$. This result verifies the transport measurement setup including in-situ wiring and contacting. In conclusion, resistances can be determined with the transport measurement setup via the I - V curves with error bars way below 1%, except for resistance/current combinations resulting in voltage drops of a few μV or less. There is a small voltage offset in the μV range which however does not interfere with the determination of R .

5.2. Procedure of in-situ transport measurements

This section describes the procedure for performing of 4-point transport measurements with the LT Nanoprobe. First the camera is used to coarsely approach the probes to the sample surface. Then, the SEM is used to adjust the probes in the desired lateral configuration (e.g. in-line or square) as will be shown in several images in the following chapters. However, this procedure also limits the probe positioning below the μm range. The best SEM resolution is achieved with the STM stage in the locked position which ensures a short and rigid mechanical loop between SEM column and sample. On the other hand, the gentle approach of the STM probes to the sample surface, which is achieved by detecting the onset of a tunneling current, is best performed with the STM stage in the hanging position. In this position the stage is suspended from springs in the recipient and is decoupled from the environment. Weak mechanical oscillations of the stage with respect to the recipient and thus the SEM column are detrimental to SEM imaging and reduce the resolution, which also limits the smallest achievable probe spacing to about $1\,\mu\text{m}$ [61]. Figure 5.3 shows a SEM image of four probes at a lateral spacing $s \approx 2\,\mu\text{m}$. The wavy appearance is an image artifact due to slight oscillations of the STM stage relative to the SEM column in the hanging position. Hence, the probes can be positioned with separations ranging from the several $100\,\mu\text{m}$ -range down to about $1\,\mu\text{m}$.

Next, each probe is individually brought to tunneling contact (typically $1\,\text{nA}$ to $10\,\text{nA}$ tunneling current at $1\,\text{V}$ to $10\,\text{V}$ bias voltage) using the STM approach procedure described in section 4.1. Then, the feedback loop is switched off, and the probes are driven forward with the fine piezo, typically by about 1 to $2\,\text{nm}$ (or for the PCUs by about 1 to 2 uncalibrated units, see appendix A.1), which establishes an ohmic contact with the sample. This gentle procedure ensures that the contact diameters do not exceed $200\,\text{nm}$ [29]. The next step is to disconnect the probes with the current switch from the STM controller (Matrix or CPU) and to connect them via the switch box to the current

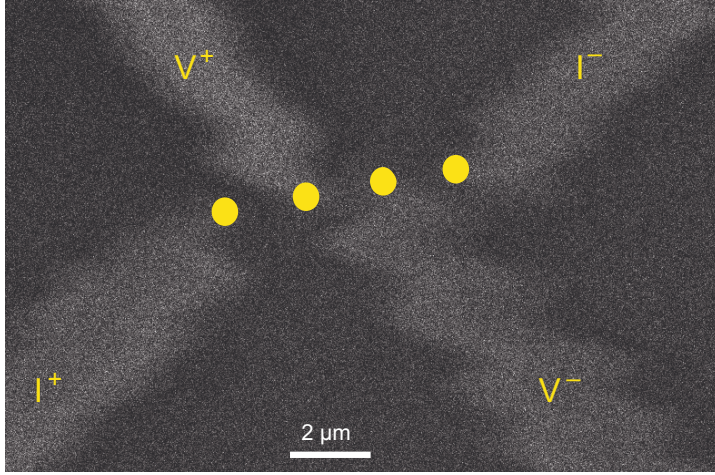


Figure 5.3.: SEM image of four STM probes in linear arrangement with a mutual lateral spacing of approximately $2\ \mu\text{m}$. The yellow dots mark the approximate contact points between probes and surface, and the labels indicate the probes used for current injection (I^- and I^+) and for the measurement of the voltage drop (V^- and V^+).

source and voltmeter (see fig. 4.4). The desired measurement mode (e.g. 2- or 4-probe mode) as well as the assignment of the probes to the current source and the voltmeter are selected in the software controlling the switch box. Now, the setup is ready for the measurement of resistances via V - I curves as discussed in the previous section.

5.3. Discussion of errors

In the course of this thesis, it turned out that resistance measurements carried out several times in succession on the same material using same parameters, but with repositioning of the probes, lead to a spread of the resistance values of about 10%. The previously shown results for test resistors and the error bars resulting from fits of individual resistance measurements show errors of 1% at most, but usually much smaller. Therefore, possible error emerging due to the probe diameter as well as to the probe positioning are discussed in the following. This discussion has been published in the supplementary material of Flatten et al. [61].

- **Probe contact diameter**

A major advantage of using a 4-probe STM to perform 4-point measurements is the possibility to realize much smaller and variable probe spacings than with conventional

setups. However, the expressions relating the measured resistance R to the resistivity ρ [e.g. equations (2.26) and (2.27) shown again below] have been derived in chapters 2 and 3 under the assumption that the probe spacings s are much larger than the probe contact diameter d , i.e. $s \gg d$. For STM probes brought into ohmic contact, we estimate $d < 200$ nm, and the smallest probe spacing considered in this work is $s = 1$ μm . Hence, $s/d \approx 5$ and the error due to the finite size of the contacts needs to be considered.

Ilse et al. [88] performed numerical simulations to determine geometrical correction factors for finite-size probes. They find that for large sample size ($> 10d$, which is clearly fulfilled in our case) and for $s/d > 5$ the error due to the finite probe contact radius is less than 5%. A similar result was obtained by Just et al. [29] in the framework of the N -layer conductance model. Probe contact diameters up to 200 nm at a similar probe spacing as in our case did not have a significant influence on the results of the calculations. Hence, we conclude that the errors due to the finite probe contact diameters do not exceed a few % and should not lead to a significant variance between measurements taken at different sample positions (but with the same nominal probe spacing s), since the probe approach procedure ensures the probe contact diameters to vary only in a limited range. Considering this, the contact diameter is neglected for the performed 4-probe transport measurements in this thesis.

• Precision of probe positioning

The advantage of 4-probe STM setups allowing for smaller and in particular variable probe spacings comes at the price of larger errors of probe positioning, compared to, for instance, lithographically fabricated multi-point probe arrays [11]. Positioning errors arise due to (i) unfavorable SEM imaging conditions caused by mechanical oscillations of the STM stage in the hanging position for smallest probe spacings (see fig. 5.3), (ii) reduced SEM resolution due to the large field of view (up to 100 μm wide, see fig. 5.8) required for large probe spacings, and (iii) uncertainties in identifying the exact point of contact, which is hidden by the body of the probe. Note for the latter point that the axes of the four probes are 45° inclined with respect to the surface (see fig. 4.12). We estimate that the positioning error in the whole range of probe spacings in our experiments amounts to 5–10% of the nominal probe spacing s .

In order to quantify the influence of the positioning error on the resistance (or resistivity) measurement, the vectorial notation relating the measured resistance R to the (isotropic) resistivity ρ for both the 3D [sample thickness $t \gg s$, equation (2.26)] and 2D [$t \ll s$, equation (2.27)] transport cases is considered

$$R^{3\text{D}} = \frac{\rho}{2\pi} \left[\frac{1}{|\vec{s}_2 - \vec{s}_1|} - \frac{1}{|\vec{s}_4 - \vec{s}_2|} - \frac{1}{|\vec{s}_3 - \vec{s}_1|} + \frac{1}{|\vec{s}_4 - \vec{s}_3|} \right]$$

$$R^{2\text{D}} = \frac{\rho}{2\pi t} \ln \left[\frac{|\vec{s}_3 - \vec{s}_1| \cdot |\vec{s}_4 - \vec{s}_2|}{|\vec{s}_2 - \vec{s}_1| \cdot |\vec{s}_4 - \vec{s}_3|} \right],$$

where \vec{s}_i denotes the position of probe i ($i = 1 \dots 4$). The current is injected through probes 1 and 4, and the voltage drop is measured between probes 2 and 3. For a linear

equidistant arrangement of the probes ($|\vec{s}_i - \vec{s}_{i-1}| \equiv s$ for $i = 2, 3, 4$), equations (2.26) and (2.27) reduce to equations (2.15) and (2.21) from section 2.2.

In the experimental procedure the first probe is placed at a random position \vec{s}_1 on the thin-film sample and the other three probes are positioned relative to \vec{s}_1 at nominal equidistant spacings \vec{s} , $2\vec{s}$, and $3\vec{s}$. This involves the errors described above and results in the effective probe positions

$$\vec{s}_1 \quad (5.1)$$

$$\vec{s}_2 = \vec{s}_1 + \vec{s} + \delta_2 \vec{s} \quad (5.2)$$

$$\vec{s}_3 = \vec{s}_1 + 2\vec{s} + \delta_3 \vec{s} \quad (5.3)$$

$$\vec{s}_4 = \vec{s}_1 + 3\vec{s} + \delta_4 \vec{s}, \quad (5.4)$$

where δ_i ($i = 2 \dots 4$) denote the relative positioning errors in the direction of \vec{s} . Of course, in practice there are also positioning errors perpendicular to the \vec{s} . However, they have only a second-order effect on the lengths $|\vec{s}_i - \vec{s}_k|$ ($i, k = 1, 2, 3, 4$) and lead to additional, but much smaller errors of the resistance measurement. The propagation of the relative errors δ_i ($i = 2 \dots 4$) in equations (2.26) and (2.27) for the measured

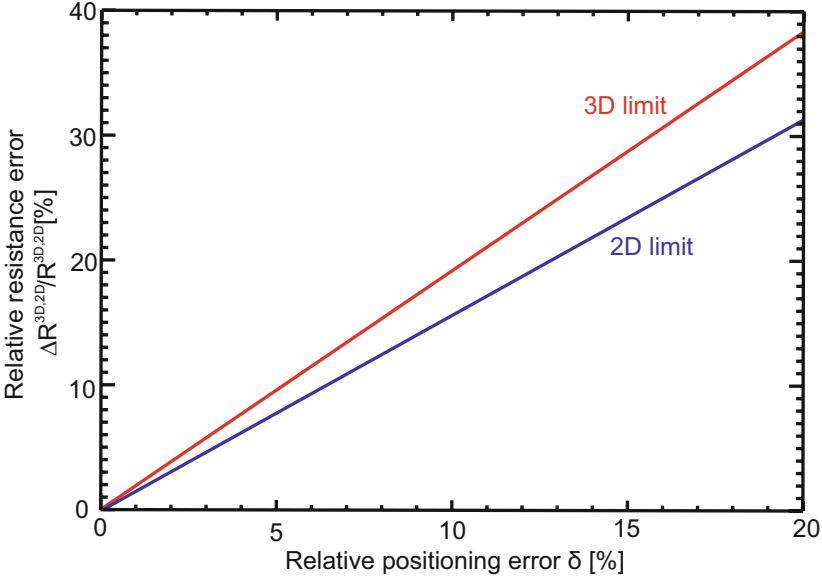


Figure 5.4.: Relative error of the measured resistance $\Delta R^{3D,2D}/R^{3D,2D}$ for the 3D (red) and 2D (blue) cases according to equations (2.26) and (2.27) as a function of the relative positioning errors, which are assumed to be equal for probes 2–4 ($\delta_2 = \delta_3 = \delta_4 \equiv \delta$).

resistances R^{3D} and R^{2D} is calculated and the result is plotted in figure 5.4. For both the 3D and 2D case the relative error of the resistance measurement is larger than the relative positioning error by a factor of about 1.6 and 1.2, respectively. The estimated positioning error of the experimental setup of 5–10% thus cause resistance variations of about 7–14%. Taking positioning errors in the direction perpendicular to \vec{s} into account slightly increases this error.

On the basis of this analysis, the positioning errors, in particular those along the connecting line between two probes, are the main source for the observed variance of the resistance measurements taken under identical conditions, but after repositioning the probes.

5.4. In-situ 4-probe measurement of a thin Cu stripe

In the chronological order of the experiments performed in this thesis, a thin Cu stripe served as a test sample for the first in-situ electronic transport measurement with the 4-probe setup. Copper was chosen due to its inertness and well-known low isotropic resistivity of $\rho = 0.01678 \mu\Omega\text{m}$ for a perfect crystal [89]. The results emphasize the importance of well-defined probe positioning and the as gentle as possible contacting of the sample. In these respects, these test measurements have provided important experimental hints for the improvement of the following measurements.

The stripe was prepared in a different UHV system by evaporating copper at room temperature through a shadow mask onto a MICA substrate. The growth rate was 0.1 \AA/s and the film thickness was $t = 30 \text{ nm}$. After transfer to the LT Nanoprobe UHV system through air, the Cu stripe was first annealed at a temperature of about 120°C

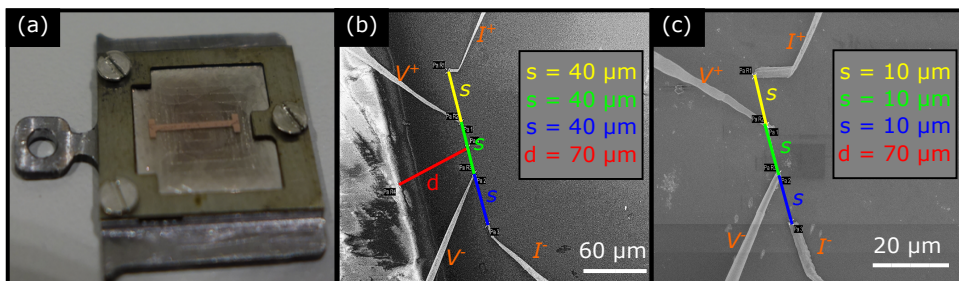


Figure 5.5.: (a) Photograph of the Cu stripe mounted on the sample holder. (b) shows a SEM image where the sample is contacted by four probes with an equidistant probe spacing of $s = 40 \text{ nm}$, while in (c) the probe spacing is reduced to $s = 10 \text{ nm}$. d measures the distance of the probes from the sample edge to ensure that edge effects can be neglected, which is the case for $d \gtrsim 2s$ [4].

for 2 h to remove eventually physisorbed surface contaminations. The 7 mm long and 600 μm wide stripe geometry is visible in figure 5.5 (a). Note that the Cu strip does not touch the metallic frame that fixes the insulating MICA substrate on the sample plate. Therefore, the stripe is not contacted to the ground potential. This complicates the contacting of the sample with the probes under SEM control because of charging effects and also prohibits the approach of the (first) probe via the STM controller.

5.4.1. Impact of positioning precision and contact radii

The contacting is realized according to the following procedure. The first probe is intentionally and vigorously driven into the sample using the coarse piezo motors, while observing the sample with SEM. The initial charging effects disappear as soon as the probe, which is ex-situ connected to ground, hits the sample. The disappearance of the charging effects is the signal to manually stop the coarse approach motion. This procedure inevitably degrades the probe apex and leads to an uncontrollably large contact radius. With the first probe defining the potential of the Cu stripe, the other probes can now be gently approached into the tunneling regime by monitoring the tunneling current. This is done after positioning the probes under SEM control in the desired probe configuration, here the Valdes in-line configuration as can be seen in figure 5.5 (b) and (c) for an equidistant probe spacing $s = 40$ and $10\ \mu\text{m}$, respectively. In contrast to the later performed measurements, the probes are moved several 100 nm forward with the coarse approach to definitely ensure the formation of ohmic contacts. I - V -curves are taken by sweeping the current from $-10\ \text{mA}$ to $+10\ \text{mA}$ and back to $-10\ \text{mA}$ and measuring the voltage drop ten times for each I value. An exemplary I - V -curve for $s = 40\ \mu\text{m}$ is shown in the insert of figure 5.6, which yields $R = (1.0027 \pm 0.014)\ \Omega$ and $V_0 = (28.5 \pm 1.1)\ \mu\text{V}$. Such measurements are performed for eleven spacings s between 100 and $s = 5\ \mu\text{m}$, where each measurement is repeated two times after retracting and new re-approaching of the probes. The mean values of the measured resistances are plotted versus the equidistant probe spacings in figure 5.6. According to the positioning errors discussed in section 5.3, each measured resistance comprises a 10% error bar. The rather crude contacting procedure with a forward motion of the z -piezo by about 100 nm into the sample leads to a significant deformation of the probes that can even be seen on the mesoscopic scale in figure 5.5 (b) and (c), where especially the outer current probes are strongly bent. This is taken into account by assigning an error to the s values. Note in this context, that a forward moving of the z -piezo by a distance $\Delta z \approx 100\ \text{nm}$ does not necessarily result in an indentation of the probe with the same depth. The angle of 45° between the probe axes and the surface normal [see fig. 4.12 (e) and (f)] allows the probes to accommodate most of the forward motion by elastic bending. Nevertheless, the forward motion is significantly reduced $\Delta z \approx 2\ \text{nm}$ on the basis of the data in figures 5.5 and figure 5.6.

For the Cu thickness $t = 30\ \text{nm}$ and large spacings in the μm -range one is clearly in a 2D transport regime ($t \ll s$). As described in section 2.2 for a 4-probe measurement with

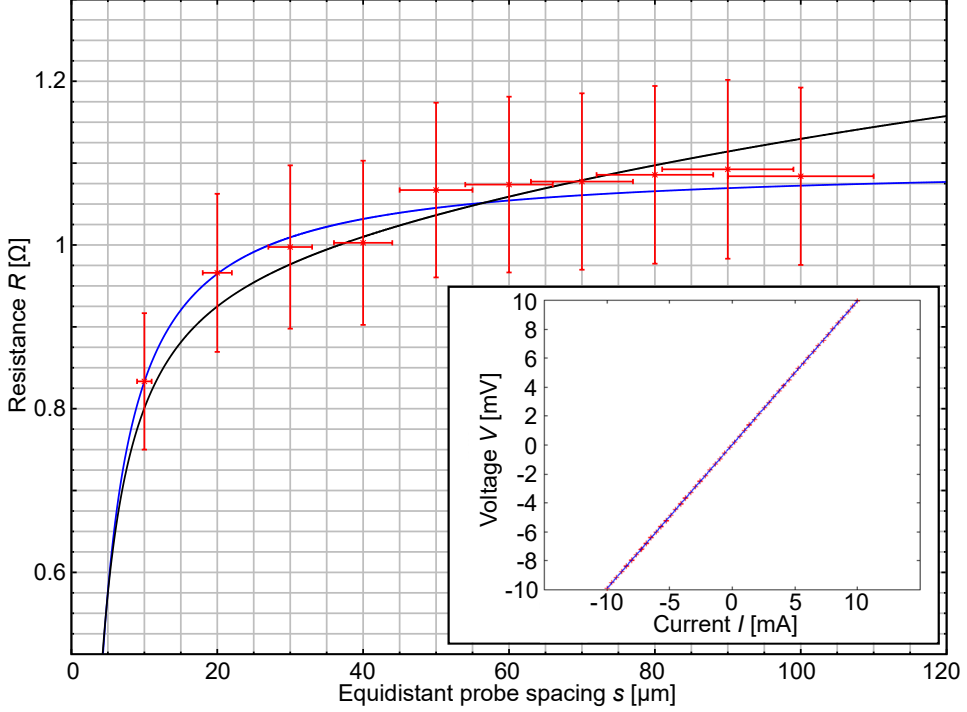


Figure 5.6.: Resistance R versus equidistant probe spacing s for the copper stripe sample. Solid lines are fit functions that neglect (blue line) or include (black line) edge effects, respectively. In the insert the V - I -curve for $s = 40 \mu\text{m}$ is plotted.

equidistant probe spacings, R only depends on the thickness t , but is independent of s . The measured R values in figure 5.6 are almost constant between $s = 50$ and $100 \mu\text{m}$, clearly indicating the 2D transport case. However, the resistance values strongly decrease for $s < 50 \mu\text{m}$. This can be explained by the influence of the contact radii, which in this measurement tend to be quite large due to the deep contacting of the probes with $\Delta z \approx 100 \text{ nm}$. Hence, the expression including the correction for finite tip radius (2.20)

$$R_{2\text{D}}^{\text{4P}} = \frac{\rho}{\pi t} \cdot \ln \left(\frac{2s - r_C}{s - r_C} \right)$$

discussed in section 2.2 is fitted to the data. The unknown variables are the resistivity ρ as well as the contact radius r_C . The fit (blue line in fig. 5.6) yields $\rho = (0.1495 \pm 0.0011) \mu\Omega\text{m}$ and $r_C = (1.15 \pm 0.04) \mu\text{m}$. This large contact radius is a further reason to use a much lower $\Delta z \approx 2 \text{ nm}$ in later transport experiments.

The red line d [see fig. 5.5(b)] measures the distance from the probes to the sample edge, which is $d = 70 \mu\text{m}$ for the measurements displayed in figure 5.6. Edge effects can be neglected if $d \gtrsim 2s$. Since this condition is not fulfilled for all measurements the fit equation is rewritten according to Refs. [4, 6]

$$R_{2\text{D}}^{4\text{P}} = \frac{\rho}{\pi t} \cdot \ln\left(\frac{2s - r_C}{s - r_C}\right) \cdot \left(1 + \frac{s}{2d + s} - \frac{s}{2d + 2s} - \frac{1}{2d + 4s} + \frac{1}{2d + 5s}\right),$$

where the right bracket is a correction factor that takes possible edge effects into account. The plot of the fit function is shown in figure 5.6 by the black solid line and yields $\rho = (0.1401 \pm 0.0015) \mu\Omega\text{m}$ and $r_C = (1.07 \pm 0.07) \mu\text{m}$. Both values deviate about 6% from the previously determined ones, thus edge effects can largely be neglected for these measurements.

In conclusion, large probe deformations leading to large contact radii as well as ill-defined probe positioning are detrimental the resistance measurements even in the large μm -range. Therefore, a precise probe positioning as well as a gentle sample contacting are key requirements for high-quality transport measurement. This is especially true for the characterization of the crossover between the 2D and the 3D transport cases, which typically occurs for small probe spacings. Hence, the contact radii should be negligibly small ($r_C \ll s$). Furthermore, the probes should be positioned at a distance $d \gtrsim 2s$ from the sample edge to avoid edge effects on the transport measurements.

5.4.2. Impact of thin-film quality

The resistivity measured for the Cu stripe deviates by a factor of 10 from the one expected for a perfect crystal $\rho = 0.01678 \mu\Omega\text{m}$ [89]. This can be explained by different electron scattering. For electron transport there are four mechanisms contributing to scattering in thin-film samples: surface scattering, grain boundary scattering, impurity scattering, and roughness [90]. The film resistivity ρ_{film} can be described via [91]

$$\rho_{\text{film}} = \rho_{\text{bulk}} + \rho_{\text{impurity}} + \rho_{\text{imperfection}} + \rho_{\text{thickness}}, \quad (5.5)$$

where is ρ_{bulk} the intrinsic bulk resistivity of a material, ρ_{impurity} describes the influence of impurities, $\rho_{\text{imperfection}}$ the influence of imperfections due to growth including grain boundaries, and $\rho_{\text{thickness}}$ the influence of the finite thickness. If the film thickness is in the range of the electron mean free path l in the material, there is a possibility of scattering effects at the bottom or the surface of the film [92]. The electrons have to scatter diffusely, i.e. inelastically, wherefore the resistivity increases above the intrinsic bulk value. In contrast to this, specular scattering has no influence on the conductivity, thus $\rho_{\text{thickness}} = 0$ for specular scattering [91]. A simple model for diffuse scattering is given by the expression derived by Fuchs [93] for $t < l$, where a pure and structurally perfect film is assumed

$$\frac{\rho_{\text{film}}}{\rho_{\text{bulk}}} = \frac{4}{3 \cdot (t/l) \cdot \log(l/t)}. \quad (5.6)$$

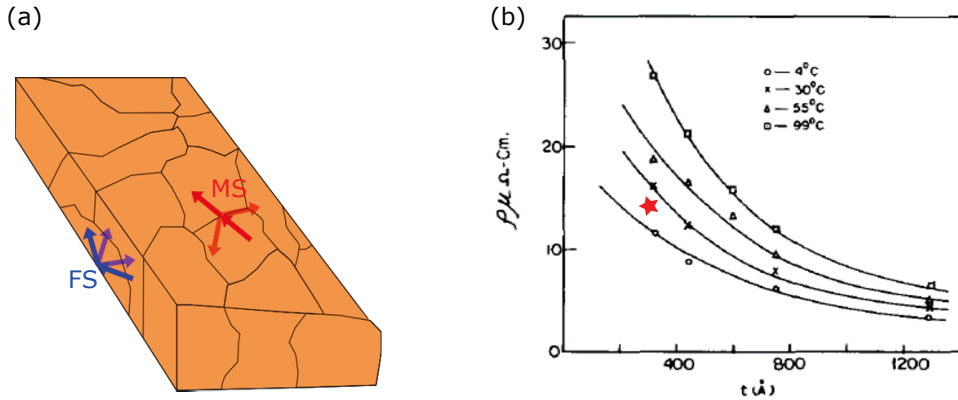


Figure 5.7.: (a) Sketch of a thin-film sample exhibiting surface or bottom scattering (blue arrows, FS model) and grain boundary scattering (red arrows, MS model) (adapted from [96]). (b) Increasing resistivity for decreasing sample thickness for Cu films on glass measured at 4, 30, 55, and 99°C (taken from [97]). The red star marks the here measured result for $t = 30 \text{ nm}$ measured at 21°C .

This model was extended by Sondheimer [94] and is today known as the Fuchs-Sondheimer (FS) model for surface scattering in conductors. FS scattering is sketched in figure 5.7 (a) with blue arrows. In addition, there is also the possibility of scattering at grain boundaries, which occurs if the grain size is comparable to the electron mean free path. This was found by Mayadav and Shatzkes [95]. The principle of the Mayadav-Shatzkes (MS) model is sketched in figure 5.7 (a) with red arrows. Granular growth often occurs for thin films. Depending on the substrate, growing rate, temperature as well as post annealing the grains have different sizes and thus influence the resistivity in a different manner. Finally, both surface and grain boundary scattering lead to an increased resistivity for thin-film samples.

The here determined resistivity $\rho = (0.1495 \pm 0.0011) \mu\Omega\text{m}$ clearly deviates from that of a Cu film ($t \approx 30 \text{ nm}$) on a Si(100) substrate grown at a rate of 2.56 nm/min , which amounts to $\rho \approx (0.028 \pm 0.0011) \mu\Omega\text{m}$ [98]. Evaporated, single-crystalline copper films on Si(111) grown with a rate of about 1 nm/min comprise a resistivity between 0.02 and $0.05 \mu\Omega\text{m}$ for $t \approx 30 \text{ nm}$ depending on preheating the substrate between 500 and 1200 K [99]. A sputtered copper films with $t \approx 30 \text{ nm}$ yields $\rho \approx 0.047 \mu\Omega\text{m}$ [100]. For all these measurements the growth rate is much slower than the one used here (0.1 \AA/s). The grain size is typically smaller for a faster growth [101], thus exhibiting stronger grain boundary scattering and higher resistivity. A result comparable to the present one is measured by Pal [97] for Cu films on glass, grown with a rate of 7 to 8 \AA/s and post-annealed at 120°C for 2 h . As far as MICA and glass are more or

less comparable substrate materials [101], the here measured resistivity is corroborated by the results in Ref. [97], where different film thicknesses are measured at different temperatures [see fig. 5.7 (b)]. The red star marks the measured resistivity of Cu stripe, which is measured at room temperature ($T \approx 21^\circ\text{C}$). It indeed lies between the curves measured at 4 and 30°C , respectively. Finally, for the electron mean free path in copper of $l \approx 39\text{ nm}$ [100], the intrinsic bulk resistivity $\rho_{\text{bulk}} = 0.01678\ \mu\Omega\text{m}$, and the thickness $t = 30\text{ nm}$, equation (5.6) delivers $\rho_{\text{film}} = 0.114\ \mu\Omega\text{m}$, which is smaller than the here measured $\rho = (0.1495 \pm 0.0011)\ \mu\Omega\text{m}$. Therefore, not only diffuse surface and interface scattering, but also grain boundary scattering has to be taken into account. Concluding, the thin-film quality has a significant impact on transport measurements and needs to be taken into account when discussing and comparing experimental resistivity values.

5.5. In-situ 4-probe measurement of a thin Au film – Test of arbitrary probe configurations

The final test sample is a 10 nm thick gold film grown at room temperature on Si(100) by evaporation at a rate of $1.1\ \text{\AA}/\text{s}$. The below presented results demonstrate again the influence of electron scattering at the surface and the bottom interface on the resistivity, but also confirm the crossover function derived in section 2.4 for arbitrary probe configurations. The latter is achieved by measuring the resistivity once in square configurations with variable edge lengths s and subsequently by keeping three probes fixed at the corners of a square configuration, while moving the fourth probe towards the center of the square.

After the transfer through air into the LT Nanoprobe UHV system, the gold film is annealed at 150°C for 1 hour. Then, the surface is imaged by the SEM [see fig. 5.8 (a)]. A pattern of dark lines is visible indicating that the film did not grow homogeneously and that surface and grain boundary scattering may play a role. The probes are positioned in

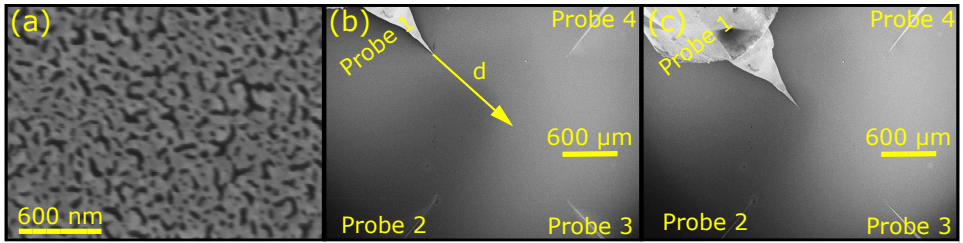


Figure 5.8.: (a) SEM image of the gold thin-film sample. (b) Square configuration of the 4 probes for $s = 1000\ \mu\text{m}$. (c) Probe 1 has been moved along the arrow d towards the center of the square.

a square configuration with edge lengths ranging from 50 to 1000 μm as shown in figure 5.8 (b). The probes are then brought into a gentle ohmic contact with the sample by moving them from the tunneling regime forward by $\Delta z = 1$ to 2 nm. The determination of the resistances is again performed by measuring I - V -curves. The square arrangement of the probes allows two independent measurements just by exchanging the assignment of two probes from current injection to voltage measurement. This change is sketched in the insert of figure 5.9, where I^- and V^+ are exchanged. The red arrows indicate the main directions of the injected current. For each square configuration (s and probe assignment), several measurements are performed at different locations on the sample, and the mean value of R for each measured s is plotted in figure 5.9. The error bars are mostly less than 10% with the largest being less than 15%. Obviously, R is independent of s , as expected since s is in the μm -range, while $t = 10$ nm. This clearly corresponds to the 2D transport case that is described by equation (2.29)

$$R_{2\text{D}}^{\text{square}} = \rho \frac{\ln(2)}{2\pi t},$$

which is plotted in figure 5.9 as a blue line. In contrast to the previous section, the contact radius of the probes can be neglected. This is because of the large probe spacings and the gentle contacting of the sample, which ensures a contact diameter of typically less than 200 nm [29]. The fit yields $\rho = (0.0906 \pm 0.0006) \mu\Omega\text{m}$, which is by a factor of about 4 larger than the ideal bulk value for gold $\rho_{\text{bulk}} = 0.02255 \mu\Omega\text{m}$ [89]. Again, this can be related to additional scattering. With the bulk resistivity ρ_{bulk} , the thickness $t = 10$ nm, and the electron mean free path of gold $l = 38$ nm [102], equation (5.6) yields $\rho_{\text{film}} = 0.093 \mu\Omega\text{m}$, which is close to the measured resistivity. This means that the enhanced thin-film resistivity is predominantly caused by additional surface/interface scattering. Negligibly weak scattering at grain boundaries is compatible with microstructure visible in figure 5.8 (a), since the length scale of the dark/bright contrast, which possibly represents the grain structure, is much larger than the electron mean free path of gold $l = 38$ nm.

The next measurement addresses arbitrary, i.e. non-regular, probe configurations. Starting from a square configuration with edge length $s = 1000 \mu\text{m}$, one probe is moved step-wise towards the center of the square [see to fig. 5.8 (b) and (c)]. d indicates the distance of the moving probe from the starting position in the corner of the square. Resistance values R measured at different distances d are plotted versus d in figure 5.10. For determining the resistivity via the crossover function for arbitrary probe configurations [equation (2.35)] derived in section 2.4, the probe separations s_i must be expressed by the edge length s and d (see insert of fig. 5.10),

$$s_1 = \sqrt{s^2 + d^2 - 2sd \cos(\alpha)} \quad (\text{from } V^+ \text{ to } I^+) \quad (5.7)$$

$$s_2 = \sqrt{2}s \quad (\text{from } V^+ \text{ to } I^-) \quad (5.8)$$

$$s_3 = \sqrt{2s^2 + d^2 - 2sd [\sin(\alpha) + \cos(\alpha)]} \quad (\text{from } V^- \text{ to } I^+) \quad (5.9)$$

$$s_4 = s \quad (\text{from } V^- \text{ to } I^-). \quad (5.10)$$

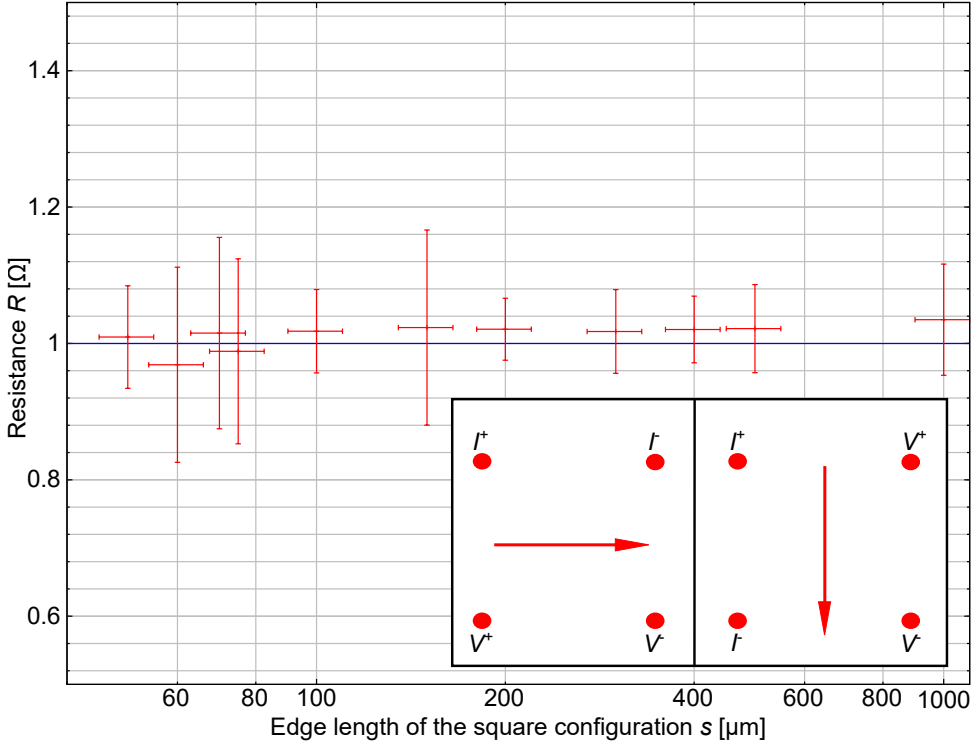


Figure 5.9.: Resistance R versus edge length s of the square probe configuration. The blue line is a fit to equation (2.29). The insert shows two different probe assignments that enable two independent measurements of R without physically moving the probes.

Note that these equations hold for both configurations sketched in the insert of fig. 5.10, if the angle α is defined for the two cases as indicated. For the measurements in figure 5.10, the I^+ probe is moved along the diagonal of the square configuration, thus $\alpha = 45^\circ$ yielding $s_1 = \sqrt{s^2 + d^2 - \sqrt{2}sd}$ and $s_3 = \sqrt{2}s - d$. The crossover equation (2.35) then becomes

$$R = \frac{\rho}{2\pi t} \cdot \ln \left(\frac{\sinh \left(\frac{t}{\sqrt{s^2 + d^2 - \sqrt{2}sd}} \right) \sinh \left(\frac{t}{s} \right)}{\sinh \left(\frac{t}{\sqrt{2}s} \right) \sinh \left(\frac{t}{\sqrt{2}s - d} \right)} \right). \quad (5.11)$$

Fitting of equation (5.11) to the data in figure 5.10 with $s = 1000 \mu\text{m}$ and $t = 10 \text{ nm}$ yields $\rho = (0.09543 \pm 0.00014) \mu\Omega\text{m}$, which is in good agreement (within 5%) with the

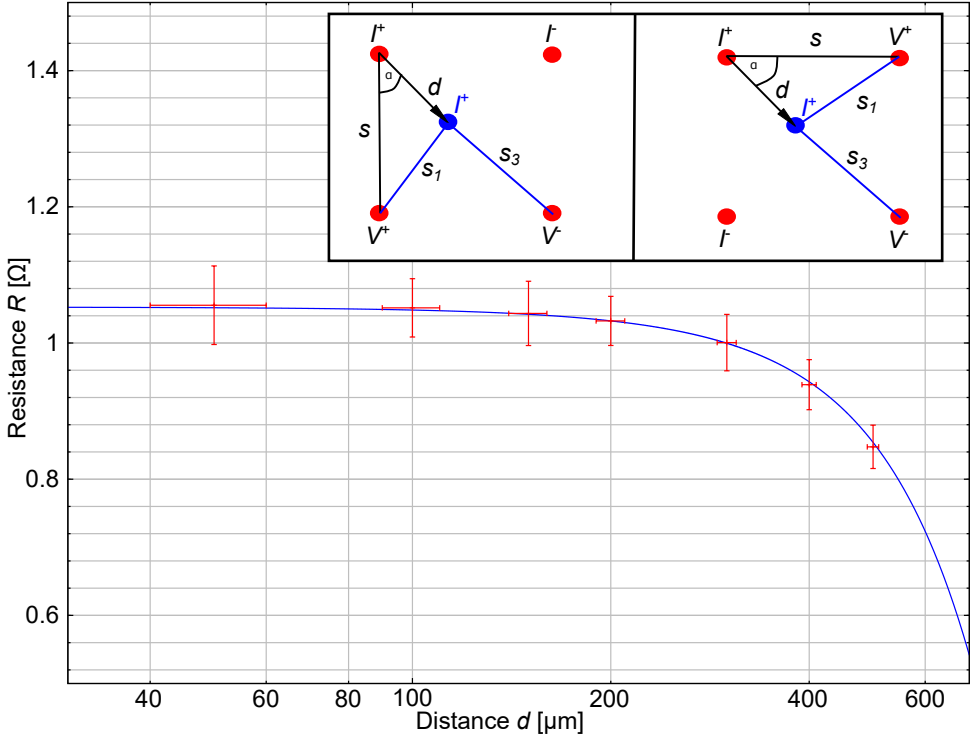


Figure 5.10.: Resistance R versus distance d of probe I^+ from the corner of the initial square configuration. The blue line is a fit to equation (5.11). The insert shows the probe configurations for exchanged V^+ and I^- probes. Note the different definitions of α .

resistivity determined from the data in figure 5.9. Hence, this measurement confirms the validity of the crossover function for arbitrary probe configurations, though here only demonstrated for the 2D transport case.

5.6. Summary and conclusions

In this chapter, I have presented experiments with ex-situ and in-situ contacted test resistors to check and verify the electronic setup, the wiring inside and outside the vacuum system as well as the data acquisition software. I also described the procedure for contacting a sample with the four probes and discussed the measurement errors due to finite probe radii and due to the limited accuracy of the probe positioning. The latter leads for our setup to a variance of consecutively measured resistance values of

the order of 10%, if the probes are retracted and re-positioned for each measurement. Further test measurements of the resistivity of in-situ contacted thin Cu and Au films yield good agreement with literature values, if additional scattering at the surface and bottom of the film and to a lesser extent at grain boundaries is taken into account. The main conclusions derived from these test experiments for this thesis concern the utmost importance of carefully forming the contacts between probes and sample. Only very gentle contacts realized by approaching the probes by $\Delta z \approx 1$ to 2 nm from the tunneling regime towards the sample enable negligibly small radii of the probe apexes and negligible (elastic and plastic) bending of the probes and thus reliable identification of the exact contact points. Additionally, to avoid edge effects on the transport measurement the probes should be placed at a distance $d \gtrsim 2s$ from the sample edge. Finally, I also tested and verified the crossover function that I have derived in section 2.4 for arbitrary probe configurations.

6. Electronic transport properties of a magnetic MAX phase – $(\text{Mn}_{0.5}\text{Cr}_{0.5})_2\text{GaC}$

MAX phases with the general formula $\text{M}_{n+1}\text{AX}_n$ with $n = 1, 2, 3$ (M is an early transition metal, A is a A-group element mostly of the main groups 13-16, and X is C or N) belong to the layered material class comprising a complex bonding scheme combining both metal as well as ceramic properties. This bonding scheme is the basis of numerous applications ranging from electrical contacts, magnetic sensors, spintronics devices to coating materials in aerospace technology [40–42], but also indicates anisotropic electronic transport properties, where the out-of-plane resistivity component is typically larger than the in-plane one [41]. In this chapter the magnetic MAX phase $(\text{Cr}_{0.5}\text{Mn}_{0.5})_2\text{GaC}$ is investigated, which has attracted interest due to its peculiar spin structure and resulting magnetic properties that both originate from the nanolaminated crystal structure [103, 104]. However, for further possible applications the conductivity properties of this MAX phase should be well known, thus the electrical transport properties are characterized in this chapter, especially regarding to the expected anisotropic electronic transport properties.

First, in section 6.1 the complex bonding structure of MAX phases is discussed which is an indicator for the anisotropic electronic transport properties. Section 6.2 introduces the two used thin-film samples and the measurement procedure for the MAX phase samples is shown. The results are discussed in section 6.3. First, the results for a 40 nm thin sample are presented to measure the in-plane resistivity component ρ_{ab} (section 6.3.1). Here, the previously derived equation for arbitrary probe configurations is employed. Section 6.3.2 presents the main result of this thesis for the $(\text{Cr}_{0.5}\text{Mn}_{0.5})_2\text{GaC}$ MAX phase, namely the determination of the in-plane and out-of-plane resistivity components ρ_{ab} and ρ_c of a 155 nm thick thin-film sample. The measurement protocol derived in chapter 3 yields a large anisotropy ratio of $\rho_c/\rho_{ab} = 529 \pm 49$. This is the first experimental application of this novel method and has been published in Flatten et al. [61].

6.1. Theoretical Background

The layered MAX phases comprise a complex bonding structure. The two-dimensional building blocks of $\text{M}_{n+1}\text{AX}_n$ phases are evident in the crystal structure for $n = 1$ shown in figure 6.1(a). M_2X layers formed by face-sharing M_6X octahedrons and planar A layers are stacked alternately along the c -axis. As a consequence, MAX phases exhibit chemical bonding anisotropy [40]. All bonds are predominantly of covalent character with different degrees of admixed metallicity or ionicity [40]. The mixed bonding character

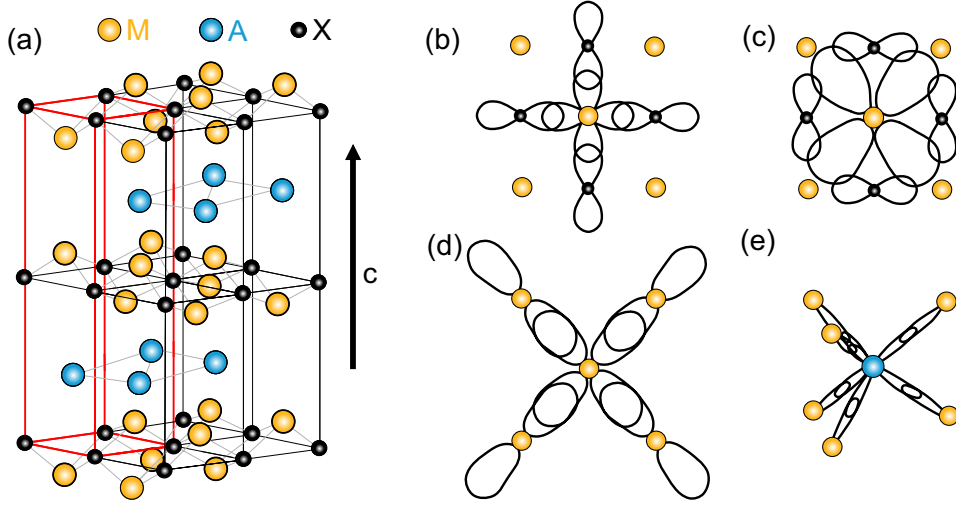


Figure 6.1.: (a) Layered crystal structure of M_2AX phases. The red lines indicate the unit cell. Bonds in the M_2X layer: (b) Covalent $\text{M-X } pd_\sigma$ bonds, (c) covalent $\text{M-X } pd_\pi$ bonds, and (d) mixed covalent-metallic $\text{M-M } dd_\sigma$ bonds. (e) Covalent $\text{M-A } pd_\sigma$ bonds between M_2X and A layers. (b) to (e) are adapted from [40]. Figure is taken from Flatten et al. [61].

gives rise to the combined metallic and ceramic properties of MAX phases.

Strong hybridization between the d -orbitals of the M elements and the $2p$ -orbitals of the X elements leads to M-X-M chains with strong covalent pd_σ and pd_π bonds as schematically shown in figure 6.1 (b) and (c), respectively. The primarily covalent M-A bonds between the M_2X and A planes sketched in figure 6.1 (e) are typically weaker than the M-X bonds. The d -orbitals of the M elements also form metal-metal dd_σ bonds with adjacent M atoms [see fig. 6.1 (d)]. The energy of these states, which are spatially confined in the M_2X layers, is in vicinity of the Fermi level E_F . These states dominate the overall density of states at E_F and accordingly also the electric conductivity, which is thereby much higher in the ab plane compared to the c -direction [40]. This is corroborated by density-functional theory (DFT) calculations of band structures of various MAX phases. Most MAX phases do not have bands that cross the Fermi surface along the c -axis [41]. Therefore, the anisotropy in the electronic structure is theoretically predicted to lead to anisotropic electronic transport. The anisotropy of the transport may be further enhanced by electron-phonon interaction [60]. Typically, the resistivity in the ab -plane $\rho_{ab} \equiv \rho_a = \rho_b$ is significantly lower than the resistivity along the c -axis ρ_c [40, 41, 55, 105], where ρ_{ab} and ρ_c are the two independent components of the diagonal

second-ranked resistivity tensor of MAX phases with hexagonal crystal structure, such as $(\text{Cr}_{0.5}\text{Mn}_{0.5})_2\text{GaC}$. In literature, however, the resistivity components ρ_{ab} and ρ_c are not often characterized experimentally because it is difficult to determine the out-of-plane resistivity component for thin-film samples. Therefore, in this thesis the anisotropic conductivity is investigated for the magnetic MAX phase $(\text{Cr}_{0.5}\text{Mn}_{0.5})_2\text{GaC}$ by using the crossover function to directly determine ρ_{ab} and ρ_c as described in section 6.3.2.

6.2. Experimental procedure

The used $(\text{Cr}_{0.5}\text{Mn}_{0.5})_2\text{GaC}$ thin-film samples with thicknesses $t = 40$ and 155 nm were grown at Linköping University by magnetron sputter epitaxy on a $\text{MgO}(111)$ substrate [103]. X-ray diffraction (in the following XRD) and transmission electron microscopy have proven the hexagonal M_2AX phase structure on $\text{MgO}(111)$ with $[11\bar{2}0]_{\text{MAX}} || [10\bar{1}]_{\text{MgO}}$ in the surface plane and $[0001]_{\text{MAX}} || [111]_{\text{MgO}}$ out of the plane, i.e. the a and b -axes are lying in the thin-film plane and the c -axis along the surface normal. Regarding the notation used in chapter 3 one can identify $\rho_{ab} \equiv \rho_a = \rho_x = \rho_b = \rho_y$ as the in-plane resistivity and $\rho_c \equiv \rho_z$ as the out-of-plane resistivity. Thus the crossover function derived in section 3.2 can be used for the direct determination of the in-plane as well as out-of-plane resistivity components.

The 4-probe electronic transport measurements are performed at room temperature with ex-situ wet-chemically etched and in-situ flash-annealed tungsten probes (see section 4.2). Before the transport measurements each probe is inspected in the SEM to ensure a probe diameter of less than 200 nm. After transfer into UHV, the 40 nm sample was annealed for 1 h at 200°C and the 155 nm sample for 1 h at 150°C to desorb physisorbed contaminants from the chemically inert surface. For each resistance measurement, the four STM probes are first positioned under SEM control in the desired configuration, namely in-line with irregular probe spacings for the 40 nm sample (see section 6.3.1) and in-line with equidistant probe spacing s for the 155 nm sample (see section 6.3.2). Each probe is then approached into the tunneling regime (typically 1 nA tunneling current at 1 V bias voltage) using the approach procedure of the STM controller. Finally, the probes are individually moved (using the z -axes of the STM piezo scanners) by $\Delta z = 1 - 2$ nm towards the sample to establish ohmic contacts. This gentle procedure ensures that the contact diameters do not exceed 200 nm, and therefore they have no significant influence on the measurement (see section 5.3). As described previously in chapters 4 and 5 for the resistance measurements, the probes are disconnected from the STM controller and connected to a current source and a voltmeter. The current I is injected through the outer probes (I^+ and I^-), and the voltage drop V is measured between the inner probes (V^+ and V^-). The current is swept from -10.0 to $+10.0$ mA for the 40 nm sample and from -1.0 to $+1.0$ mA for the 155 nm sample to record a V - I -curve, from which one obtains the resistance R by fitting the linear function $V(I) = R \cdot I + V_0$. V_0 is always of the order of 40 to 60 μV and thus much smaller than the voltage drop.

The error bar of the resistance values is typically within 0.1%. The measured resistances are finally plotted versus the adjusted probe spacing.

6.3. Electronic transport measurements

First the results for the 40 nm sample are presented to determine the in-plane resistivity component ρ_{ab} from measurements performed in the 2D transport regime. Afterwards, the 155 nm sample is used to directly and simultaneously determine both the in-plane and out-of-plane resistivity components ρ_{ab} and ρ_c as well as the anisotropic ratio ρ_c/ρ_{ab} via the 3D-2D crossover function.

6.3.1. Determining the in-plane resistivity component measured on a 40 nm thin-film sample

For the purpose to determine the in-plane resistivity component ρ_{ab} of the magnetic MAX phase $(\text{Cr}_{0.5}\text{Mn}_{0.5})_2\text{GaC}$, the probes are first placed in an in-line configuration

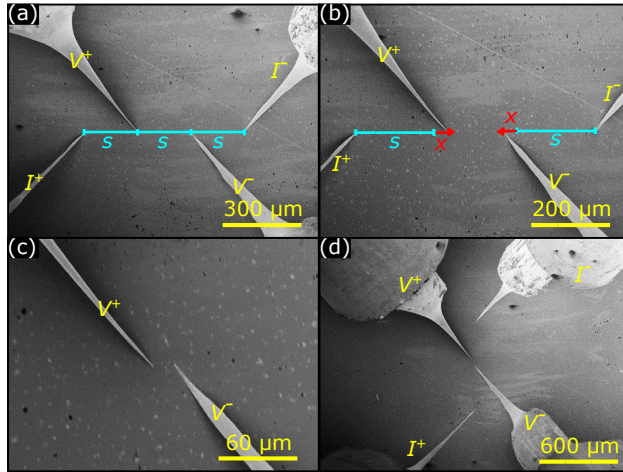


Figure 6.2.: 4-probe transport measurements of a 40 nm thick $(\text{Cr}_{0.5}\text{Mn}_{0.5})_2\text{GaC}$ film. SEM image (a) of an in-line configuration with equidistant probe spacing $s = 200 \mu\text{m}$ used as the starting configuration, (b) of the new probe positions after moving the voltage probes by a distance x , while the current probes remain in their positions, (c) of the voltage probes at a separation of $s = 20 \mu\text{m}$, and (d) of a different orientation of the probe configuration with vertical current flow.

with an equidistant probe spacing of $s = 200 \mu\text{m}$ as shown in figure 6.2 (a). Next, both voltage probes are moved a certain distance x closer to each other [see fig. 6.2 (b)], and for several distances x the resistance is determined via the measured I - V -curves (an exemplary I - V -curve is shown in the insert of fig. 6.3).

Additionally, different orientations of the probe configuration with respect to the x and y -axes are employed. Horizontal in-line configurations are shown in figure 6.2 (a) to (c), while a vertical configuration is shown in 6.2 (d). In all cases the spacing between the probes is in the μm range, while the sample thickness is $t = 40 \text{ nm}$. Thus, all measurements are clearly in the 2D transport regime. Note that under these conditions

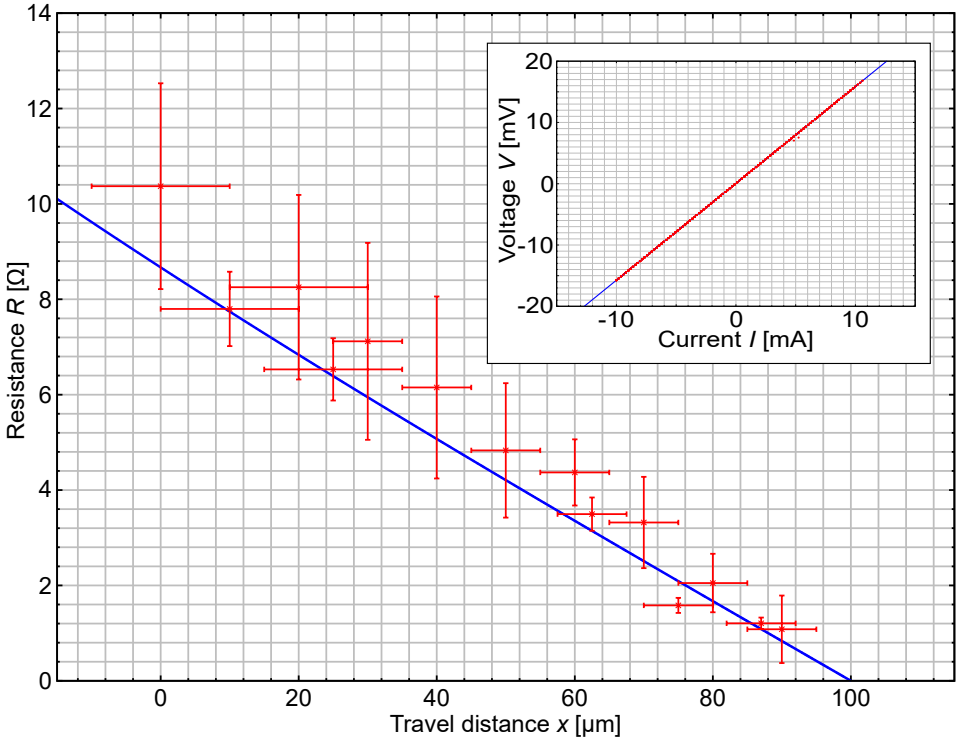


Figure 6.3.: Measured resistances R (red) versus equidistant travel distance x of the voltage probes. The blue line is a fit of the 2D equation for arbitrary probe positioning [equation (2.45)] to the data yielding $\rho_{\text{ab}} = (1.38 \pm 0.06) \mu\Omega\text{m}$. The insert shows a V - I -curve for $x = 90 \mu\text{m}$. Red dots are measured values (including error bars) and the blue line is a linear fit yielding $R = (1.5809 \pm 0.0005) \Omega$ and $V_0 = (61.9 \pm 0.3) \mu\text{V}$.

– 2D transport regime and in-line configuration – the measured resistances do not depend on the orientation of the in-line configuration or any (here for the hexagonal material unexpected) in-plane anisotropy (see discussion in section 3.3).

All in all there are 28 resistances measured at various x values. For each x , the mean R with an error bar obtained by averaging several measurements is plotted in figure 6.3. For x values, where only one R measurement could be obtained, a relative error of 10% is assumed, which is the expected error bar due to the uncertainty of the probe positioning of 5–10% as discussed in section 5.3. The errors for a few x values are significantly larger than the 10%, which is most likely related to the non-uniform surface as visible in the SEM images in figure 6.2, especially the horizontal scratches appearing bright in (d).

For irregular probe configurations with moving inner probes in the 2D transport regime the dependency between R and x is given by equation (2.45) derived in section 2.4. A fit of this function to the data is shown figure 6.3 as a solid blue line and yields $\rho_{ab} = (1.38 \pm 0.06) \mu\Omega\text{m}$. This low in-plane resistivity value confirms theoretical predictions [40, 41, 55, 105] and is also in the range of experimental values reported for various MAX phases [40, 55, 60, 106]. A detailed discussion this result and a comparison with literature will be given at the end of the next section.

6.3.2. Determining ρ_c/ρ_{ab} via the crossover function measured on a 155 nm thin-film sample

The 155 nm thin-film sample is measured with the in-line probe configuration with equidistant probe spacing s , i.e. in contrast to the previous section all probes (or at

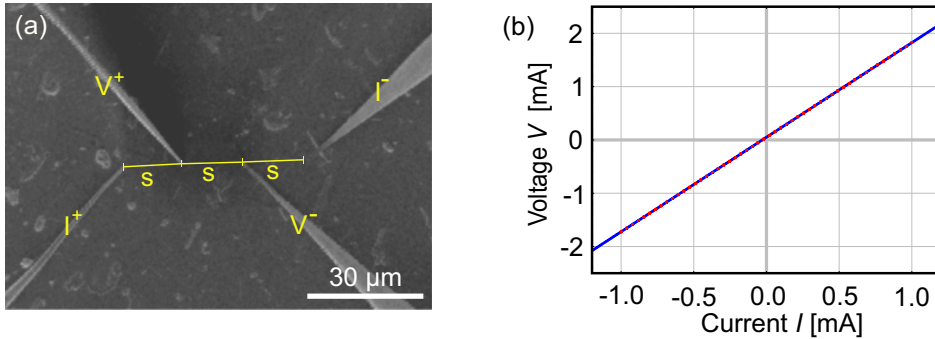


Figure 6.4.: 4-probe transport measurements of a 155 nm thick $(\text{Cr}_{0.5}\text{Mn}_{0.5})_2\text{GaC}$ film. (a) SEM image of an in-line configuration with equidistant probe spacing $s = 15 \mu\text{m}$. (b) V - I -curve for $s = 15 \mu\text{m}$. Red dots are measured values (including error bars) and the blue line is a linear fit yielding $R = (1.7738 \pm 0.0005) \Omega$ and $V_0 = (51.0 \pm 0.2) \mu\text{V}$. Figure is taken from Flatten et al. [61].

least three of them) need to be moved to change the parameter s . An example for $s = 15 \mu\text{m}$ is shown in figure 6.4 (a). Small bright spots on the surface are most likely due to gallium islands. A typically measured I - V -curve is shown in figure 6.4 (b) for $s = 15 \mu\text{m}$. The linear fit $V(I) = R \cdot I + V_0$ (blue curve) yields $R = (1.7738 \pm 0.0005) \Omega$ and $V_0 = (51.0 \pm 0.2) \mu\text{V}$. As before, the error bar of the resistance values is within 0.1%.

Figure 6.5 shows a compilation of 38 resistance measurements (red symbols) for a set of probe spacings ranging from $s = 1$ to $50 \mu\text{m}$ that were performed with numerous probes and at several spots of the sample surface as well as in different in-plane directions. For each probe spacing s , we plot the mean R with an error bar, both obtained by averaging

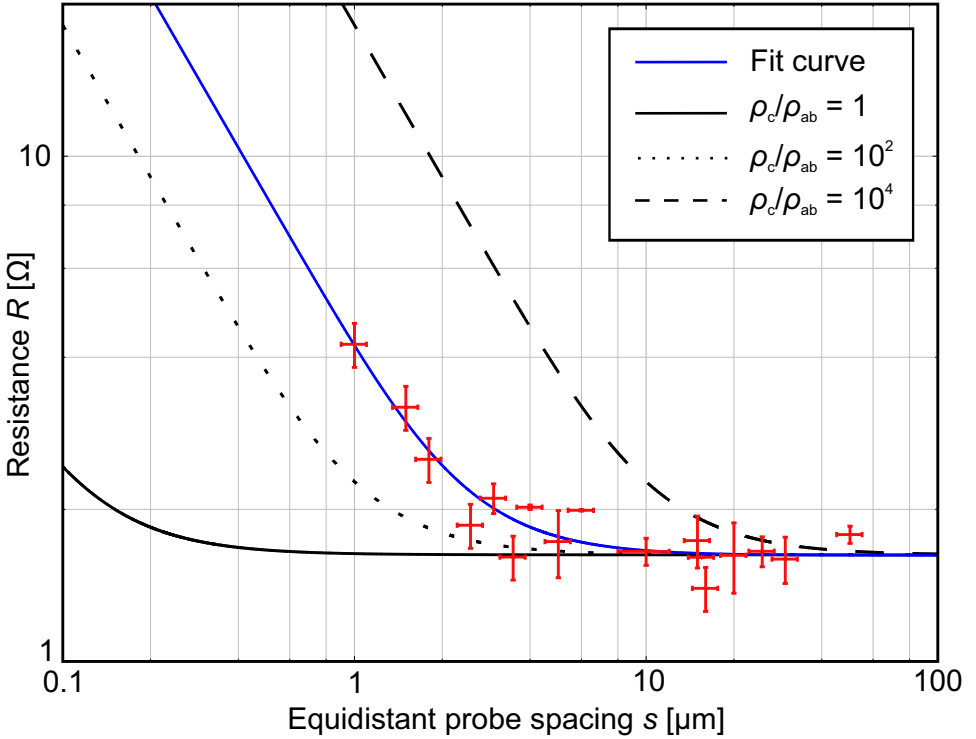


Figure 6.5.: Measured resistances R (red) versus equidistant probe spacing s . The blue curve is a fit of equation (3.10) to the data yielding $\rho_c/\rho_{ab} = (525 \pm 49)$. Black curves show for comparison the isotropic behavior (solid line) and anisotropic cases for anisotropy ratios 10^2 (dotted) and 10^4 (dashed). Figure is taken from Flatten et al. [61].

several measurements, each consisting of positioning and approach of the probes followed by recording and fitting a V - I -curve. The thus determined errors of R are typically about 10% that can be traced back to the uncertainty of the probe positioning, in particular along the line connecting the probes, of 5–10% as discussed in the section 5.3. For s values, where only one R measurement could be obtained, the same relative error is assumed. Obviously, R is constant for large s and increases for $s < 5\text{ }\mu\text{m}$. This behavior can be fitted in a parameter-free manner with the transient behavior described by equation (3.10) as shown by the solid blue line. For the present case, hexagonal crystal structure with isotropic in-plane resistivity $\rho_{ab} = \sqrt{\rho_x\rho_y}$ and $\rho_c = \rho_z$, equation (3.10) reads

$$R = \frac{\rho_{ab}}{\pi t} \cdot \ln \left(\frac{\sinh \left(\sqrt{\frac{\rho_c}{\rho_{ab}}} \cdot t/s \right)}{\sinh \left(\sqrt{\frac{\rho_c}{\rho_{ab}}} \cdot t/2s \right)} \right).$$

The least-square fitting simultaneously yields both $\rho_{ab} = (1.14 \pm 0.04)\text{ }\mu\Omega\text{m}$ and $\rho_c = (599 \pm 52)\text{ }\mu\Omega\text{m}$ leading to the anisotropy ratio $\frac{\rho_c}{\rho_{ab}} = 525 \pm 49$ and the 3D-2D crossover point according to equation (3.11) at $\zeta t = (2.6 \pm 0.1)\text{ }\mu\text{m}$.

The low in-plane resistivity $\rho_{ab} = (1.14 \pm 0.04)\text{ }\mu\Omega\text{m}$ is of the same order of magnitude as the value determined in the previous section 6.3.2 for the 40 nm film and thus agrees with theoretical predictions [40, 41, 55, 105] and previously reported experimental values for various MAX phases [40, 55, 60, 106]. The deviation of about 20% between the 40 and 155 nm films may be due to film-to-film variations, different thickness-dependent film microstructures and surface morphologies, or the inferior surface quality of the 40 nm sample [see large-scale scratches in fig. 6.2 (d)].

The in-plane resistivity $\rho_{ab} = 1.1\text{--}1.4\text{ }\mu\Omega\text{m}$ measured here for two films of different thickness compares well with the resistivity $\rho_{\text{poly}} = 2.2\text{ }\mu\Omega\text{m}$ reported by Lin et al. [106] for sintered polycrystalline $(\text{Cr}_{0.5}\text{Mn}_{0.5})_2\text{GaC}$ pellet samples, for which the impact of ρ_c is largely suppressed because the current paths can pass primarily in the ab -planes of the crystallites due to current percolation. While numerous theoretical reports predict that in MAX phases $\rho_c \gg \rho_{ab}$ [40, 41, 55], there are only very few experimental data on the anisotropy ratio and no previous measurement for the $(\text{Cr}_{0.5}\text{Mn}_{0.5})_2\text{GaC}$ MAX phase. The result $\frac{\rho_c}{\rho_{ab}} = 525 \pm 49$ clearly deviates from the isotropic case (black solid line in figure 6.5) found for the Ti_2GeC MAX phase [59] and also exceeds the ratio of 14–18 reported for the Ti_2AlC MAX phase [60]. On the contrary, it is of the same order of magnitude as reported for Cr_2AlC (300–475 at 300 K) and V_2AlC (3000–9000 between 300 and 4 K) MAX phases [55]. For comparison, the dotted and dashed lines in figure 6.5 indicate the transient behavior for $\rho_{ab} = 1.14\text{ }\mu\Omega\text{m}$ and anisotropy ratios 10^2 and 10^4 , respectively.

6.4. Summary and conclusions

In this chapter, I have presented electronic 4-point transport measurements on $(\text{Mn}_{0.5}\text{Cr}_{0.5})_2\text{GaC}$ magnetic MAX phase films that were provided by the group of J. Rosen at the Linköping University in Sweden. The complex bonding scheme of MAX phases that leads to anisotropic electronic transport properties was briefly introduced. The measurements of a 40 nm thick film are clearly to be assigned to the 2D transport regime ($t \ll s$) and therefore only allowed the determination of the in-plane resistivity component ρ_{ab} . On the contrary, the 155 nm thick film enabled the observation of the 2D-3D crossover such that I could measure both the in-plane and out-of-plane resistivity components of the nanolaminated MAX phase thin film. This was possible by using the crossover function that I have derived and described in section 3.2. To the best of my knowledge, this was the first measurement using this here specifically developed parameter-free experimental procedure on the basis of a 4-probe STM to determine ρ_{ab} and ρ_c of a single oriented thin-film sample. The method does neither require a specific device structure, nor a comparison of samples with different microstructure, or modelling of transport or effective medium properties (see discussion of previous work in chapter 1).

Concerning MAX phases, this novel method will allow systematic studies of the impact of the chemical composition on the resistivity tensor in order to achieve a deeper understanding of the electronic structure of MAX phases. The measured sizable resistivity anisotropy of a $(\text{Cr}_{0.5}\text{Mn}_{0.5})_2\text{GaC}$ MAX phase thin film $\rho_c/\rho_{ab} = 525 \pm 49$ reflects the complex bonding scheme of MAX phases with predominately covalent bonds in the basal planes as well as between the MX and A planes, but mixed with different degrees of metallicity and ionicity, resulting in the unique combination of metallic and ceramic properties of MAX phases. The presented data provide clear evidence for a sizable resistance anisotropy in a *magnetic* MAX phase, thus opening an avenue for investigating the so far unexplored interplay between electronic structure near the Fermi surface and the magnetic order that may add novel spintronic functionality to the versatile class of magnetic MAX phases.

The majority of these results has been published in Flatten et al. [61].

7. Electronic transport properties of an i-MAX phase – $(\text{Cr}_{2/3}\text{Ho}_{1/3})_2\text{AlC}$

Due to their unique structure $\text{M}_{n+1}\text{AX}_n$ with $n = 1, 2, 3$ MAX phases can be prepared in various solids with pure or mixtures of M elements [107]. Mixing different M' elements into traditional MAX phases led to the discovery of several sets of crystalline phases and allows tuning their physical properties. An example is the magnetic $(\text{Cr}_{0.5}\text{Mn}_{0.5})_2\text{GaC}$ phase discussed in the previous chapter. Recently, a large class of mixed $(\text{M}_{2/3}\text{M}'_{1/3})\text{AX}$ phases, where M' is a rare-earth element, was discovered [108–110]. Hybridization between $4f$ and conduction electrons promises a variety of electronic as well as magnetic ground states with possibly intriguing properties [110]. This is all the more true as these phases exhibit chemical order in the MXM' planes. According to this *in-plane* ordering, the name i-MAX phases has been coined for them [108]. It can be expected that the additional in-plane order gives rise to additional in-plane anisotropy, in particular for the conductivity. All i-MAX phases discovered up to now exhibit either a monoclinic or an orthorhombic crystal structure [110]. In this chapter, the focus is on $(\text{Cr}_{2/3}\text{Ho}_{1/3})_2\text{AlC}$, a very recently and so far unpublished i-MAX phase [111]. Thin $(\text{Cr}_{2/3}\text{Ho}_{1/3})_2\text{AlC}$ crystals with suitable thickness were kindly provided by Q. Tao from the Linköping University in Sweden. $(\text{Cr}_{2/3}\text{Ho}_{1/3})_2\text{AlC}$ exhibits an orthorhombic crystal structure [110] and is therefore well suited for the determination of in-plane (of course in addition to out-of-plane) conductivity anisotropy with the procedures that I have developed in chapter 3, in particular sections 3.3 and 3.4. To the best of my knowledge, this is the first experimental characterization of the anisotropic resistivity behaviour in an i-MAX phase.

In section 7.1, the general bonding structure of i-MAX phases is discussed, which is an indicator for anisotropic electronic transport properties, especially now also for in-plane anisotropy in the ab -plane, i.e. the MXM' planes. Section 7.2 introduces the two investigated samples, and the measurement procedure applied to the i-MAX samples is briefly shown. The results are presented in sections 7.3 and 7.4. Section 7.5 gives a summary and conclusions.

7.1. Theoretical background

As usual for MAX phases the $(\text{M}_{2/3}\text{M}'_{1/3})\text{AX}$ i-MAX phases also exhibit a layered structure [see fig. 7.1 (a) to (c)] [107]. The M atoms are arranged on a honeycomb lattice and the M' atoms on a triangular grid [see fig. 7.1 (d)]. An in-plane layer is formed containing $(\text{M}_{2/3}\text{M}'_{1/3})\text{X}$ elements. The A atoms form a Kagomé-like pattern, which is alternately with MXM' planes stacked along the c -axis [see fig. 7.1 (a) to (c)]. Depending on the

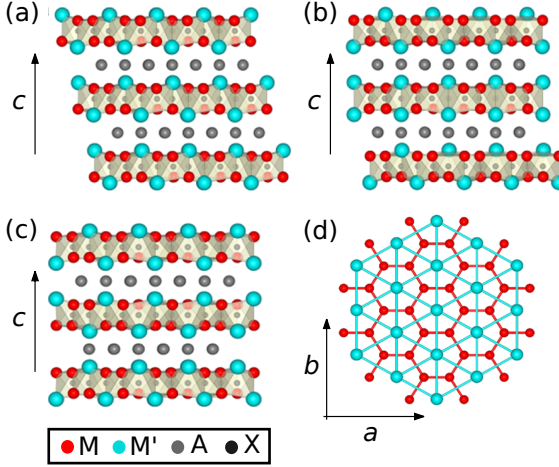


Figure 7.1.: Crystal structure of i-MAX phases. (a) and (b) show monoclinic structures with space groups $C_{2/c}$ and $C_{2/m}$, respectively. (c) shows the orthorhombic structure with space group C_{mcm} . (d) shows the chemically ordered M-M' layer. All figures taken from [110].

stacking pattern, i-MAX phases exhibit a monoclinic structure with space groups $C_{2/c}$ [see fig. 7.1 (a)] or $C_{2/m}$ [see fig. 7.1 (b)] or an orthorhombic structure with space group C_{mcm} [see fig. 7.1 (c)] [110]. As shown for numerous i-MAX phases the bonding structure is similar to the traditional MAX phases comprising chemical bonding anisotropy [107–109]. There are metallic-like bonds between the d -states of the M/M' atoms, strong hybridization between the d - and p -orbitals of the M/M' and X atoms as well as weak hybridization between the d - and p -orbitals of the M/M' and A atoms. Additionally, for some i-MAX phases a small out-of-plane bonding between the M atoms is found [108]. As known for traditional MAX phases, the metallic property of the i-MAX phases also originates mostly from the d -orbitals of the M/M' atoms. These states dominate the density of states at E_F , thus contribute mostly to electronic conductivity. The contribution of the M atoms is larger since there are more M than M' atoms in the unit cell [107]. Compared to the hexagonal MAX phase, the i-MAX phases comprise six times as many atoms per unit cell, which is of course also reflected in the electronic structure determined by DFT calculations [108]. The band structure exhibit significantly more bands than the traditional MAX phases. One fingerprint of the latter phases is that they contain no band-crossing at E_F along the c -axis, which indicates the large conductivity anisotropy measured in chapter 6. For some i-MAX phases it was shown that several bands cross the Fermi level along in-plane as well as out-of-plane directions, which should lead to

a less anisotropic resistivity behaviour [108]. The investigated $(\text{Cr}_{2/3}\text{Ho}_{1/3})_2\text{AlC}$ i-MAX phase comprises an orthorhombic structure [111]. Referring to section 3.2, the resistivity tensor in this case exhibits three independent components, in particular ρ_a and ρ_b along two orthogonal in-plane directions and ρ_c aligned along the out-of-plane c -axis. In-plane and out-of-plane resistivity anisotropy is expected due to the in-plane chemical ordering and the layered crystal structure, respectively. However, the less anisotropic band structure should result in a weaker out-of-plane resistivity anisotropy than for traditional MAX phases, and – to the best of my knowledge – the in-plane resistivity anisotropy has so far only been predicted, but not yet experimentally verified.

7.2. Experimental procedure

The $(\text{Cr}_{2/3}\text{Ho}_{1/3})_2\text{AlC}$ samples were prepared at Linköping University by Q. Tao in the group of J. Rosen, who kindly provided the description of the novel sample preparation and XRD data before publication [111]. The crystals were grown by the flux method, which is here just briefly introduced. Elemental powder with a molar ratio of $\text{Cr}:\text{Ho}:\text{Al}=0.18:0.36:0.1$ is mixed in a mortar, which is afterwards placed in an Al_2O_3 crucible and heated in a tube furnace under flowing Ar up to 1600°C for 60 min. Then the specimen is cooled down slowly to 1200°C in 2400 min, then to 800°C , and finally to room temperature. Afterwards, the furnace is removed and the specimen is stored in air for several days to oxidize the excess Ho. Several days later the remaining pellets are immersed in 0.5 mol HCl for 1 h to remove the remaining intermetallics. After this preparation, shiny pellets with a size of up to few mm^3 are obtained.

These crystals are further investigated by XRD as shown in figure 7.2. The Rietveld refinement of an XRD spectrum taken of crushed crystals confirms the space group C_{mcm} . The agreement is very good with $\chi^2 = 2.39$ and $R_{\text{wp}} = 11.7$ [112]. Other typical i-MAX phase structures like $C_{2/c}$ and $C_{2/m}$ have also been considered, but give much worse agreements. Thus $(\text{Cr}_{2/3}\text{Ho}_{1/3})_2\text{AlC}$ exhibits the space group C_{mcm} representing nothing else than an orthorhombic crystal system. Furthermore, XRD of the platelet-shaped crystals used for electronic transport measurements proves that the a and b -axes are lying in the surface plane and the c -axis along the surface normal. However, the in-plane orientation, explicitly the position of the a and b -axes with respect to the sample edges, was not known when the transport measurement were performed. Regarding the notation used in chapter 3, only $\rho_c \equiv \rho_z$ could be identified as the out-of-plane resistivity. The exact position of the a and b -axes relevant for the ρ_a and ρ_b components is described in section 7.3. As discussed in chapter 3, first the in-plane resistivities are characterized using a rotating square configuration and then the out-of-plane resistivity can be determined via the crossover function for arbitrary probe positioning by varying the edge length of the square configuration.

The 4-probe electronic transport measurement are performed at room temperature using self-made tungsten probes as described previously. Before the transport measure-

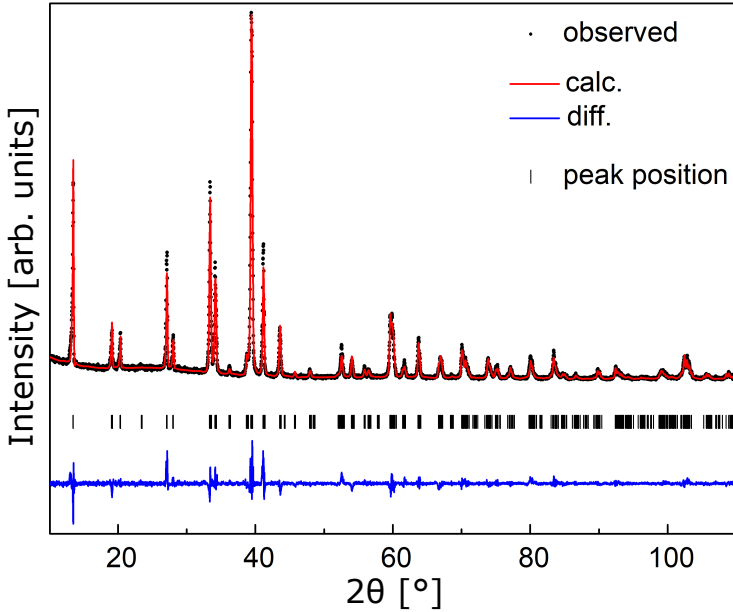


Figure 7.2.: Rietveld refinement of an XRD spectrum of $(\text{Cr}_{2/3}\text{Ho}_{1/3})_2\text{AlC}$ crushed crystals confirming the space group C_{mcm} . Measurement and figure are kindly provided by Q. Tao, Linköping University.

ment the platelet-shaped $(\text{Cr}_{2/3}\text{Ho}_{1/3})_2\text{AlC}$ crystal was clamped onto a mica substrate and in-situ annealed at 150°C for 1 h to desorb physisorbed contaminants from the chemically inert surface. For each resistance measurement the probes are positioned under SEM control in a square configuration, which is rotated by certain angles θ to determine the in-plane anisotropic transport properties as described in section 7.3. In section 7.4 the edge length s of the square configuration is varied to determine the out-of-plane resistivity. After positioning, each probe is approached into the tunneling regime (typically 10 nA tunneling current at 1 V bias voltage) using the approach procedure of the STM controller. Finally, the probes are individually moved (using the z -axes of the STM piezo scanners) by $\Delta z = 1\text{-}2\text{ nm}$ towards the sample to establish ohmic contacts. As described previously, the probes are disconnect from the STM controller and connected to a current source and voltmeter. The injected current is swept from -1.0 to $+1.0\text{ mA}$ to record V - I -curves, from which the resistances R are determined. The measured resistances are finally plotted versus the rotation angle θ or the edge length s .

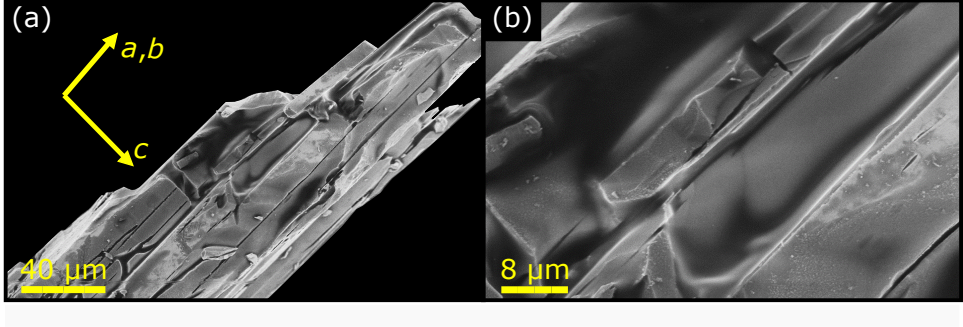


Figure 7.3.: Cross-sectional SEM images of a $80\text{ }\mu\text{m}$ thick $(\text{Cr}_{2/3}\text{Ho}_{1/3})_2\text{AlC}$ platelet-shaped crystal at different magnifications. Several black lines in the ab -plane indicate gaps between partly delaminated $10\text{-}30\text{ }\mu\text{m}$ thick lamellae.

A last important point to mention is that the effective thickness of the measured crystals is unknown. The nominal thickness of the platelet-shaped $(\text{Cr}_{2/3}\text{Ho}_{1/3})_2\text{AlC}$ crystals ranges between 60 and $150\text{ }\mu\text{m}$. However, cross-sectional SEM images (fig. 7.3) show black lines in the ab -plane, which very likely represent gaps between partly delaminated lamellae. As seen in figure 7.3, the thickness of the delaminated lamellae is strongly position-dependent and ranges between 10 and $30\text{ }\mu\text{m}$. Such delamination is tightly connected to the layered structure and thus not surprising. The gaps are an indication for weak bonding between the MXM' and A layers that has been explored to prepare 2D materials of several parenting i-MAX phases, so-called i-MXenes, by exfoliation [107, 108, 113, 114]. In the present context, however, the delamination leads to an ill-defined thickness t of the lamellae that are relevant for the quantitative analysis the here presented electronic transport measurements. This issue will be discussed later in more detail.

7.3. Characterization of the in-plane resistivities components

In this section, the in-plane anisotropic transport properties of the $(\text{Cr}_{2/3}\text{Ho}_{1/3})_2\text{AlC}$ i-MAX phase are discussed. Three independent measurements on different spots on the sample are performed. One of them is explained in the following in more detail.

As seen in figure 7.4, the four STM-probes contact the sample in a square configuration. As discussed in section 3.3, a rotating square configuration is the best choice to characterize an in-plane anisotropic resistivity. The SEM imaging software is used to rotate the square configuration about a certain angle θ . Figure 7.4 (a) shows a zoom-out SEM image. The yellow arrows define the angles $\theta = 0^\circ$ and 90° according to the coordinate system of the SEM software. The green arrows indicate the crystalline a and b -axes

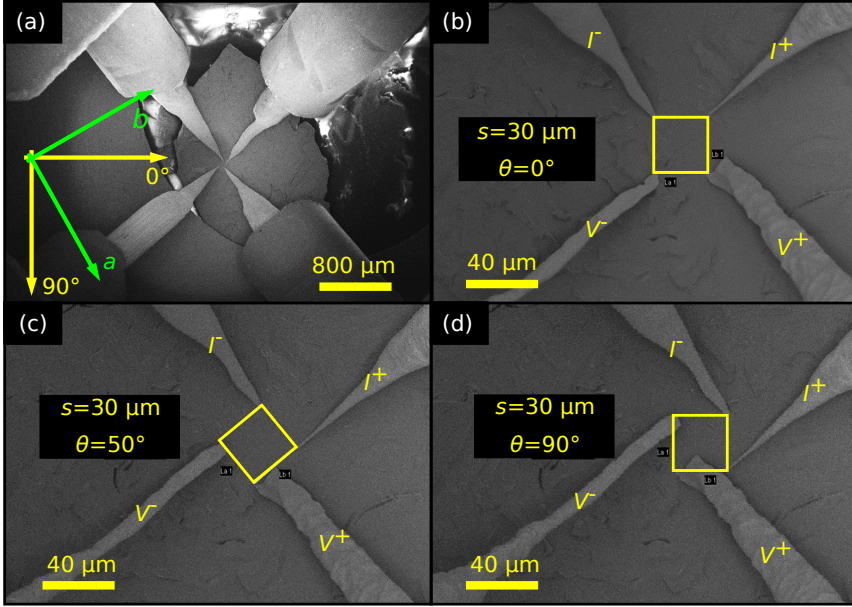


Figure 7.4.: 4-probe configurations for electronic transport measurements on a $(\text{Cr}_{2/3}\text{Ho}_{1/3})_2\text{AlC}$ crystal. (a) shows an overview of the platelet-shaped crystal contacted by 4 probes. The yellow arrows indicate the coordinate system of the SEM software which defines the rotation angle θ . The green arrows symbolize the crystalline a and b -axes of the platelet. (b) to (d) show 4-probe square configurations with fixed edge length $s = 30 \mu\text{m}$, but different rotation angles $\theta = 0^\circ$, 50° , and 90° .

as will be discussed below. In figure 7.4 (b), a square configuration with edge length $s = 30 \mu\text{m}$ is shown for $\theta = 0^\circ$. This square is then rotated clockwise [see fig. 7.4 (c) for $\theta = 50^\circ$ and (d) for $\theta = 90^\circ$]. The resistance R is measured for 12 θ values yielding the plot R versus θ shown in figure 7.5. Each R in the plot is measured either with a single measurement or by two repeated measurements, re-positioning the probes each time. The error bars of R in figure 7.5 represent the typically expected error of 10% (refer to chapters 5 and 6). The resistance values are in the range of 3 to 6 m Ω revealing a metal-like behaviour in agreement with literature for different i-MAX phases [110]. The resistance values systematically depend on the angle θ with a maximum between 40° and 60° , clearly indicating an in-plane anisotropy.

If the measurements are performed in the 2D transport regime, then the $R(\theta)$ de-

pendence is given by equation (3.17), which allows for $\rho_a \neq \rho_b$. In order to fulfill this condition, the edge length s of the square configuration must be long enough. Additional transport measurements with an in-line configuration with equidistant probe spacing s ranging from 20 to 70 μm confirm that the measurements in square configuration with $s = 30 \mu\text{m}$ in figure 7.5 are in the 2D regime and, hence, that equation (3.17) can be applied.

However, equation (3.17) also depends on the sample thickness t , which is not precisely known for the $(\text{Cr}_{2/3}\text{Ho}_{1/3})_2\text{AlC}$ samples due to the gaps caused by delamination (see fig. 7.3). Luckily, the variable t only occurs in the pre-factor, which is expressed in the following as $A = \frac{\sqrt{\rho_x \rho_y}}{2\pi t}$ and yields a rewritten expression of equation (3.17)

$$R(\theta, \rho_x, \rho_y, A) = A \cdot \ln \left(\frac{\left(1 + \frac{\rho_y}{\rho_x}\right)^2 - 4 \cos^2(\theta) \sin^2(\theta) \left(1 - \frac{\rho_y}{\rho_x}\right)^2}{\left(\sin^2(\theta) + \frac{\rho_y}{\rho_x} \cos^2(\theta)\right)^2} \right), \quad (7.1)$$

with the unknown variables ρ_x , ρ_y , and A . Note that equations (3.17) and (7.1) assume that $\theta = 0$ corresponds a current flow from I^+ to I^- in x -direction. As the orientation of the a and b -axes was not known at the moment of the measurements, an additional phase shift ϕ is added to the angle θ . Using the in-plane anisotropic ratio $r = \frac{\rho_y}{\rho_x}$ one obtains

$$R(\theta, r, A, \phi) = A \cdot \ln \left(\frac{(1+r)^2 - 4 \cos^2(\theta + \phi) \sin^2(\theta + \phi) (1-r)^2}{(\sin^2(\theta + \phi) + r \cos^2(\theta + \phi))^2} \right). \quad (7.2)$$

This equation is fitted to the measured R yielding $A = (6.20 \pm 0.15) \text{ m}\Omega$, $r = 1.59 \pm 0.08$ and $\phi = (33.8 \pm 2.1)^\circ$ (blue line in fig. 7.5). Assuming that the thickness of the measured, top-most lamella is in the range between 10 and 30 μm , one obtains $\rho_x = 0.29 \dots 0.88 \mu\Omega\text{m}$ and $\rho_y = 0.47 \dots 1.41 \mu\Omega\text{m}$.

The maximum and minimum of the $R(\theta)$ curve are at $90^\circ - \phi = (56.2 \pm 2.1)^\circ$ and at $0^\circ - \phi = (-33.8 \pm 2.1)^\circ$, respectively. These directions are marked in figure 7.4 (a) by green arrows. After completing all transport measurements the sample was sent to Q. Tao at the Linköping University in Sweden to determine the crystalline axes. For the very same crystallite that was used for transport measurements and could be identified using the SEM image in figure 7.4 (a), the green arrows were found to coincide with the a and b -axes, as labelled in figure 7.4 (a) [111]. This result allows the assignments $\rho_a = \rho_y$ and $\rho_b = \rho_x$. Note in figure 7.4 (a) that the phase shift ϕ indicates the offset between the x -axis ($\theta = 0^\circ$) and b -axis and between the y -axis ($\theta = 90^\circ$) and a -axis, respectively.

$R(\theta)$ measurements are repeated at two further locations on the same crystallite surface and with different edge lengths of the square configuration, $s = 60 \mu\text{m}$ [see fig. 7.6 (a)] and $s = 30 \mu\text{m}$ [see fig. 7.6 (b)]. For the location, where the $s = 30 \mu\text{m}$ data was taken, an additional measurement with an in-line probe configuration confirmed 2D

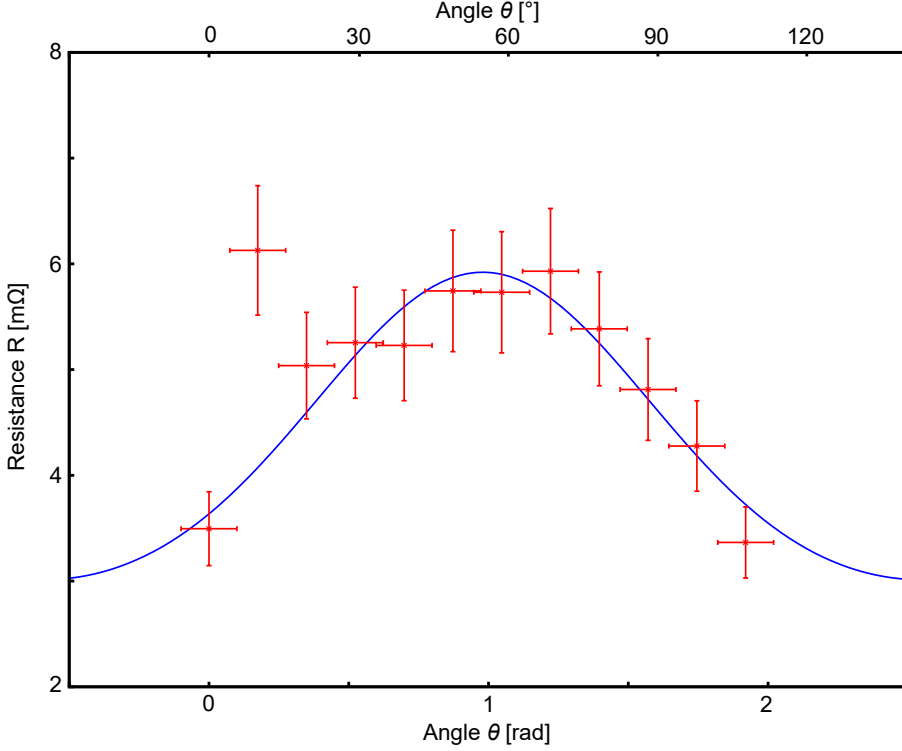


Figure 7.5.: In-plane resistivity anisotropy of $(\text{Cr}_{2/3}\text{Ho}_{1/3})_2\text{AlC}$. Measured resistance R (red) versus the rotation angle θ of the 4-probe square configuration. The blue line is a fit to equation (7.2) yielding $r = \frac{\rho_y}{\rho_x} = (1.59 \pm 0.08)$.

transport behavior for $s = 30 \mu\text{m}$, meaning that the local lamella thickness t is small enough. The location, where the $s = 60 \mu\text{m}$ data was taken, was also used for the measurement of the out-of-plane resistivity anisotropy by varying the edge length of the square configuration (see section 7.4). The resulting crossover function shown in figure 7.8 indicates that for this location $s = 60 \mu\text{m}$ is only slightly larger than the crossover point. Hence, deviations from the 2D transport regime are to be expected.

The blue lines in figure 7.6 are fits to equation (7.2), which yield an anisotropic ratio of $r = 1.93 \pm 0.15$ for $s = 60 \mu\text{m}$ (a) and $r = 1.33 \pm 0.10$ for $s = 30 \mu\text{m}$ (b). The $s = 60 \mu\text{m}$ data yields a significantly larger value than the $s = 30 \mu\text{m}$ data. This is most likely due to deviations from the 2D transport regime at $s = 60 \mu\text{m}$. Therefore, this value is not taken into account when calculating the average parameters $r^{\text{mean}} = 1.46 \pm 0.13$, $A = (5.7 \pm 0.4) \text{ m}\Omega$, and $\phi^{\text{mean}} = (34.6 \pm 3.5)^\circ$. The deviations between the two fitted

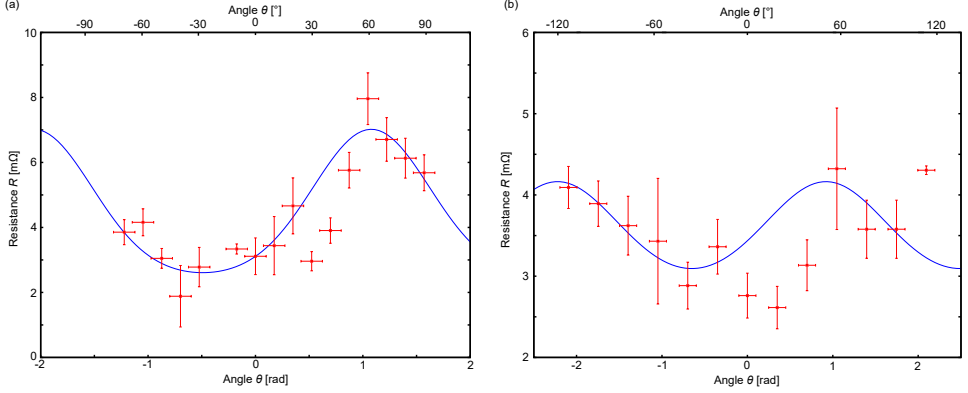


Figure 7.6.: In-plane resistivity anisotropy of $(\text{Cr}_{2/3}\text{Ho}_{1/3})_2\text{AlC}$. Additional measurements of the $R(\theta)$ dependence (red) taken at two further locations on the crystal surface and with different $s = 60 \mu\text{m}$ for (a) and $s = 30 \mu\text{m}$ for (b). The blue lines are fits to equation (7.2) yielding for $r = \frac{\rho_a}{\rho_b} = 1.93 \pm 0.15$ for (a) and $r = \frac{\rho_a}{\rho_b} = 1.33 \pm 0.10$ for (b).

anisotropy results can be predominantly related to the quite rough crystal surface visible in figures 7.4 and 7.7.

The result that $r = \frac{\rho_a}{\rho_b} > 1$ means that $\rho_a > \rho_b$. For $(\text{Cr}_{2/3}\text{Ho}_{1/3})_2\text{AlC}$ and numerous other i-MAX phases the unit cell is larger in a -direction than in b -direction [107–110], see figure 7.1 (d). In particular, the triangular grid of the M' atoms consists of rows of nearest-neighbor M' atoms that are not present in the a -direction. In contrast, the a and b -directions are equivalent for the honeycomb lattice of the M atoms. Therefore, the in-plane anisotropy with lower resistivity component ρ_b can be qualitatively linked to enhanced transport mediated by metallic d - d nearest-neighbor bonds along the b -direction of the two-dimensional M' sublattice.

To the best of my knowledge, the electronic transport measurements presented in this section represent the first determination of the in-plane resistivity anisotropy originating from the crystal structure of an i-MAX phase. The orthorhombic $(\text{Cr}_{2/3}\text{Ho}_{1/3})_2\text{AlC}$ i-MAX phase reveals a metal-like resistivity behaviour and a small, but significant in-plane anisotropy with the ratio $r = \frac{\rho_a}{\rho_b} = 1.46 \pm 0.13$.

7.4. Determination of the out-of-plane resistivity component

In this section, the determination of the out-of-plane resistivity for the same $(\text{Cr}_{2/3}\text{Ho}_{1/3})_2\text{AlC}$ crystallite is discussed. To this end, the edge length s of a square

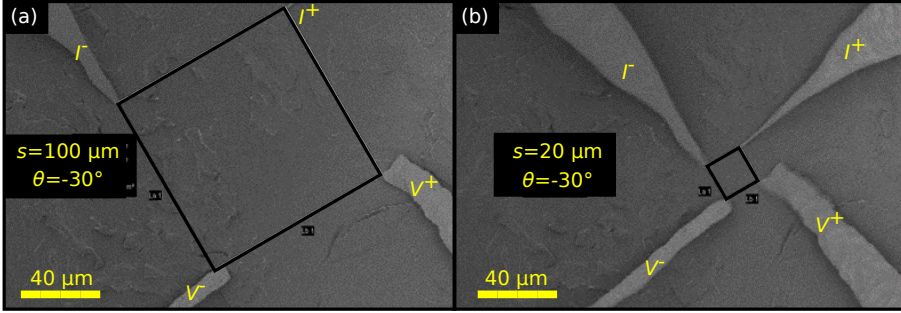


Figure 7.7.: 4-probe configurations for electronic transport measurements on a $(\text{Cr}_{2/3}\text{Ho}_{1/3})_2\text{AlC}$ crystal. The edge length of the square configuration is $s = 100 \mu\text{m}$ for (a) and $s = 20 \mu\text{m}$ for (b), while the rotation angle is fixed at $\theta = -30^\circ$.

configuration is varied from 100 to $5 \mu\text{m}$ as shown in figure 7.7 for $s = 100 \mu\text{m}$ (a) and $s = 20 \mu\text{m}$ (b). Note that the angle of the resistance measured is fixed at $\theta = -30^\circ$ such that the current is applied along the b -axis of the crystal.

The dependence of the measured resistance R (red) on s is plotted in figure 7.8, where each R is measured at least three times, each after re-positioning the probes. The course of the resistance values shows the crossover between the 3D and 2D transport regimes as discussed in sections 3.2 and 3.3. Concerning the measurement protocol, first the edge length of the square is varied. At first glance, the R values do not strongly vary for $s \geq 50 \mu\text{m}$. This suggests that there is a clear 2D transport behavior, wherefore the square configuration is then rotated with $s = 60 \mu\text{m}$ to measure the data in figure 7.6 (a) and to determine the in-plane anisotropy (see section 7.3).

The crossover function [equation (3.12)] for the here shown scenario with the current applied along the b -axis is given by

$$R_{\text{square}} = \frac{\sqrt{\rho_b \rho_a}}{\pi t} \cdot \ln \left(\frac{\sinh \left(\sqrt{\frac{\rho_c}{\rho_a}} \frac{t}{s} \right)}{\sinh \left(\sqrt{\frac{\rho_c}{\rho_a + \rho_b}} \frac{t}{s} \right)} \right). \quad (7.3)$$

Apparently, the crossover function $R_{\text{square}}(s)$ depends on four parameters, namely the resistivity components ρ_a , ρ_b , ρ_c , and the lamella thickness t . However, there are only three independent parameters. This can be easily seen with the substitutions $\rho_a = \alpha t$,

$\rho_b = \beta t$, and $\rho_c = \gamma/t$, which eliminate the parameter t from equation (7.3).

$$R_{\text{square}} = \frac{\sqrt{\alpha\beta}}{\pi} \cdot \ln \left(\frac{\sinh \left(\sqrt{\frac{\gamma}{\alpha}} \frac{1}{s} \right)}{\sinh \left(\sqrt{\frac{\gamma}{\alpha+\beta}} \frac{1}{s} \right)} \right). \quad (7.4)$$

Hence, determining of the resistivity components is only possible, if the lamella thickness t is known. Furthermore, the fitting in the previous section 7.3 yielded the in-plane anisotropy ratio $r = \frac{\rho_a}{\rho_b} \equiv \frac{\alpha}{\beta} = 1.46 \pm 0.13$, which reduces the number of fit parameters in equation (7.4) to only two (e.g. β and γ). The corresponding fit with fixed $\alpha = 1.46\beta$

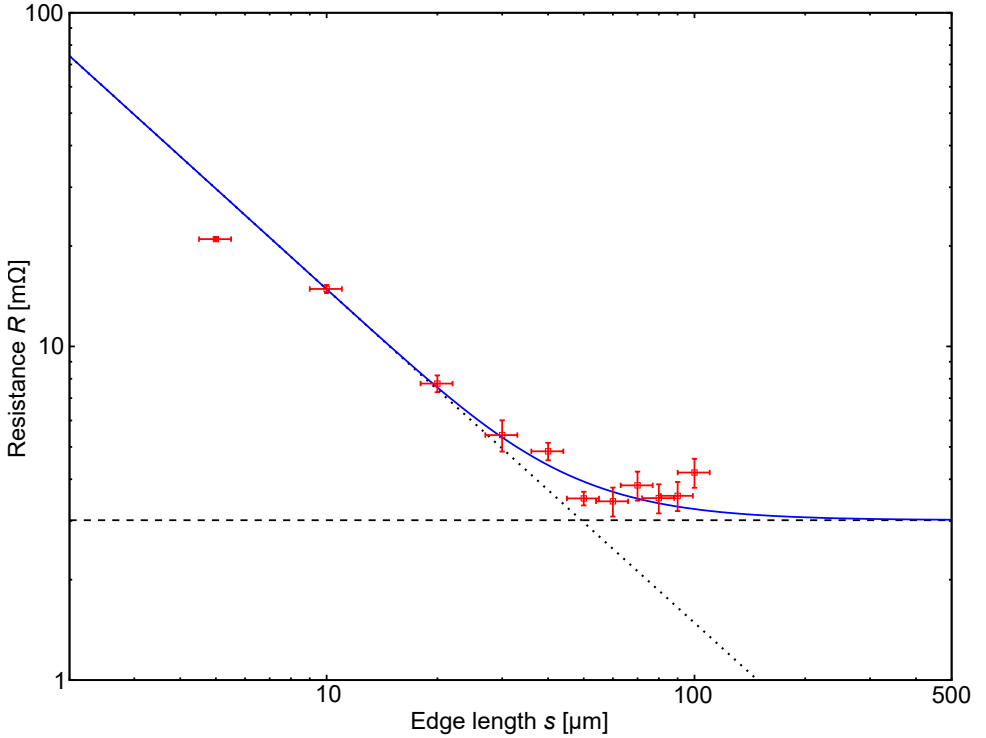


Figure 7.8.: Out-of-plane resistivity anisotropy of $(\text{Cr}_{2/3}\text{Ho}_{1/3})_2\text{AlC}$. Measured resistance R (red) versus the edge length s of the 4-probe square configuration. The blue line is a fit to equation (7.4) performed with fixed $\alpha = 1.46\beta$, which yields $\beta = (0.030 \pm 0.002) \Omega$ and $\gamma = (137 \pm 15) \Omega \mu\text{m}^2$. The dashed and dotted lines indicate the 2D and 3D transport cases, respectively.

is shown as a blue line in figure 7.8. The fit results are $\beta = (0.030 \pm 0.002)\Omega$ and $\gamma = (137 \pm 15)\Omega\mu\text{m}^2$.

Although the lamella thicknesses t relevant for the different measurements are not known in detail, the probable thickness range $t = 10 \dots 30\mu\text{m}$ can be estimated from cross-sectional SEM images (e.g. fig. 7.3). Table 7.1 compiles the resulting ranges for the resistivity components and the anisotropy ratios.

Lamella thickness t [μm]	$\rho_a = \alpha t$ [$\mu\Omega\text{m}$]	$\rho_b = \beta t$ [$\mu\Omega\text{m}$]	$\rho_c = \gamma t^{-1}$ [$\mu\Omega\text{m}$]	$\frac{\rho_a}{\rho_b} = \frac{\alpha}{\beta}$	$\frac{\rho_c}{\sqrt{\rho_a\rho_b}} = \frac{\gamma}{\sqrt{\alpha\beta}}t^{-2}$
10	0.44	0.30	13.7	1.46	37.7
\vdots	\vdots	\vdots	\vdots	\vdots	\vdots
30	1.32	0.90	4.38	1.46	4.0

Table 7.1.: Ranges for the resistivity components, the in-plane anisotropy ratio, and the out-of-plane anisotropy ratio under the assumption of a lamella thickness range from $t = 10$ to $30\mu\text{m}$. The uncertainty of the lamella thickness t makes a precise determination of the resistivity components impossible. Therefore, error margins resulting from the fits are omitted for clarity.

The fitted curve in figure 7.8 shows that capturing of the entire crossover region well into the 2D regime would require significantly longer edge lengths s exceeding $100\mu\text{m}$. This was not feasible for the present $(\text{Cr}_{2/3}\text{Ho}_{1/3})_2\text{AlC}$ sample due to structural inhomogeneity of the surface that is probably caused by delamination. Nevertheless, the presented measurements reveal a stronger out-of-plane than in-plane resistivity anisotropy. The out-of-plane anisotropy ratio is smaller than that of the traditional MAX phase discussed in chapter 6. This is in agreement with the less anisotropic band structure of the i-MAX phases.

7.5. Conclusion

In this chapter, I have presented electronic 4-point transport measurements on $(\text{Cr}_{2/3}\text{Ho}_{1/3})_2\text{AlC}$ i-MAX phase crystallites, which were prepared at Linköping University by Q. Tao in the group of J. Rosen. In i-MAX phases, the chemical order of the M and M' atoms (here Cr and Ho) in the ab -plane reduces the crystal symmetry compared to the conventional MAX phases. $(\text{Cr}_{2/3}\text{Ho}_{1/3})_2\text{AlC}$ has orthorhombic symmetry that leads to a diagonal resistivity tensor with three independent components, allowing for anisotropic resistivity in the ab -plane. To the best of my knowledge, the data presented in this chapter revealing $\frac{\rho_a}{\rho_b} = 1.46 \pm 0.13$ represent the first experimental evidence for such an in-plane resistivity anisotropy in an i-MAX phase. Furthermore, the major axes of the resistivity tensor in the surface plane are found to coincide with the a and b -axes determined by XRD. The lower resistivity component in b -direction ρ_b can be qualita-

tively explained by enhanced transport mediated by metallic d - d nearest-neighbor bonds along the b -direction of the two-dimensional M' sublattice.

With the measurement protocols developed in chapter 3, I was also for the first time able to simultaneously characterize the out-of-plane and in-plane resistance, i.e. the entire resistance tensor of an i-MAX phase. Unfortunately, the thickness of the measured crystallites ($t = 10 \dots 30 \mu\text{m}$) were not precisely known due to partial delamination of the material. For that reason, only value ranges could be determined for the absolute magnitudes of the resistivity components and the out-of-plane resistivity ratio. The in-plane resistivity components ρ_a and ρ_b are of the order of $1 \mu\Omega\text{m}$ and ρ_c is about one order of magnitude larger, indicating good metallic behavior in agreement with literature on other i-MAX phases. The out-of-plane anisotropy ratio $\frac{\rho_c}{\sqrt{\rho_a\rho_b}}$ is in the range between 4 and 40. The stronger out-of-plane than in-plane anisotropy ratio is compatible with the bonding scheme of i-MAX phases, which is similar to that of conventional MAX phases. However, the unit cell of i-MAX phases is larger and results in a larger number of electronic bands crossing the Fermi energy, including some in c -direction. This explains the reduced out-of-plane resistivity anisotropy of $(\text{Cr}_{2/3}\text{Ho}_{1/3})_2\text{AlC}$ compared to conventional MAX phases, such as $(\text{Mn}_{0.5}\text{Cr}_{0.5})_2\text{GaC}$ investigated in chapter 6 with $\frac{\rho_c}{\rho_a} = 525 \pm 49$.

Finally, I want to emphasize that I have given in this chapter first proof-of-principle for the quantitative determination of the entire resistivity tensor of a material with orthorhombic or higher symmetry on basis of electronic 4-probe transport measurements performed on a single sample of a given (and known) thickness.

8. Summary and Outlook

This thesis emphasizes the possibilities of characterizing resistivity properties of a sample by using a 4-probe STM. Besides the constant progress in developing the 4-probe STM for measuring resistances in the nanoscale regime, there are several opportunities using the features of a 4-probe STM to analyse electronic transport properties of a sample, in particular the variable probe positioning.

Nowadays materials with layered structures are in the focus of interest since they are possible parent-materials for samples with one or a few atomic layers known as 2D materials. According to the layered structure, these materials grown as epitaxial thin films typically comprise a bonding anisotropy and thus an anisotropic resistivity, where the out-of-plane resistivity component usually differs due to the oriented growth along the c -axis, i.e. the out-of-plane resistivity is typically larger than the in-plane resistivities. There are straight-forward methods for the characterization of anisotropic in-plane transport behaviour, but the determination of an out-of-plane resistivity is quite challenging (refer to chapter 1). Therefore, this thesis presents a specifically developed parameter-free experimental method for the direct determination of an out-of-plane resistivity.

Briefly summarized, this method is based on the crossover between the 2D and 3D electronic transport case. The dependency between the resistivity and the resistance measured in a 4-point measurement is introduced to discuss the counterintuitive behaviour of the 2D ($R \propto t$) and 3D ($R \propto s$) transport cases. Subsequently, the crossover between the two regimes is described, which is the key to the measurement protocol for the direct determination of the out-of-plane resistivity. A novel solution to characterize the crossover between 2D and 3D regime for arbitrary probe positioning is presented in this thesis, too.

Anisotropic electronic transport can be analysed by introducing the resistivity as a second rank tensor, whereby here the focus is on crystal symmetries exhibiting a diagonal resistivity tensor (orthorhombic and higher symmetry). The van der Pauw transformation is used to determine the up to three independent resistivity tensor components. In-plane resistivity components can be easily determined in the 2D transport case using a rotating square configuration of the probes. On the other hand, transient behaviour between the 2D and 3D regime obtained by variation of probe spacing and described by the crossover function is used to obtain the out-of-plane resistivity. Therefore, the novel method for determining the out-of-plane resistivity is based on the crossover function, which I have reformulated for anisotropic materials using the van der Pauw transformation.

After calibration and testing of the experimental setup, measurements of a thin cooper stripe and a gold film are presented to verify the theory behind the transport measure-

ments, but also point out some challenges one has to care about, like a gentle probe approach with a minimal penetration depth into the sample, surface and film quality as well as different contributions of error sources emerging during the measurement. Possible error sources are discussed in more detail and it is found that the largest error of consecutive resistance measurements results from the inaccuracy of the probe positioning.

As a first key result of this thesis, I have simultaneously measured the in-plane and perpendicular-to-plane resistivity, and thus the out-of-plane resistivity anisotropy, of a nanolaminated MAX phase thin film using the here developed method. These measurements represent proof-of-principle for future investigations about the dependency between the chemical composition and the resistivity tensor in MAX phase films with hexagonal crystal structure. The measured resistivity anisotropy of the magnetic $(\text{Cr}_{0.5}\text{Mn}_{0.5})_2\text{GaC}$ MAX phase $\rho_c/\rho_{ab} = 525 \pm 49$ is sizable and reflects the complex bonding scheme of MAX phases. Relating the magnetic properties of MAX phases to transport properties of this kind opens an avenue for investigating the so far unexplored interplay between electronic structure near the Fermi surface and the magnetic order that may add novel spintronic functionality to the versatile class of magnetic MAX phases. As an outlook, electronic transport measurements with an applied magnetic field should give more insight into the electronic and magnetic properties. However, the LT Nanoprobe only enables measurement with an applied magnetic field of 25 mT perpendicular to the sample surface, and furthermore the measurement temperature is fixed at about 4 K due to the superconducting coil used.

Finally, I have also measured the electronic transport properties of the $(\text{Cr}_{2/3}\text{Ho}_{1/3})_2\text{AlC}$ i-MAX phase. The chemical in-plane ordering of i-MAX phases is predicted to lead to in-plane anisotropic properties. Indeed, my experiments represent the first experimental verification of anisotropic transport properties in i-MAX phases in in-plane as well as out-of-plane direction. The measurements have been performed on a crystal sample for which partial delamination of crystalline lamellae leads at the sample surface to platelet-shaped crystallites with an ill-defined thickness. The in-plane anisotropic resistivity ratio could be accurately determined in the 2D regime yielding $\frac{\rho_a}{\rho_b} = 1.46 \pm 0.13$, thus $\rho_a > \rho_b$. Cross-sectional SEM images indicate crystallite thicknesses between 10 and $t = 30\mu\text{m}$. Using this value range, one can estimate value ranges for all three resistivity components. It turns out the the out-of-plane anisotropy ratio $\frac{\rho_c}{\sqrt{\rho_a\rho_b}}$ is at least one order of magnitude smaller than for the conventional $(\text{Cr}_{0.5}\text{Mn}_{0.5})_2\text{GaC}$ MAX phase and thus confirms predictions based on previous DFT band structure calculations for other i-MAX phases.

At the very moment of writing this thesis, Q. Tao has prepared structurally better crystals with a significantly flatter surfaces and also better defined thicknesses [111]. Therefore, the transport measurements performed in chapter 7 should be repeated on those crystals to quantitatively determine all three resistivity components ρ_a , ρ_b , and ρ_c for a deeper understanding of the electronic transport properties of i-MAX phases.

As a further outlook, selective etching of an i-MAX phase delivers so-called i-MXenes, when the M' elements are removed in addition to the A-layers. This leads to a metallic-like 2D structure with ordered metal vacancies [113–115]. Thus, a large anisotropy in conductivity should occur, which has not been experimentally confirmed yet. First non-direction-specific experiments only showed that i-MXenes exhibit a high electric conductivity [114]. There are also theoretical predictions that the physical properties can be tuned by functionalization, e.g. adding O atoms to initially metallic i-MXenes makes them semiconductors with indirect band gaps [107]. Functionalized i-MXenes exhibiting piezoelectricity have also been reported [107]. All in all, i-MXenes open new possible fields in 2D physics comprising either a conducting or semiconducting material with significant piezoelectric properties. Therefore, it would be highly desirable to push the here presented 4-probe measurement techniques to the nanometer scale to enable direct access transport properties of i-MXenes.

The here presented novel method relies on the observation of the crossover between the 2D and 3D regimes, which occurs at a probe spacing that is linearly dependent on the sample thickness. Thinner samples require smaller probe spacings, and vice versa smaller spacing allow thinner samples. In my experiments, the minimal probe spacings is limited to about $1\ \mu\text{m}$, which, depending on the resistance anisotropy, requires a sample thickness of more than $100\ \text{nm}$ to $1\ \mu\text{m}$. Accordingly, the here presented resistivity values represent bulk properties. The smallest spacing between two probes reported in literature is around $25\ \text{nm}$ [13]. Comparable small spacing between four probes has so far not yet been accomplished, but is not a fundamental problem and will certainly be reached soon. To this end, focused-ion-beam techniques can be used to prepare much thinner and well-defined probes with radii down to $17\ \text{nm}$ [116]. This combined with keeping the probes during the transport measurement in tunneling contact, i.e. the STM feedback loop is active [117], will enable well-defined and non-destructive 4-point measurements in near future, probably down to the lower nanometer range. This will also be an improvement over to the lithographically fabricated multi-probes, which presently offer precise probe spacings of $1\ \mu\text{m}$ due to correction factors applied. However, during contact with a sample, these multi-probes are pressed onto the surface, resulting in deformation of the probes and damage to the surface, both of which are detrimental.

The work presented in this thesis can be considered as a contribution to the development of 4-probe STM towards a powerful tool for electronic transport measurements including spectroscopy and potentiometry for the technologically increasingly important nanometer range. The main focus of this work is introducing novel parameter-free methods for the direct determination of the entire resistivity tensor of samples with orthorhombic or higher symmetry with unprecedented accuracy and reliability. The measurement protocols are based on 4-point electronic transport measurements with variable probe configurations and spacings combined with the observation of the crossover between the 2D and 3D transport regimes. The novel methods developed here rely just on a single oriented thin-film sample and do neither require a specific device structure, nor a comparison of samples with different microstructure, or modelling of transport or

effective medium properties. They can be applied in-situ under UHV conditions and to materials that are not available as micrometer-thick crystals or are unstable unless stabilized in thin-film form.

A. Additional Data

A.1. Calibration of the PCUs

The PCUs are designed to operate with different piezo scanner systems, which may have different piezo sensitivities. In contrast to the Matrix controller, the PCUs have no access to the scanner configuration file containing the piezo sensitivities. Therefore, the PCUs display the piezo position in uncalibrated units (values roughly in the range $[-1000, 1000]$). The well controlled motion of the probes from the tunnelling regime into ohmic contact, which is done under PCU control, requires a precise calibration of all three CPU/scanner units. The calibration of the PCU 4 is shown here in detail, but the same procedure has also been performed for PCUs 2 and 3. The corresponding data are shown in figure A.2.

The PCU is connected via remote control with the Matrix controller, which is then used to approach the probe with the z -piezo by several nanometers towards the sample, while the PCU display is read out. The start value is arbitrarily set to $z = 0$ nm and positions closer to the sample correspond to negative values of z . Additionally, the potentiometer for the (uncalibrated) z -axis offset on the PCU front panel can be set independently, which shifts the displayed values. Therefore, two calibrations are done with the offset potentiometer set to 5 and 4, see figures A.1 and A.2. The linear relations between calibrated z -position in nanometers and PCU values yield the following fits, where # symbolizes PCU values.

$$\text{PCU 2, potentiometer 5: } z = (-0.77332 \pm 0.00013) \frac{\text{nm}}{\text{unit}} \# - (850.09 \pm 0.08) \text{ nm}$$

$$\text{PCU 2, potentiometer 4: } z = (-0.77180 \pm 0.00009) \frac{\text{nm}}{\text{unit}} \# - (1102.70 \pm 0.07) \text{ nm}$$

$$\text{PCU 3, potentiometer 5: } z = (-0.77446 \pm 0.00012) \frac{\text{nm}}{\text{unit}} \# - (827.90 \pm 0.08) \text{ nm}$$

$$\text{PCU 3, potentiometer 4: } z = (-0.77420 \pm 0.00010) \frac{\text{nm}}{\text{unit}} \# - (1102.17 \pm 0.08) \text{ nm}$$

$$\text{PCU 4, potentiometer 5: } z = (-0.77159 \pm 0.00012) \frac{\text{nm}}{\text{unit}} \# - (831.91 \pm 0.09) \text{ nm}$$

$$\text{PCU 4, potentiometer 4: } z = (-0.77180 \pm 0.00009) \frac{\text{nm}}{\text{unit}} \# - (1102.71 \pm 0.07) \text{ nm}$$

The slope of the all curves is $m \approx 0.77$ nm per PCU unit, meaning that changing PCU display value by one corresponds to piezo motion of about 0.77 nm. In order to make the PCU values unambiguous and comparable, it is highly advisable to always work with fixed settings of z -offset potentiometers. Throughout this thesis, the offsets are fixed at 5, i.e. in the middle of the total range.

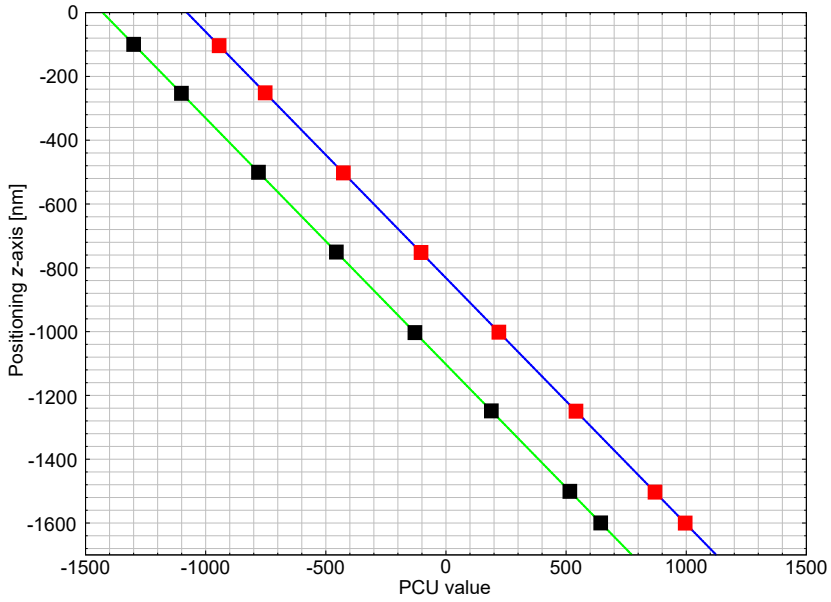


Figure A.1.: Calibration of PCU 4 for z -offsets 5 (blue symbols) and 4 (red symbols). Solid lines are linear fits.

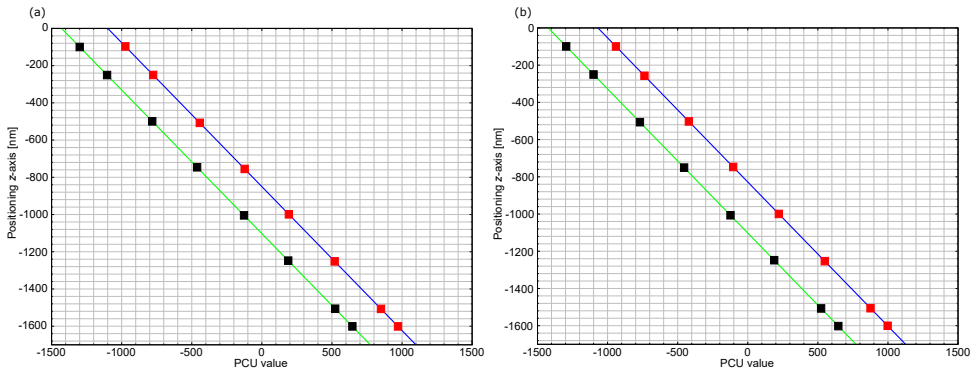


Figure A.2.: Calibration of PCU 2 (a) and 3 (b) for z -offsets 5 (blue symbols) and 4 (red symbols). Solid lines are linear fits.

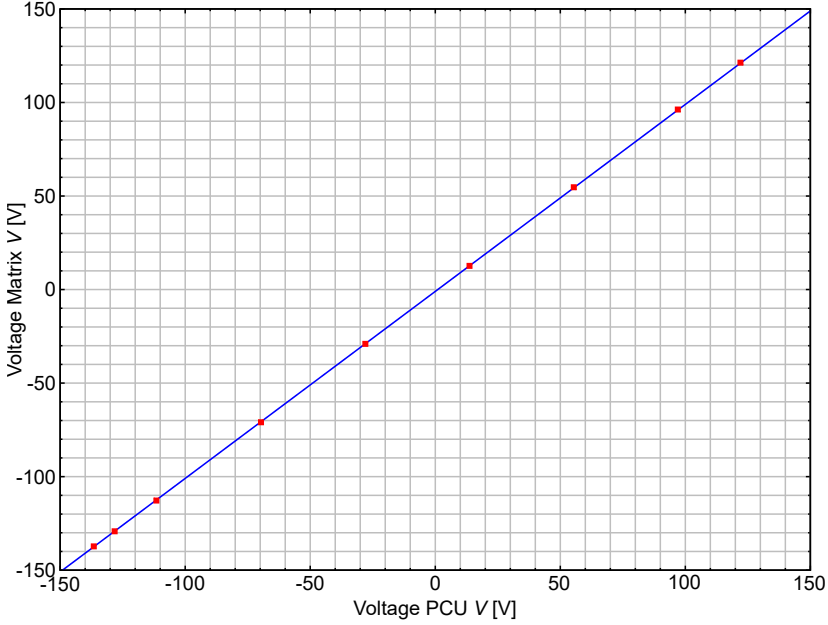


Figure A.3.: Matrix output voltage vs. PCU output voltage for a series of user-selected z -positions. The solid line is a linear fit.

As a final test of the calibrations, one has to make sure that choosing a given z -position in the Matrix software (in nm) or with the PCU potentiometers (in PCU units) leads to the same voltage applied to the z -piezo. To this end, the desired z -position of the piezo is varied via the Matrix interface and manually via the PCU potentiometer and the resulting high-voltage outputs of the Matrix controller and the PCU are recorded. In figure A.3, the Matrix output voltage is plotted versus the PCU voltage output. A linear fit (solid line) delivers a slope of (0.9995 ± 0.0003) . The small offset of about (-0.99 ± 0.03) can be related to a small deviation of the z -offset potentiometer from the value 5, which corresponds to an offset voltage of 0 V. Hence, this plot demonstrates that the voltage output of both Matrix controller and PCU are the same for a given position of the z -piezo.

A.2. Measurements of ex-situ and in-situ test resistors

Plots for test resistor $R = 10\text{ k}\Omega$

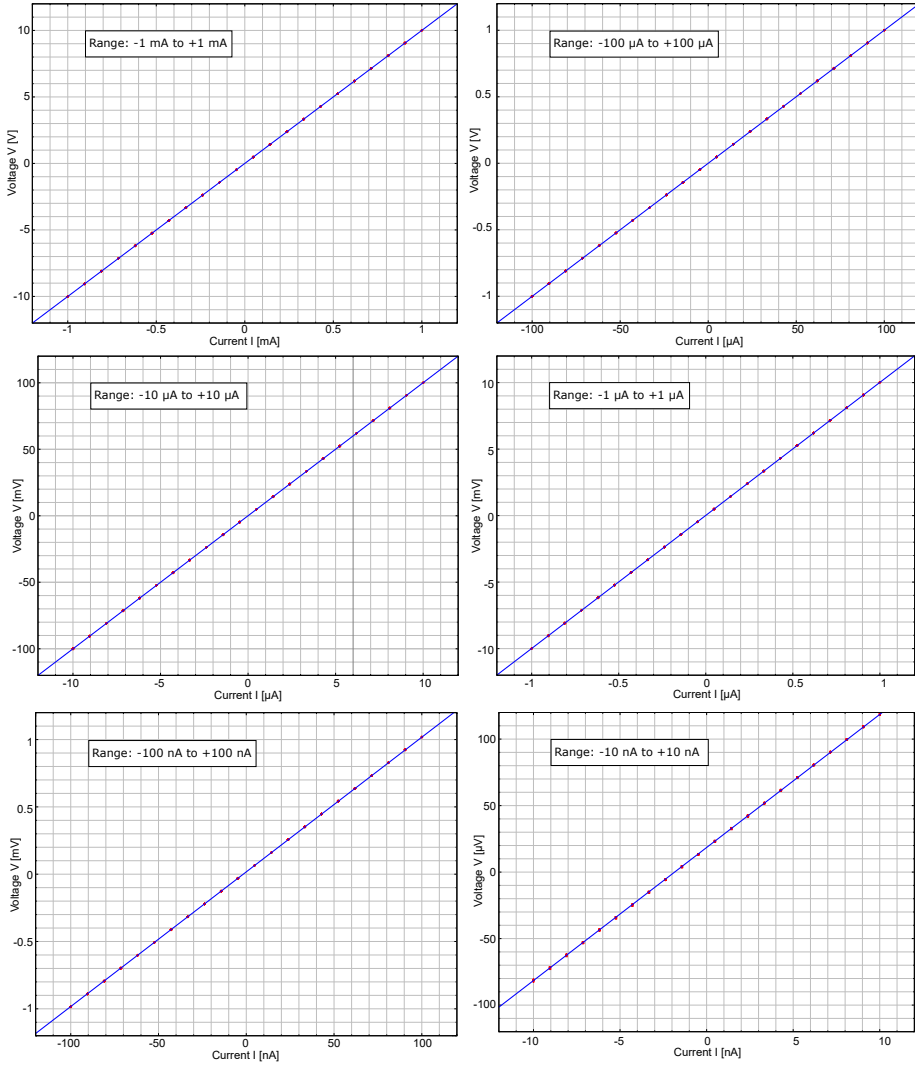


Figure A.4.: V - I plots for test resistor $R = 10\text{ k}\Omega$ measured in different current ranges.

Plots for test resistor $R = 1\Omega$

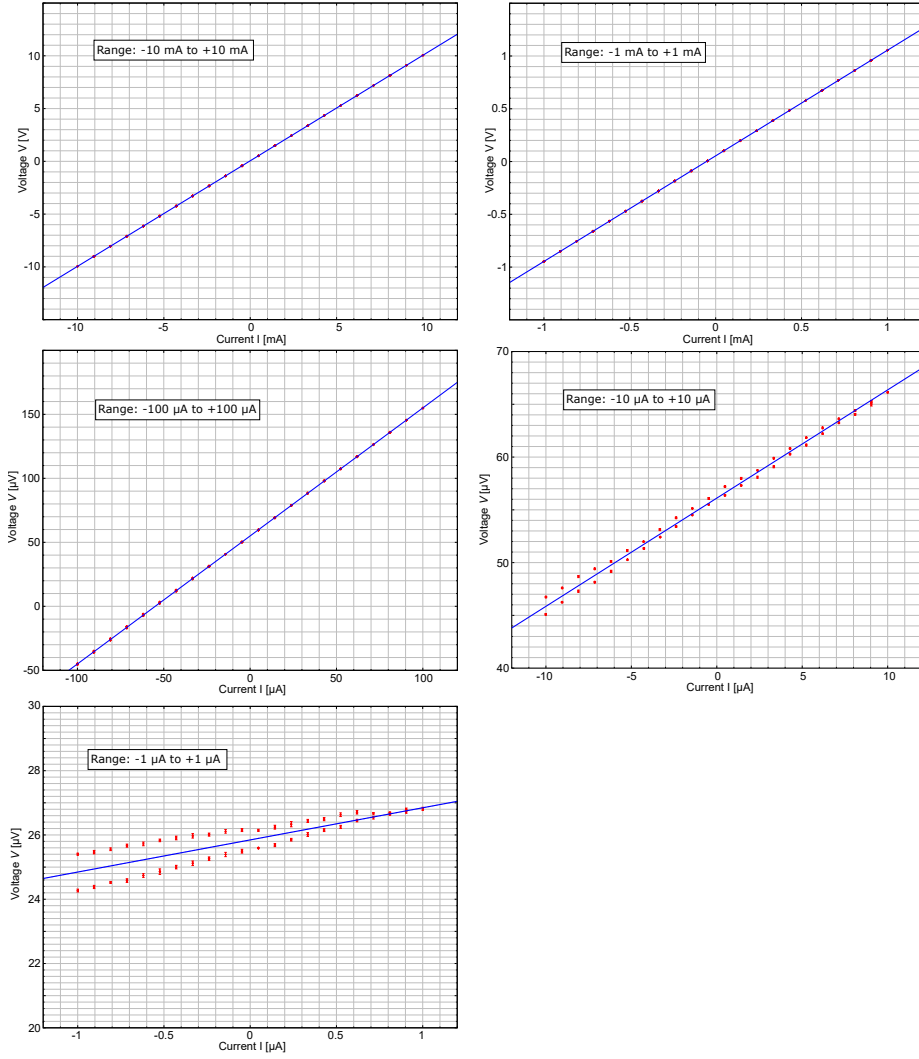


Figure A.5.: V - I plots for test resistor $R = 10\Omega$ measured in different current ranges.

Plots for test resistor $R = 10.0015\text{ m}\Omega$

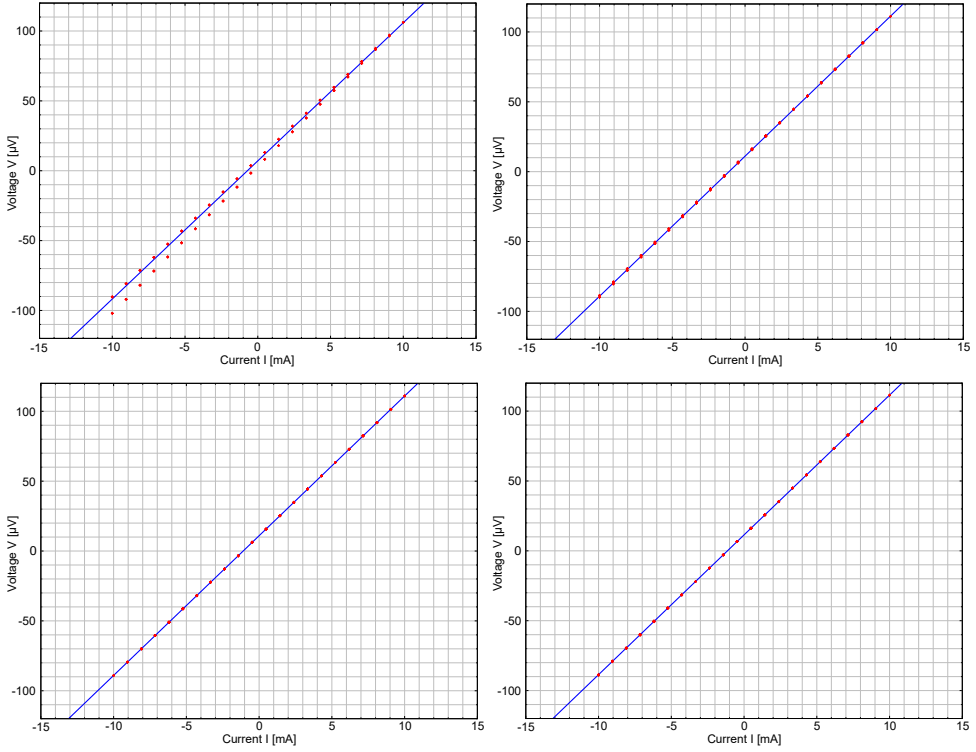


Figure A.6.: Four repeated measurements of the V - I curve for test resistor $R = 10.0015\text{ m}\Omega$.

Plots for test resistor $R = 1.0008 \text{ m}\Omega$

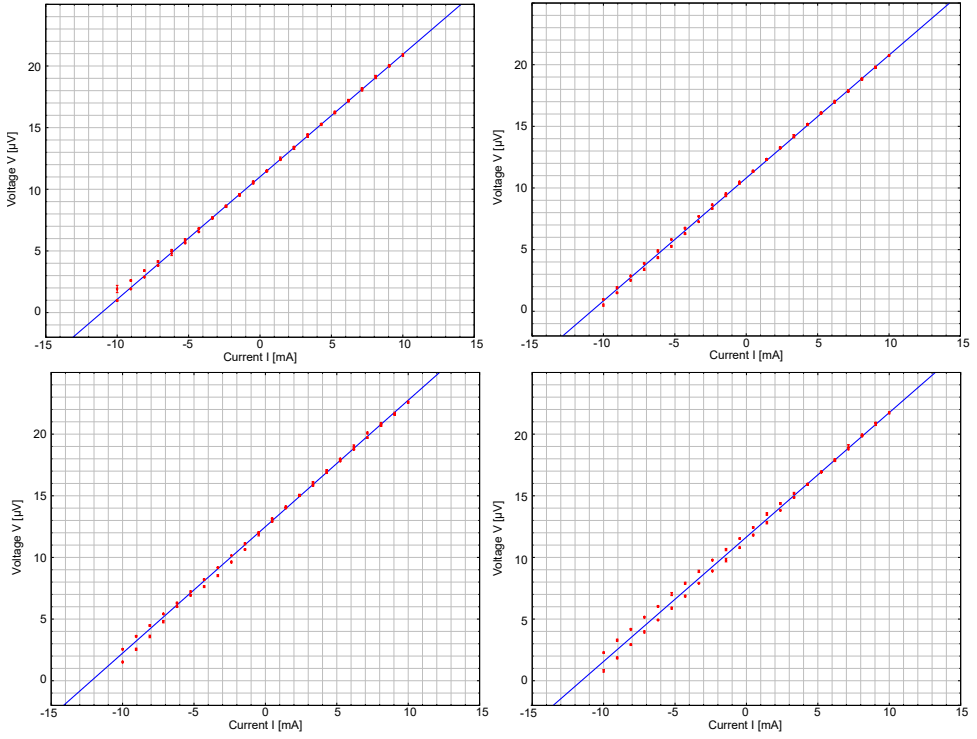


Figure A.7.: Four repeated measurements of the V - I curve for test resistor $R = 1.0008 \Omega$.

Bibliography

- [1] R. A. Serway. *Principle of Physics*. London: Saunders College Publishing, 1998.
- [2] P. Hofmann and J. W. Wells. Surface-sensitive conductance measurements. *J. Phys.: Condens. Matter*, 21:013003, 2009.
- [3] S. M. Sze and K. K. Ng. *Physics of Semiconductor Devices*. Hoboken, NJ: Wiley, 2007.
- [4] I. Miccoli, F. Edler, H. Pfnür, and C. Tegenkamp. The 100th anniversary of the four-point probe technique: the role of probe geometries in isotropic and anisotropic systems. *J. Phys.: Condens. Matter*, 27:223201, 2015.
- [5] F. Wenner. A method for measuring Earth resistivity. *Bull. Bur. Stand.*, 12:469–472, 1915.
- [6] L. B. Valdes. Resistivity Measurements on Germanium for Transistors. *PROC. IRE*, 42:420–427, 1954.
- [7] ASTM. Annual Book of ASTM Standards part 43, F48, 1975.
- [8] L. J. van der Pauw. A method of measuring the resistivity and Hall coefficient on lamellae of arbitrary shape. *Philips Tech. Rev.*, 20:220, 1958.
- [9] A KLA Company Capres. <http://www.capres.com/>. 25.09.2019.
- [10] L. Gammelgaard, P. Bøggild, J. W. Wells, K. Handrup, Ph. Hofmann, J. E. Hansen M. B. Balslev and, and P. R. E. Petersen. A complementary metal-oxide-semiconductor compatible monocantilever 12-point probe for conductivity measurements on the nanoscale. *Appl. Phys. Lett.*, 93:093104, 2008.
- [11] A. Cagliani, F. W. Østerberg, O. Hansen, L. Shiv, P. F. Nielsen, and D. H. Petersen. Breakthrough in current-in-plane tunneling measurement precision by application of multi-variable fitting algorithm. *Rev. Sci. Instrum.*, 88:095005, 2017.
- [12] B. Voigtländer, V. Cherepanov, S. Korte, A. Leis, D. Cuma, S. Just, and F. Lüpke. Invited Review Article: Multi-tip scanning tunneling microscopy: Experimental techniques and data analysis. *Rev. Sci. Instrum.*, 89:101101, 2018.

- [13] M. Kolmer, P. Brandimarte, J. Lis, R. Zuzak, S. Godlewski, H. Kawai, A. Garcia-Lekue, N. Lorente, T. Frederiksen, C. Joachim, D. Sanchez-Porta, and M. Szymon-ski. Electronic transport in planar atomic-scale structures measured by two-probe scanning tunneling spectroscopy. *Nat. Comm.*, 10:1573, 2019.
- [14] I. Shiraki, F. Tanabe, R. Hobara, T. Nago, and S. Hasegawa. Independently driven four-probes for conductivity measurements in ultrahigh vacuum. *Surf. Sci.*, 493:633, 2001.
- [15] H. Grube, B. C. Harrison, J. Jia, and J. J. Boland. Stability, resolution, and tip/tip imaging by a dual-probe scanning tunneling microscope. *Rev. Sci. Instrum.*, 72:4388, 2001.
- [16] K. Takami, M. Akai-Kasaya, A. Saito, M. Aono, and Y. Kuwahara. Construction of independently driven double-tip scanning tunneling microscope. *Jpn. J. Appl. Phys.*, 44:L120, 2005.
- [17] O. Guise, H. Marbach, and J. T. Yates Jr. Development and performance of the nanoworkbench: A four tip STM for conductivity measurements down to submicrometer scales. *Rev. Sci. Instrum.*, 76:045107, 2005.
- [18] W. Yi, I. I. Kaya, I. B. Altfeder, D. M. Chen I. Appelbaum, and V. Narayana-murti. Dual-probe scanning tunneling microscope for study of nanoscale metal-semiconductor interfaces. *Rev. Sci. Instrum.*, 76:063711, 2005.
- [19] J. F. Xu, P. M. Thibado, and Z. Ding. 4K, ultrahigh vacuum scanning tunneling microscope having two orthogonal tips with tunnel junctions as close as a few nanometers. *Rev. Sci. Instrum.*, 77:093703, 2006.
- [20] R. Hobara, N. Nagamura, S. Hasegawa, I. Matsuda, Y. Yamamoto, Y. Miyatake, and T. Nagamura. Variable-temperature independently driven four-tip scanning tunneling microscope. *Rev. Sci. Instrum.*, 78:053705, 2007.
- [21] V. Cherepanov, E. Zubkov, H. Junker, S. Korte, M. Blab, P. Coenen, and B. Voigtländer. Ultra compact multitip scanning tunneling microscope with a diameter of 50 nm. *Rev. Sci. Instrum.*, 83:033707, 2012.
- [22] M. Salomons, B. V. C. Martins, J. Zikovsky, and R. A. Wolkow. Ultra compact multitip scanning tunneling microscope with a diameter of 50 nm. *Rev. Sci. Instrum.*, 85:045126, 2014.
- [23] See www.scientaomicron.com for information about commercial multi-tip STMs.
- [24] See www.rhk-tech.com for information about commercial multi-tip STMs.
- [25] See www.unisoku.com for information about commercial multi-tip STMs.

-
- [26] See www.mprobes.com for information about commercial multi-tip STMs.
- [27] J. W. Wells, J. F. Kallehauge, T. M. Hansen, and P. Hofmann. Disentangling surface, bulk, and space-charge-layer conductivity in Si(111)–(7×7). *Phys. Rev. Lett.*, 97:206803, Nov 2006.
- [28] S. Just, M. Blab, S. Korte, V. Cherepanov, H. Soltner, and B. Voigtländer. Surface and Step Conductivities on Si(111) Surfaces. *Phys. Rev. Lett.*, 115:066801, 2015.
- [29] S. Just, H. Soltner, V. Cherepanov, and B. Voigtländer. Surface conductivity of Si(100) and Ge(100) surfaces determined from four-point transport measurements using an analytical N -layer conductance model. *Phys. Rev. B*, 95:075310, 2017.
- [30] S. Hasegawa. Charge and spin transport on surfaces and atomic layers measured by multi-probe techniques. *J. Phys.: Condens. Matter*, 31:223001, 2019.
- [31] C. Durand, X.-G. Zhang, S. M. Hus, C. Ma, M. A. McGuire, Y. Xu, H. Cao, I. Miotkowski, Y. P. Chen, and A.-P. Li. Differentiation of Surface and Bulk Conductivities in Topological Insulators via Four-Probe Spectroscopy. *Nano Lett.*, 16:22132220, 2016.
- [32] F. Lüpke, M. Eschbach, T. Heider, M. Lanius, P. Schüffegen, D. Rosenbach, N. v. d. Driesch, V. Cherepanov, G. Mussler, L. Plucinski, D. Grützmacher, C. M. Schneider, F. S. Tautz, and B. Voigtländer. Electrical resistance of individual defects at a topological insulator surface. *Nat. Comm.*, 8:15704, 2017.
- [33] F. Lüpke, S. Just, M. Eschbach, T. Heider, E. Młyńczak, M. Lanius, P. Schüffegen, D. Rosenbach, N. v. d. Driesch, V. Cherepanov, G. Mussler, L. Plucinski, D. Grützmacher, C. M. Schneider, F. S. Tautz, and B. Voigtländer. In situ disentangling surface state transport channels of a topological insulator thin film by gating. *npj Quantum Materials*, 46, 2018.
- [34] F. Lüpke, S. Korte, V. Cherepanov, and B. Voigtländer. Scanning tunneling potentiometry implemented into a multi-tip setup by software. *Rev. Sci. Instrum.*, 86:123701, 2015.
- [35] F. Lüpke, D. Cuma, S. Korte, V. Cherepanov, and B. Voigtländer. Four-point probe measurements using current probes with voltage feedback to measure electric potentials. *J. Phys.: Condens. Matter*, 30(5):054004, 2018.
- [36] H. Okino, I. Matsuda, R. Hobara, Y. Hosomura, and S. Hasegawa. In situ resistance measurements of epitaxial cobalt silicide nanowires on Si(110). *Appl. Phys. Lett.*, 86:233108, 2005.
- [37] K. S. Novoselov, V. I. Fal’ko, L. Colombo, P. R. Gellert, M. G. Schwab, and K. Kim. A roadmap for graphene. *Nature*, 490:192, 2012.

- [38] K. S. Novoselov, A. Mishchenko, A. Carvalho, and A. H. Castro Neto. 2D materials and van der Waals heterostructures. *Science*, 353:461, 2016.
- [39] A. S. Ingason, M. Dahlqvist, and J. Rosen. Magnetic MAX phases from theory and experiments; a review. *J. Phys.: Condens. Matter*, 28:433003, 2016.
- [40] M. Magnuson and M. Mattesini. Chemical bonding and electronic-structure in MAX phases as viewed by X-ray spectroscopy and density functional theory. *Thin Solid Films*, 621:108–130, 2017.
- [41] P. Eklund, M. Beckers, U. Jansson, H. Högberg, and L. Hultman. The $M_{n+1}AX_n$ Phases: Materials Science and Thin-Film Processing. *Thin Solid Films*, 518:1851–1878, 2010.
- [42] I. P. Novoselova, A. Petruhins, U. Wiedwald, D. Weller, J. Rosen, M. Farle, and R. Salikhov. Long-term stability and thickness dependence of magnetism in thin $(Cr_{0.5}Mn_{0.5})_2GaC$ MAX phase films. *Mater. Res. Lett.*, 7:159–163, 2019.
- [43] Michel W. Barsoum. The $M_{n+1}AX_n$ Phases: A New Class of Solids; Thermodynamically Stable Nanolaminates. *Prog. Solid State. Chem.*, 28:201–281, 2000.
- [44] Michel W. Barsoum. *MAX Phases: Properties of Machinable Ternary Carbides and Nitrides*. Wiley-VCH, 2013.
- [45] A. Dash, R. Vaßen, O. Guillon, and J. Gonzalez-Julian. Molten salt shielded synthesis of oxidation prone materials in air. *Nature Mater.*, 18:465–470, 2019.
- [46] C. A. M. dos Santos, A. de Campos, M. S. da Luz, B. D. White, J. J. Neumeier, B. S. de Lima, and C. Y. Shigue. Procedure for measuring electrical resistivity of anisotropic materials: A revision of the Montgomery method. *J. Appl. Phys.*, 110:083703, 2011.
- [47] O. F. de Lima, R. A. Ribeiro, M. A. Avila, C. A. Cardoso, and A. A. Coelho. Anisotropic Superconducting Properties of Aligned MgB_2 Crystallites. *Phys. Rev. Lett.*, 86:5974–5977, 2001.
- [48] B. Korin-Hamzić, E. Tafra, M. Basletić, A. Hamzić, and M. Dressel. Conduction anisotropy and Hall effect in the organic conductor $(TMTTF)_2AsF_6$: Evidence for Luttinger liquid behavior and charge ordering. *Phys. Rev. B*, 73:115102, 2006.
- [49] C. Tegenkamp, Z. Kallassy, H.-L. Günter, V. Zielasek, and H. Pfnür. Anisotropic conductance of Pb-induced chain structures on Si(557) in the monolayer regime. *Eur. Phys. J. B*, 43:557–564, 2005.
- [50] J. D. Wasscher. Determination of the resistivity anisotropy of orthorombic materials via transverse resistivity measurements. *Philips Res. Rep.*, 16:301–306, 1961.

-
- [51] H. C. Montgomery. Method for Measuring Electrical Resistivity of Anisotropic Materials. *J. Appl. Phys.*, 42:2971, 1971.
- [52] K. A. Borup, K. F. F. Fischer, D. R. Brown, G. J. Snyder, and B. B. Iversen. Measuring anisotropic resistivity of single crystals using the van der Pauw technique. *J. Appl. Phys.*, 92:045210, 2015.
- [53] P. Walmsley and I. R. Fisher. Determination of the resistivity anisotropy of orthorhombic materials via transverse resistivity measurements. *Rev. Sci. Instrum.*, 88:043901, 2017.
- [54] Taizo Kanagawa, Rei Hobara, Iwao Matsuda, Takehiro Tanikawa, Akiko Natori, and Shuji Hasegawa. Anisotropy in Conductance of a Quasi-One-Dimensional Metallic Surface State Measured by a Square Micro-Four-Point Probe Method. *Phys. Rev. Lett.*, 91:036805, 2003.
- [55] T. Ouisse, L. Shi, B. A. Piot, B. Hackens, V. Mauchamp, and D. Chaussende. Magnetotransport properties of nearly-free electrons in two-dimensional hexagonal metals and application to the $M_{n+1}AX_n$ phases. *Phys. Rev. B*, 92:045133, 2015.
- [56] M. Charalambous, J. Chaussy, and P. Lejay. Evidence from resistivity measurements along the c axis for a transition within the vortex state for $H \parallel ab$ in single-crystal $YBa_2Cu_3O_7$. *Phys. Rev. B*, 45:5091, 1992.
- [57] N. Haddad, E. Garcia-Cauarel, L. Hultman, M. W. Barsoum, and G. Hug. Dielectric properties of Ti_2AlC and Ti_2AlN MAX phases: The conductivity anisotropy. *J. Appl. Phys.*, 104:023531, 2008.
- [58] V. Mauchamp, G. Hug, M. Bugnet, T. Cabioc'h, and M. Jaouen. Anisotropy of Ti_2AlN dielectric response investigated by ab initio calculations and electron energy-loss spectroscopy. *Phys. Rev. B*, 81:035109, 2010.
- [59] T. H. Scabarozi, P. Eklund, J. Emmerlich, H. Högberg, T. Meehan, P. Finkel, M. Barsoum, J. Hettinger, L. Hultman, and S. Lofland. Weak electronic anisotropy in the layered nanolaminate Ti_2GeC . *Solid State Commun.*, 146:498–501, 2008.
- [60] V. Mauchamp, W. Yu, L. Gence, L. Piraux, T. Cabioc'h, V. Gauthier, P. Eklund, and S. Dubois. Anisotropy of the resistivity and charge-carrier sign in nanolaminated Ti_2AlC : Experiment and ab initio calculations. *Phys. Rev. B*, 87:235105, 2013.
- [61] T. Flatten, F. Matthes, A. Petruhins, R. Salikhov, U. Wiedwald, M. Farle, J. Rosen, D. E. Bürgler, and C. M. Schneider. Direct measurement of anisotropic conductivity in a nanolaminated $(Mn_{0.5}Cr_{0.5})_2GaC$ thin film. *Appl. Phys. Lett.*, 15:094101, 2019.

- [62] P. Jaschinsky, J. Wensorra, M. I. Lepsa, J. Mysliveček, and B. Voigtländer. Nanoscale charge transport measurements using a double-tip scanning tunneling microscope. *J. Appl. Phys.*, 104:094307, 2008.
- [63] J. Albers and H. L. Berkowitz. An Alternative Approach to the Calculation of Four-Probe Resistances on Nonuniform Structures. *J. Electrochem. Soc.*, 132:2453, 1985.
- [64] J. J. Kopanski, J. Albers, G. P. Carver, and J. R. Ehrstein. Verification of the Relation Between Two-Probe and Four-Probe Resistances as Measured on Silicon Wafers. *J. Electrochem. Soc.*, 137:3935, 1990.
- [65] R. A. Weller. An algorithm for computing linear four-point probe thickness correction factors. *Rev. Sci. Instrum.*, 72:3580, 2001.
- [66] S. Z. Tehrani, W. L. Lim, and L. Lee. Correction factors for film resistivity measurements. *Measurement*, 45:219, 2012.
- [67] L. E. Murr. *Handbook of Materials Structures, Properties, Processing and Performance*. Springer Internaitonal Publishing Switzerland, 2015.
- [68] L. J. van der Pauw. Determination of resistivity tensor and Hall tensor of anisotropic conductors. *Philips Res. Rep.*, 16:187, 1961.
- [69] N. Schnitzler. *Entwicklung eines Mess- und Steuersignal-Kontrollers für den Betrieb eines 4-Spitzen Rastertunnelmikroskops*. Fachhochschule Aachen, Forschungszentrum Jülich - PGI-6, 2014.
- [70] B. Voigtländer. *Scanning Probe Microscopy - Atomic Force Microscopy and Scanning Tunneling Microscopy*. Springer-Verlag GmbH Berlin Heidelberg, 2015.
- [71] Scienta Omicron. <https://www.scientaomicron.com/en/products/lt-nanoprobe/instrument-concept>. 17.09.2019.
- [72] Scienta Omicron. *UHV Gemini – User's Guide*. Scienta Omicron, 2006.
- [73] Zeiss. *Manual for the SUPRA (VP) and ULTRA Scanning Electron Microscopes*. Carl Zeiss AG, 2005.
- [74] C. J. Chen. *Introduction to Scanning Tunneling Microscopy*. New York: Oxford University Press, 1993.
- [75] J. P. Ibe, P. P. Bey Jr., S. L. Brandow, R. A. Brizzolara, N. A. Burnham, D. P. DiLella, K. P. Lee, C. R. K. Marrian, and R. J. Colton. On the electrochemical etching of tips for STM. *J. Vac. Sci. Technol. A*, 8:3570, 1990.

-
- [76] A.-S. Lucier. *Preparation and Characterization of Tungsten Tips Suitable for Molecular Electronics Studies*. Center for the Physics of Materials, Department of Physics, McGill University, Montreal, Quebec, Canada - Master thesis, 2004.
- [77] O. L. Guise, J. W. Ahner, M.-C. Jung, P. C. Goughnour, and Jr. J. T. Yates. On the electrochemical etching of tips for STM. *Nano Lett.*, 2:190, 2002.
- [78] Scienta Omicron. *ISE 5 Ion Source and NG ISE 5 Control Unit User's Guide*. Scienta Omicron, 2012.
- [79] J. Hall. *Master thesis*. Universität Köln, Forschungszentrum Jülich - PGI-6, 2015.
- [80] I. Ekvall, E. Wahlström, D. Claesson, H. Olin, and E. Olsson. Preparation and characterization of electrochemically etched W tips for STM. *Meas. Sci. Technol.*, 10:11–18, 1999.
- [81] V. T. Binh. In situ fabrication and regeneration of microtips for scanning tunneling microscopy. *Journal of Microscopy*, 152:355–361, 1988.
- [82] U. Staufer, L. P. Muray, D. P. Kern, , and T. H. P. Chang. Investigation of emitter tips for scanning tunneling microscope-based microprobe systems. *J. Vac. Sci. Technol. B*, 9:2962, 1991.
- [83] A. Stalder. *Mechanics and Electronics on the Atomic Scale: A Study using Scanning Probe Methods*. University of Freiburg, 1995.
- [84] A. Schirmeisen. *Metallic Adhesion and Tunneling at the Atomic Scale*. McGill University, 1999.
- [85] A.-S. Lucier. *Preparation and Characterization of Tungsten Tips Suitable for Molecular Electronics Studies*. McGill University, 2004.
- [86] H. Ibach. *Physics of Surfaces and Interfaces*. Springer Heidelberg Berlin, 2006.
- [87] E. Taglauer. Surface cleaning using sputtering. *Applied Physics A*, 51:238, 1990.
- [88] K. Ilse, T. Tänzer, C. Hagendorf, and M. Turek. Geometrical correction factors for finite-size probe tips in microscopic four-point-probe resistivity measurements. *J. Appl. Phys.*, 116:224509, 2014.
- [89] D. R. Lide ed. *CRC Handbook of Chemistry and Physics, Internet Version 2005*. FCRC Press, Boca Raton, FL, 2005.
- [90] T. Sun. *Classical Size Effect In Copper Thin Films: Impact Of Surface And Grain Boundary Scattering On Resistivity*. University of Central Florida, 2009.

- [91] K. L. Chopra, L. C. Bobb, and M. H. Francombe. Electric Resistivity of Thin Single-Crystal Gold Films. *J. Appl. Phys.*, 34:1699, 1963.
- [92] Y. Namba. Resistivity and Temperature Coefficient of Thin Metal Films with Rough Surface. *Japanese J. Appl. Phys.*, 9:1326, 1970.
- [93] K. Fuchs. Electrical Resistance in Thin Metal Films. *Proc. Cambridge Phil. Soc.*, 34:100, 1938.
- [94] E. H. Sondheimer. Mean Free Path of Electrons in Metals. *Advan. Phys.*, 1:1, 1952.
- [95] A. F. Mayadas and M. Shatzkes. Electrical-Resistivity Model for Polycrystalline Films: the Case of Arbitrary Reflection at External Surfaces. *Phys. Rev. B*, 1:1382–1389, 1970.
- [96] S. Maitrejean, V. Carreau, O. Thomas, S. Labat, B. Kaouache, M. Verdier, J. Lepinoux, Y. Bréchet, M. Legros, J. Douin, S. Brandstetter, C. Cayron, O. Sicardy, D. Weygand, O. Dubreuil, and P. Normandon. Cu Grain Growth in Damascene Narrow Trenches. *AIP Conf. Proc.*, 1143:135, 2009.
- [97] A. K Pal, P. Sen, and A. K. Barua. Electrical properties of vacuum-evaporated copper films. *Thin Solid Films*, 25:S25–S28, 1975.
- [98] H.-D. Liu, Y.-P. Zhao, G. Ramanath, S. P. Murarka, and G.-C. Wand. Thickness dependent electrical resistivity of ultrathin (< 40 nm) Cu films. *Thin Solid Films*, 384:151–156, 2001.
- [99] F. Feder, P. Rudolf, and P. Wissmann. The resistivity of single-crystal copper films. *Thin Solid Films*, 36:183–186, 1976.
- [100] W. Zhang, S. H. Brongersma, O. Richard, B. Brijs, R. Palmans, L. Froyen, and K. Maex. Influence of the electron mean free path on the resistivity of thin metal films. *Microelectronic Engineering*, 76:146–152, 2004.
- [101] K. Bordo and H.-G. Rubahn. Effect of deposition rate on structure and surface morphology of thin evaporated Al films on dielectrics and semiconductors. *Materials Science*, 18, 2012.
- [102] R. Munoz, C. Gonzalez-Fuentes, R. Henriquez, A. Espinosa, G. Kremer, L. Moraga, A. Ibañez-Landeta, S. Bahamondes, S. Donoso, and M. Flores. Resistivity of thin gold films on mica induced by electron-surface scattering from a self-affine fractal surface. *J. Appl. Phys.*, 110:023710, 2011.

-
- [103] A. Petruhins, A. S. Ingason, J. Lu, F. Magnus, S. Olafsson, and J. Rosen. Synthesis and characterization of magnetic $(\text{Cr}_{0.5}\text{Mn}_{0.5})_2\text{GaC}$ thin films. *J. Mater. Sci.*, 50:4495–4502, 2015.
- [104] R. Salikhov, A. S. Semisalova, A. Petruhins, A. Sigurdur Ingason, J. Rosen, U. Wiedwald, and M. Farle. Magnetic Anisotropy in the $(\text{Cr}_{0.5}\text{Mn}_{0.5})_2\text{GaC}$ MAX Phase. *Mater. Res. Lett.*, 3:156–160, 2015.
- [105] A. Thore, M. Dahlqvist, B. Alling, and J. Rosen. First-principles calculations of the electronic, vibrational, and elastic properties of the magnetic laminate Mn_2GaC . *J. Appl. Phys.*, 116:103511, 2014.
- [106] S. Lin, P. Tong, B. S. Wang, Y. N. Huang, W. J. Lu, D. F. Shao, B. C. Zhao, W. H. Song, and Y. P. Sun. Magnetic and electrical/thermal transport properties of Mn-doped $\text{M}_{n+1}\text{AX}_n$ phase compounds $\text{Cr}_{2-x}\text{Mn}_x\text{GaC}$ ($0 \leq x \leq 1$). *J. Appl. Phys.*, 113:053502, 2013.
- [107] M. Khazaei, V. Wang, C. Sevik, A. Ranjbar, M. Arai, and S. Yunoki. Electronic structures of iMAX phases and their two-dimensional derivatives: A family of piezoelectric materials. *Phys. Rev. Materials*, 2:074002, 2018.
- [108] A. Thore and J. Rosen. An investigation of the in-plane chemically ordered atomic laminates $(\text{Mo}_{2/3}\text{Sc}_{1/3})_2\text{AlC}$ and $(\text{Mo}_{2/3}\text{Y}_{1/3})_2\text{AlC}$ from first principles. *Phys. Chem. Chem. Phys.*, 19:21595, 2017.
- [109] M. Dahlqvist, J. Lu, R. Meshkian, Q. Tao, L. Hultman, and J. Rosen. Prediction and synthesis of a family of atomic laminate phases with Kagomé-like and in-plane chemical ordering. *Sci. Adv.*, 3:e1700642, 2017.
- [110] Q. Tao, J. Lu, M. Dahlqvist, A. Mockute, S. Calder, A. Petruhins, R. Meshkian, O. Rivin, D. Potashnikov, E. Caspi, H. Shaked, A. Hoser, C. Opagiste, R.-M. Galera, R. Salikhov, U. Wiedwald, C. Ritter, A. Wildes, B. Johansson, and J. Rosen. Atomically Layered and Ordered Rare-Earth i-MAX Phases: A New Class of Magnetic Quaternary Compounds. *Chem. Mater.*, 31:2476–2485, 2019.
- [111] Quanzheng Tao. Private communication. 2019.
- [112] B. H. Toby. R factors in Rietveld analysis: How good is good enough? *Powder Diffraction*, 21:0885–7156, 2006.
- [113] H. Lind, J. Halim, S. Simak, and J. Rosen. Investigation of vacancy-ordered $\text{Mo}_{1.33}\text{C}$ MXene from first principles and x-ray photoelectron spectroscopy. *Phys. Rev. Materials*, 1:044002, 2017.

- [114] Q. Tao, Ma. Dahlqvist, J. Lu, S. Kota, R. Meshkian, J. Halim, J. Palisaitis, L. Hultman, M. Barsoum, P. Persson, and J. Rosen. Two-dimensional $\text{Mo}_{1.33}\text{C}$ MXene with divacancy ordering prepared from parent 3D laminate with in-plane chemical ordering. *Nat. Comm.*, 8:14949, 2017.
- [115] R. Meshkian, M. Dahlqvist, J. Lu, B. Wickman, J. Halim, J. Thörnberg, Q. Tao, S. Li, S. Intikhab, J. Snyder, M. Barsoum, M. Yildizhan, J. Palisaitis, L. Hultman, P. Persson, and J. Rosen. W-Based Atomic Laminates and Their 2D Derivative $\text{W}_{1.33}\text{C}$ MXene with Vacancy Ordering. *Adv. Mater.*, 30:1706409, 2018.
- [116] S. Kawai, A. S. Foster, T. Björkman, S. Nowakowska, J. Björk, F. F. Canova, L. H. Gade, T. A. Jung, and E. Meyer. Van der Waals interactions and the limits of isolated atom models at interfaces. *Nat. Comm.*, 7:11559, 2016.
- [117] F. Lüpke, D. Cuma, S. Korte, V. Cherepanov, and B. Voigtländer. Four-probe measurements using current probes with voltage feedback to measure electric potentials. *J. Phys.: Condens. Matter*, 30:054004, 2018.

List of Own Publications

Paper

August 2019

Tim Flatten, Frank Matthes, Andrejs Petruhins, Ruslan Salikhov, Ulf Wiedwald, Michael Farle, Johanna Rosen, Daniel E. Bürgler and Claus M. Schneider · Direct measurement of anisotropic conductivity in a nanolaminated $(\text{Mn}_{0.5}\text{Cr}_{0.5})_2\text{GaC}$ thin film, *Appl. Phys. Lett.* **115**:094101, 2019, DOI: <https://doi.org/10.1063/1.5115347>

Poster contribution

Workshop – September 2016 Jülich – Charge Transport at Surfaces and Nanostructures with Multi-Probe Techniques

Tim Flatten, Frank Matthes, Daniel E. Bürgler, Claus. M. Schneider · Towards Electronic Transport Measurements in 2-Dimensional Systems: Transition Metal Dichalcogenides and Topological Insulators

Conference – March 2017 Dresden – Frühjahrstagung DPG – Focus Session: Charge transport at surfaces and nanostructures with multi-probe techniques

Tim Flatten, Sven Borghardt, Frank Matthes, Beata Kardynal, Daniel E. Bürgler, and Claus M. Schneider · Electronic Transport Measurements of 2-Dimensional Systems with a 4-Probe STM

Workshop – September 2018 Jülich – Charge Transport at Surfaces and Nanostructures with Multi-Probe Techniques

Tim Flatten, Ruslan Salikhov, Frank Matthes, Ulf Wiedwald, Daniel E. Bürgler, and Claus M. Schneider · Anisotropic Transport Measurements for $(\text{Cr}_{0.5}\text{Mn}_{0.5})_2\text{GaC}$ MAX Phase using the LT Nanoprobe

Acknowledgment

I would like to sincerely thank all the people who have supported me over the last three and a half years. Firstly, my gratitude to my supervisor Dr. Daniel E. Bürgler who gave me the chance to join the PGI-6 institute. Thanks for your support, especially during the writing time of my publication and thesis. I appreciate that your door was always open and you could be approached with any question.

I acknowledge the head of the institute, Prof. Dr. Claus M. Schneider, for the opportunity to visit conferences and to work in well equipped laboratories. Thank you for the nice coffee-lectures and the various anecdotes during the coffee breaks which certainly enriched the working day.

I would like to thank Prof. Dr. Thomas Michely agreeing to take over the second referee and I would also like to thank Prof. Dr. Achim Rosch for chairing the examination committee.

I further acknowledge the working group of Prof. Dr. Johanna Rosen for the nice MAX and i-MAX phase samples, especially Quanzheng Tao and Dr. Andrejs Petruhins for the sample preparation as well as the nice and always helpful communications. I would further like to thank Quanzheng Tao for providing the unpublished information's about the i-MAX phase. Belonging to the MAX phase project, I would like to acknowledge the working group of Prof. Dr. Michael Farle. My gratitude to Dr. Ulf Wiedwald and Dr. Ruslan Salikhov for the supporting talks.

I would also like to thank Dr. Frank Matthes. If I had any questions concerning the experiments I could always come to you. Furthermore, the Thursday's evening badminton sessions were always a hard fight, which was connected with a lot of fun and was a nice finish of a working day. Dr. Carsten Wiemann, I'm sorry I left the office for the last year. But thanks anyway for your support during my PhD time and for the open discussions on all sorts of topics.

My gratitude to the technical staff, especially Thomas Jansen, Norbert Schnitzler, Heinz Pfeiffer and Arnd Bremen. You have always helped me, be it with the vacuum system, small precision mechanical problems or turbopumps, as well as errors in the matrix or all possible questions concerning electronics. Thank you all!

Finally, I want to thank the working group of Dr. Daniel E. Bürgler for the nice three

Acknowledgment

and half years. It was a pleasure to meet you - Samuel Königshofen, Dr. Sebastian Schleicher and Thomas-Christian Pradella.

Thank you Tristan Heider for the helpful talks during our PhD time! I would also like to thank all the other PGI-6 staff members, who I cannot mention by name here, for the good working atmosphere, for the numerous coffee rounds, excursions and Christmas parties as well as Lasertag and Paintball matches.

In the end, I would like to thank my fiancée, my family and all my friends, without whose support I would not have been able to write this dissertation.

Erklärung

Ich versichere, dass ich die von mir vorgelegte Dissertation selbstständig angefertigt, die benutzten Quellen und Hilfsmittel vollständig angegeben und die Stellen der Arbeit – einschließlich Tabellen, Karten und Abbildungen –, die anderen Werken im Wortlaut oder dem Sinn nach entnommen sind, in jedem Einzelfall als Entlehnung kenntlich gemacht habe; dass diese Dissertation noch keiner anderen Fakultät oder Universität zur Prüfung vorgelegen hat; dass sie – abgesehen von unten angegebenen Teilpublikationen – noch nicht veröffentlicht worden ist sowie, dass ich eine solche Veröffentlichung vor Abschluss des Promotionsverfahren nicht vornehmen werde.

Die Bestimmung der Promotionsordnung sind mir bekannt. Die von mir vorgelegte Dissertation ist von PD. Dr. Daniel E. Bürgler betreut worden.

Teilpublikation:

T. Flatten *et al.*, Direct measurement of anisotropic conductivity in a nanolaminated $(\text{Mn}_{0.5}\text{Cr}_{0.5})_2\text{GaC}$ thin film, *Appl. Phys. Lett.* **115**:094101, 2019
DOI: <https://doi.org/10.1063/1.5115347>

Köln, den 05. Dezember 2019

Tim Flatten

Curriculum Vitae

Persönliche Daten

Name	Tim Flatten
Anschrift	Luisenstraße 22A, D-50170 Kerpen
Geburtsdaten	26. August 1989 in Bonn
Staatsbürgerschaft	Deutsch
Familienstand	Ledig

Derzeitige Tätigkeit

05/2016 – 02/2020	Promotionsarbeit am Forschungszentrum Jülich in der Gruppe von Daniel E. Bürgler Thema der Arbeit: Direct measurement of anisotropic resistivity in thin films using a 4-probe STM
-------------------	---

Studium / Schulausbildung

12/2012 – 10/2015	Master of Science in Physik (Abschlussnote: gut) an der Rheinischen Friedrich-Wilhelms-Universität Bonn
10/2009 – 10/2012	Bachelor of Science in Physik (Abschlussnote: gut) an der Rheinischen Friedrich-Wilhelms-Universität Bonn
2000 – 2009	Abitur am Collegium Josephinum Bonn

Sonstige Tätigkeiten

10/2015 – 02/2016	Wissenschaftliche Hilfskraft in Bonn
10/2014 – 10/2015	Studentische Hilfskraft in Bonn
Frühjahr 2012	Praktikum am DESY in Hamburg (OLYMPUS-Experiment)
Seit 2011	Geschäftsführer der Karate Abteilung des SC Fortuna Bonn
Herbst 2010	Praktikum am DESY in Hamburg (OLYMPUS-Experiment)
2006 und 2007	Auslandsaufenthalte an der Mullumbimby High School in Australien

Köln, den 05. Dezember 2019

Band / Volume 199

Regulation and assembly of the cytochrome *bc*₁-aa₃ supercomplex in *Corynebacterium glutamicum*

C.-F. Davoudi (2019), 135 pp

ISBN: 978-3-95806-416-4

Band / Volume 200

Variability and compensation in Alzheimer's disease across different neuronal network scales

C. Bachmann (2019), xvi, 165 pp

ISBN: 978-3-95806-420-1

Band / Volume 201

Crystal structures and vibrational properties of chalcogenides: the role of temperature and pressure

M. G. Herrmann (2019), xi, 156 pp

ISBN: 978-3-95806-421-8

Band / Volume 202

Current-induced magnetization switching in a model epitaxial Fe/Au bilayer

P. Gospodarič (2019), vi, 120, XXXVIII pp

ISBN: 978-3-95806-423-2

Band / Volume 203

Network architecture and heme-responsive gene regulation of the two-component systems HrrSA and ChrSA

M. Keppel (2019), IV, 169 pp

ISBN: 978-3-95806-427-0

Band / Volume 204

Spin-orbitronics at the nanoscale: From analytical models to real materials

J. Bouaziz (2019), 228 pp

ISBN: 978-3-95806-429-4

Band / Volume 205

Advanced methods for atomic scale spin simulations and application to localized magnetic states

G. P. Müller (2019), xx, 194 pp

ISBN: 978-3-95806-432-4

Band / Volume 206

Different growth modes of molecular adsorbate systems and 2D materials investigated by low-energy electron microscopy

J. E. Felter (2019), vi, 114, XXXIV pp

ISBN: 978-3-95806-434-8

Band / Volume 207

**NADPH-related studies performed with
a SoxR-based biosensor in *Escherichia coli***

A. Spielmann (2019), IV, 73 pp

ISBN: 978-3-95806-438-6

Band / Volume 208

**Chemisorption aromatischer Moleküle auf Übergangsmetalloberflächen:
Bildung molekularer Hybridmagnete**

S. Schleicher (2019), 109 pp

ISBN: 978-3-95806-442-3

Band / Volume 209

**Regulatory interactions between *Corynebacterium glutamicum*
and its prophages**

M. Hünnefeld (2019), IV, 209 pp

ISBN: 978-3-95806-445-4

Band / Volume 210

Quantum Technology

Lecture Notes of the 51st IFF Spring School 2020

23 March – 03 April 2020, Jülich, Germany

ed. by H. Bluhm, T. Calarco, D. DiVincenzo (2020), ca. 700 pp

ISBN: 978-3-95806-449-2

Band / Volume 211

Interaction of physical fields with nanostructured materials

(2020), 255 pp

ISBN: 978-3-95806-450-8

Band / Volume 212

**First-principles study of collective spin excitations in noncollinear
magnets**

F.J. dos Santos (2020), 270 pp

ISBN: 978-3-95806-459-1

Band / Volume 213

**Direct measurement of anisotropic resistivity in thin films
using a 4-probe STM**

T. Flatten (2020), viii, 129 pp

ISBN: 978-3-95806-460-7

Weitere **Schriften des Verlags im Forschungszentrum Jülich** unter
<http://www.zb1.fz-juelich.de/verlagextern1/index.asp>

Schlüsseltechnologien / Key Technologies
Band / Volume 213
ISBN 978-3-95806-460-7